STRUCTURE-PROPERTY LINKAGES FOR POLYCRYSTALLINE MATERIALS USING MATERIALS KNOWLEDGE SYSTEMS

A Dissertation
Presented to
The Academic Faculty

By

Noah H. Paulson

In Partial Fulfillment
Of the Requirements for the Degree
Doctor of Philosophy in Mechanical Engineering

Georgia Institute of Technology

August, 2017

STRUCTURE-PROPERTY LINKAGES FOR POLYCRYSTALLINE MATERIALS USING MATERIALS KNOWLEDGE SYSTEMS

Approved by:

Dr. Surya R. Kalidindi, Advisor
George W. Woodruff School of
Mechanical Engineering
Georgia Institute of Technology

Dr. David L. McDowell, Co-Advisor
George W. Woodruff School of
Mechanical Engineering
Georgia Institute of Technology

Dr. Richard W. Neu
George W. Woodruff School of
Mechanical Engineering
Georgia Institute of Technology

Dr. Hamid Garmestani
School of Materials Science
and Engineering
Georgia Institute of Technology

Dr. Donald S. Shih, Co-Advisor
Magnesium Research Center
Kumamoto University

Date Approved: May 4, 2017

ACKNOWLEDGMENTS

First, I would like to thank Dr. Surya R. Kalidindi for investing the significant time, effort and attention required to teach me what it means to be a rigorous researcher. I would also like to thank my co-advisors, Dr. David L. McDowell and Dr. Donald S. Shih for their support and guidance throughout this process. Thanks to my remaining committee members, Dr. Richard W. Neu and Dr. Hamid Garmestani, for providing fresh viewpoints on this research. Thank you to the National Science Foundation for funding this research through Grant No. CMMI-1333083.

It is important to thank Dr. Matthew W. Priddy for his significant contributions to this work through microstructure generation and response simulations and for numerous useful discussions and interactions. Thank you to Dr. Dipen K. Patel for immeasurable hours spent discussing ideas both new and old. Thanks also to Dr. Jordan S. Weaver, Dr. David B. Brough, Dr. Yuksel C. Yabansu, Ahmet Çeçen, Anne C. Hanna, David Montes De Oca Zapiain, Andrew Castillo, Dr. Evdokia Popova and Dr. Sepehr Saroukhani for many useful discussions and learning experiences.

Lastly, I would like to thank my partner, Madeline Hall, and my parents, Matthew and Jane Paulson, for supporting me throughout this endeavor.

TABLE OF CONTENTS

LIST OF TABLES

LIST OF FIGURES

NOMENCLATURE

3-D	Three Dimensional
CPFEM	Crystal Plasticity Finite Element Method
EVD	Extreme Value Distribution
FEM	Finite Element Method
FIP	Fatigue Indicator Parameter
F-S	Fatemi-Socie
GFS	Generalized Fourier Series
GSH	Generalized Spherical Harmonics
HCF	High Cycle Fatigue
MKS	Materials Knowledge System
MVE	Material Volume Element
PC	Principal Component
PCA	Principal Component Analysis
RVE	Representative Volume Element
SVE	Statistical Volume Element
S-P	Structure-Property

SUMMARY

Computational tools that are capable of rapidly exploring candidate microstructures and their associated properties are required to accelerate the rate of development and deployment of novel materials. In this work, a suite of computationally efficient protocols, based on the materials knowledge system (MKS) framework, are developed to evaluate the properties and performance of polycrystalline microstructures. In the MKS approach, physics-capturing coefficients (calibrated with microstructures and their responses obtained via experiments or simulations) store the microstructure-sensitive response of the material system of interest. Once calibrated, the linkages may be employed to predict the local responses (through localization) or effective properties (through homogenization) of new microstructures at low computational expense. Specifically, protocols are developed to predict bulk properties (elastic stiffness and yield strength), local cyclic plastic strains and resistance to fatigue crack formation and early growth (in the high cycle fatigue and transition fatigue regimes). These protocols are demonstrated on a diverse set of α-titanium microstructures, which exhibit heterogeneous microstructure features, in addition to anisotropy on multiple length-scales.

CHAPTER 1

INTRODUCTION

The current materials development process requires enormous investments of time and capital. The materials genome initiative (MGI) white paper [1] asserted that over twenty years typically elapse between the discovery and deployment of a new material. A major contributor to this glacial rate of progress is an overwhelming reliance on slow and expensive experiments to evaluate the properties of candidate materials. This task becomes even more daunting when it is recognized that materials may be simultaneously evaluated on the basis of multiple criteria; for example, both the elastic stiffness and the number of cycles to failure of a particular material may be of interest. The evaluation of each performance measure requires statistically significant numbers of experiments to be of practical use.

Computational approaches provide an opportunity to reduce the number of experiments required to characterize material performance. These typically take the form of physics-based models such as the spectral method [2, 3] or crystal plasticity finite element method (CPFEM) [4–6]. Such methods incorporate an arbitrary level of detail in the description of microstructure and any relevant materials physics. Unfortunately, these simulations often require significant computational resources. Alternatively, reduced-order models may be employed. These models typically incorporate less microstructural detail, yet involve a smaller computational investment. One common example is the Hall-Petch relationship, where the grain size in a microstructure is empirically related to its yield strength though a simple equation [7,

8]. Also commonly employed are Eshelby type solutions [9–12], where the response fields and effective properties of an inhomogeneity placed in a homogeneous medium are analytically or numerically evaluated. While models derived from the Eshelby solution solve physics-based constitutive relationships, their accuracy and scope are limited by simplifying assumptions made about the materials microstructure. Clearly, reduced-order models that incorporate comprehensive microstructure descriptors are required to accelerate the rate of exploration of material properties.

In recent years, Kalidindi and co-workers have developed the materials knowledge system (MKS) framework to establish reduced-order, microstructure-sensitive models [13–30]. Derived from statistical continuum theories [19, 31–33], the MKS framework addresses both homogenization [15, 18, 20, 22, 24, 27–30] and localization [13, 14, 16, 17, 19, 21, 23, 26] problems. In the MKS homogenization framework, microstructures are quantified using n-point spatial correlations [34–37] that are represented in a reduced-dimensional space using PCA [38]. The structure-property (S-P) linkage may then be calibrated using an ensemble of reduced-dimensional microstructure representations and their associated effective properties as obtained via experiments or previously-validated physics-based models. These protocols have been employed in the prediction of the transport properties of fuel cell materials [22] and the inelastic properties of dual-phase steels [24], in addition to numerous other examples. The framework has also been extended to processing-structure [28–30] and processing-structure-properties [27] linkages. In the MKS localization framework, microstructure response fields are predicted through the convolution of localization kernels (based on Green's functions) with a digital representation of the microstructure [13, 14, 16, 17, 19, 21, 23, 26]. As before, the localization kernels are calibrated with an ensemble of microstructure exemplars and their response fields as computed using physics-based models. The MKS localization approach has been successfully employed in the prediction of elastic and perfectly-plastic strain-rate fields in two-phase composite mi-

crostructures [13, 14, 17], microstructure evolution through spinoidal-decomposition in binary alloys [16, 26], and elastic strain fields in cubic and hexagonal polycrystalline microstructures [21, 23].

The overarching goal of this work is to develop protocols to predict the performance of polycrystalline microstructures in forms well suited to materials design and development efforts. Attainment of this goal requires the extension of the MKS framework in several regards. In polycrystalline materials, the local material state in each voxel is characterized by a crystal lattice orientation (defined by an ordered set of three Bunge-Euler angles). In previous attempts at the development of homogenization relationships for polycrystals [39, 40], the local state space (i.e., the orientation space) was binned, and the material was treated as a composite where each bin in the orientation space corresponded to a distinct local state. Unfortunately, this approach required a very large number of orientation bins to obtain a representation of satisfactory fidelity. In this work, an extension to the existing MKS framework is developed for homogenization S-P linkages through the use of generalized spherical harmonics (GSH) [41] for the functional components over the orientation space. It is demonstrated that this approach produces computationally-efficient, highly-compact representations of reduced-order S-P linkages for polycrystalline microstructures (specifically through the prediction of elastic stiffness and yield strength).

The GSH basis functions have been previously implemented in related problems [21, 23, 36, 42–44], including MKS localization linkages for the prediction of strain-component fields in cubic and hexagonal polycrystals [21, 23], where only 10 and 15 GSH basis functions, respectively, were required to accurately represent the functional dependence on crystal lattice orientation. In this work, the MKS localization framework is extended to rank-order the high cycle fatigue (HCF) resistance of polycrystalline materials. First the MKS is employed to predict full tensorial elastic strain fields in the microstructures. Stresses are then computed using Hooke's Law and are

subsequently employed to estimate cyclic plastic strains through numerical integration of a crystal plasticity flow rule. Surrogate measures of the local driving force for fatigue crack formation and early growth, referred to as fatigue indicator parameters (FIPs) are then computed from these field quantities. Microstructures can then be rank-ordered for resistance to HCF by their extreme value distributions (EVDs) of FIP responses.

In addition to employing the MKS framework for the prediction of local fatigue responses, the MKS homogenization framework is extended to rank-order the fatigue resistance of polycrystalline materials. As before, microstructures are quantified using spatial statistics and represented in a reduced-dimensional space. The fatigue response in this approach is characterized by the parameters obtained by fitting a selected functional form to the EVD of FIPs. Consequently, both the microstructures and associated fatigue responses have reduced-order representations well suited to materials development efforts. These protocols are demonstrated in the characterization of the HCF and transition fatigue performance of polycrystalline materials.

The protocols developed through this work are demonstrated on α-titanium polycrystals - a material system of particular relevance to the NSF GOALI project funding this research. The α-titanium system is complex, exhibiting orientation-dependent elastic and plastic anisotropy at the grain-scale in addition to varied microstructure topology at higher length-scales [6, 45]. Each protocol developed in this work relies on a common set of synthetic microstructures generated via DREAM.3D [46]. Furthermore, all simulations rely on the crystal plasticity framework developed by McDowell and co-workers over the past two decades [6, 47–51].

CHAPTER 2

EXECUTIVE SUMMARY

This dissertation is organized as a compilation thesis, where publication-quality research articles written by the candidate are tied together by an executive summary. This section briefly introduces the background of the work and presents each of the research topics with some selected findings. Furthermore, the executive summary draws general conclusions from the entire work that may not be apparent in the separate examination of each article's findings.

2.1 Background

2.1.1 Digital Microstructure Representation

In the MKS framework, experimental and synthetic microstructures are mathematically represented using the microstructure function [19, 36, 52]. To properly characterize the microstructure, it is important to identify which physical characteristics of the local microstructural features are expected to have a significant impact on the response of interest. This set of characteristics, called the local state, may include determiners such as phase, chemical composition, crystal structure and dislocation density. In this work, the local state only refers to a single physical characteristic and is denoted by h. The microstructure function, $m(h, \boldsymbol{x})$, captures the probability density of finding local state h (within a region of Δh around h) at the spatial location $\boldsymbol{x}$ in the microstructure.

The next step is to select a form by which to represent the microstructure function. The most logical choice is to utilize a generalized Fourier series (GFS), which has the benefit of flexibility; any desired level of detail can be incorporated into the description of microstructure feature geometries and local states. In reality, the fidelity of the experimental characterization of microstructure is limited; digital imaging techniques generally return a rasterized representation of the microstructure with a characteristic minimum resolved length-scale. In composite microstructures, where the local state is suitably characterized by a limited number of distinct phases, the most suitable GFS is given by

$$m(h, \boldsymbol{x})\Delta h \approx \sum_{n=1}^{N} \sum_{\boldsymbol{s}=\boldsymbol{1}}^{\boldsymbol{S}} M_{\boldsymbol{s}}^{n} \chi_n(h) \chi_{\boldsymbol{s}}(\boldsymbol{x}) \tag{2.1}$$

where $M_{\boldsymbol{s}}^{n}$ are the GFS coefficients, Δh is the size of the local state bin and $\chi_i(\ )$ is the indicator basis function. The indicator basis returns zero unless its argument is within the bin indexed by i, in which case it returns one. Note that $\boldsymbol{s}$ is a multidimensional array index and that N and $\boldsymbol{S}$ are the maximum number of phases and spatial locations in the microstructure, respectively. In this simple GFS, $M_{\boldsymbol{s}}^{n}$ is the volume fraction of the local state h in the spatial bin indexed by $\boldsymbol{s}$.

The GFS presented in Equation (2.1) is effective for the representation of composite microstructures; however, other local state descriptors such as composition or orientation necessitate the implementation more sophisticated basis functions that efficiently represent continuous functions. Sections 3.4 and 4.3.2 present the implementation of the GSH Fourier basis for the microstructure function's dependence on the crystalline lattice orientation in polycrystalline materials.

2.1.2 Spatial Statistics

Metrics must be employed in the construction of reduced-order homogenization relationships to characterize microstructures so that their differences can be quantified. Images of microstructure (such as the digital representations described in Section

2.1.1) are not sufficient as they cannot be directly compared mathematically. Typically, statistical microstructure descriptors such as grain size and volume fraction are utilized in structure-property linkages [7, 8, 53]. These simple metrics are often selected based on the expertise of the researcher and do not account for long-range interactions between microstructure features that can often have a significant effect on the response of interest. N-point spatial correlations [34–37] provide an opportunity to characterize both the lower- and higher-order spatial relationships between microstructure features and inherently capture a majority of the ad-hoc metrics employed in the literature.

In this work, 2-point spatial correlations are used to quantify material microstructure. The most fundamental form of the 2-point statistics is given by

$$f(h, h'|\boldsymbol{r}) = \frac{1}{Vol(\Omega_{\boldsymbol{r}})} \int_{\Omega_{\boldsymbol{r}}} m(h, \boldsymbol{x}) m(h', \boldsymbol{x} + \boldsymbol{r}) d\boldsymbol{x} \tag{2.2}$$

where $\Omega_{\boldsymbol{r}}$ is the integration domain and $f(h, h'|\boldsymbol{r})$ is the conditional probability density that a vector $\boldsymbol{r}$, randomly placed in the microstructure, has local states h and h' at the head and tail of the vector, respectively. Note that $\Omega_{\boldsymbol{r}}$ depends on the choice of $\boldsymbol{r}$ in non-periodic microstructures because the integration domain must contain $\boldsymbol{x} + \boldsymbol{r}$ for all $\boldsymbol{x}$.

Given the form of Equation (2.2), it is natural to substitute the GFS representation of the microstructure function. For a multi-phase composite material, Equation (2.1) is substituted, resulting in

$$f(h, h'|\boldsymbol{r})[\Delta h]^2 \approx \sum_{p=1}^{N} \sum_{n=1}^{N} \sum_{\boldsymbol{t}} F_{\boldsymbol{t}}^{np} \chi_n(h) \chi_p(h') \chi_{\boldsymbol{t}}(\boldsymbol{r}) \tag{2.3a}$$

$$F_{\boldsymbol{t}}^{np} = \frac{1}{|\boldsymbol{S_t}|} \sum_{\boldsymbol{s}=\boldsymbol{1}}^{\boldsymbol{S_t}} M_{\boldsymbol{s}}^{n} M_{\boldsymbol{s}+\boldsymbol{t}}^{p} \tag{2.3b}$$

where $F_{\boldsymbol{t}}^{np}$ are the GFS coefficients for Equation (2.2), $\boldsymbol{t}$ is a multidimensional vector

index for $\boldsymbol{r}$ and $\boldsymbol{S_t}$ bounds the set of indices for spatial bins contained in $\Omega_{\boldsymbol{r}}$ [25, 54]. A similarly simple expression that is better suited to polycrystalline materials may be obtained through the substitution of the microstructure function defined using GSH basis functions into Equation (2.2) (as demonstrated in Section 3.4).

2.1.3 MKS Origins

Details of the development of the MKS framework from statistical continuum theories are presented in previous work [15, 18, 22, 24, 25, 55–57] for both linear and non-linear physical phenomena; however, it is most instructive to begin the discussion with the case of linear-elasticity in composite microstructures. The development begins with an examination of a microstructure volume subject to the following constraints:

$$\nabla \cdot \boldsymbol{\sigma} = \mathbf{0} \tag{2.4a}$$

$$\nabla \times \boldsymbol{\varepsilon} = \mathbf{0} \tag{2.4b}$$

$$\boldsymbol{\sigma} : \boldsymbol{\varepsilon} \geq \mathbf{0} \tag{2.4c}$$

where $\boldsymbol{\varepsilon}$ and $\boldsymbol{\sigma}$ are the strain and stress tensors, respectively.

For this linear-elastic problem, the constitutive relationship between stress and strain at each location in the volume is described by Hooke's Law,

$$\boldsymbol{\sigma}(\boldsymbol{x}) = \boldsymbol{C}(\boldsymbol{x}) : \boldsymbol{\varepsilon}(\boldsymbol{x}) \tag{2.5}$$

where $\boldsymbol{C}(\boldsymbol{x})$ is the elastic stiffness tensor at spatial position $\boldsymbol{x}$. It is convenient to decompose $\boldsymbol{C}$ and $\boldsymbol{\varepsilon}$ as

$$\boldsymbol{C}(\boldsymbol{x}) = \boldsymbol{C}_R + \boldsymbol{C}'(\boldsymbol{x}) \tag{2.6a}$$

$$\boldsymbol{\varepsilon}(\boldsymbol{x}) = \overline{\boldsymbol{\varepsilon}} + \boldsymbol{\varepsilon}'(\boldsymbol{x}) \tag{2.6b}$$

where $\boldsymbol{C}_R$ is a selected reference stiffness and $\overline{\boldsymbol{\varepsilon}}$ is the average of $\boldsymbol{\varepsilon}$ over the entire microstructure. In this problem, it is desirable to obtain the polarization tensor, $\mathbf{a}(\boldsymbol{x})$, such that

$$\boldsymbol{\varepsilon}'(\boldsymbol{x}) = \mathbf{a}(\boldsymbol{x}) : \overline{\boldsymbol{\varepsilon}} \tag{2.7}$$

To derive $\mathbf{a}(\boldsymbol{x})$, Equation (2.6a) and Equation (2.6b) are first substituted into Equation (2.5). Through the utilization of the Green's function and recursive substitution, the following expression for $\mathbf{a}(\boldsymbol{x})$ is obtained,

$$\begin{aligned} \mathbf{a}(\boldsymbol{x}) = &- \int_{\Omega} \boldsymbol{\Gamma}(\boldsymbol{x} - \boldsymbol{x}') : \boldsymbol{C}'(\boldsymbol{x}') d\boldsymbol{x}' + \\ &\int_{\Omega} \boldsymbol{\Gamma}(\boldsymbol{x} - \boldsymbol{x}') : \boldsymbol{C}'(\boldsymbol{x}') : \int_{\Omega} \boldsymbol{\Gamma}(\boldsymbol{x}' - \boldsymbol{x}'') : \boldsymbol{C}'(\boldsymbol{x}'') d\boldsymbol{x}'' d\boldsymbol{x}' + \ldots \end{aligned} \tag{2.8}$$

where $\boldsymbol{\Gamma}(\boldsymbol{x} - \boldsymbol{x}')$ is a symmetrized derivative of the Green's function. This analytical expression for $\mathbf{a}(\boldsymbol{x})$ is a critical component in the development of both homogenization (Section 2.1.4), and localization relationships (Section 2.1.5).

2.1.4 MKS Homogenization

One branch of the MKS protocols is concerned with the determination of effective properties given detailed microstructure information and loading conditions. Continuing the example from Section 2.1.3, it is hypothesized that a homogenization relationship may be developed for the effective elastic stiffness tensor, $\boldsymbol{C}^{eff}$, where

$$\overline{\boldsymbol{\sigma}} = \boldsymbol{C}^{eff} : \overline{\boldsymbol{\varepsilon}} \tag{2.9}$$

according to Hooke's Law. The volume averaged stress ($\overline{\boldsymbol{\sigma}}$) and strain ($\overline{\boldsymbol{\varepsilon}}$) in Equation (2.9) are defined by the following relationships:

$$\overline{\boldsymbol{\sigma}} = \frac{1}{V(\Omega)} \int_{\Omega} \boldsymbol{\sigma}(\boldsymbol{x}) d\boldsymbol{x} \tag{2.10a}$$

$$\overline{\boldsymbol{\varepsilon}} = \frac{1}{V(\Omega)} \int_{\Omega} \boldsymbol{\varepsilon}(\boldsymbol{x}) d\boldsymbol{x} \tag{2.10b}$$

$\boldsymbol{C}^{eff}$ may be expressed as a function of $\boldsymbol{C}$ and the localization tensor of Equation (2.8) [25] as follows

$$\boldsymbol{C}^{eff} = \overline{\boldsymbol{C}} + \overline{\boldsymbol{C} : \mathbf{a}} \tag{2.11}$$

where the over-bar represents a volumetric average. Through the representation of $\boldsymbol{C}(\boldsymbol{x})$ with a GFS and the substitution of Equation (2.8) into Equation (2.11), $\boldsymbol{C}^{eff}$ may be expressed as follows,

$$\boldsymbol{C}^{eff} = \overline{\boldsymbol{C}} - \int_{\Omega_{\boldsymbol{r}}} \int_{H} \int_{H} \boldsymbol{\Gamma}(\boldsymbol{r}) : [\boldsymbol{C}(h) m(h, \boldsymbol{x})] : [\boldsymbol{C}'(h') m(h', \boldsymbol{x} + \boldsymbol{r})] \, d\boldsymbol{r} dh dh' + \dots \tag{2.12}$$

where $\boldsymbol{r} = \boldsymbol{x} - \boldsymbol{x}'$ and H bounds the local state space. One advantage of Equation (2.12) is that $\boldsymbol{\Gamma}(\boldsymbol{r})$, $\boldsymbol{C}(h)$ and $\boldsymbol{C}'(h')$ depend solely on the physical characteristics of the materials system and that $m(h, \boldsymbol{x})$ and $m(h', \boldsymbol{x} + \boldsymbol{r})$ only depend on the specific topology of the microstructure of interest. Furthermore, in Equation (2.12) $m(h, \boldsymbol{x})$ and $m(h', \boldsymbol{x} + \boldsymbol{r})$ form the 2-point spatial statistics, $f(h, h' | \boldsymbol{r})$, which provide an easily comparable and qualitative description of microstructure.

Unfortunately, evaluation of the triple integral in Equation (2.12) is difficult and sensitive to the selection of $\boldsymbol{C}_R$. Through a reconfiguration of Equation (2.12) and a truncation of the higher-order terms in the series, the following relationship is extracted,

$$\boldsymbol{C}^{eff} \approx \overline{\boldsymbol{C}} - \sum_{\boldsymbol{r}, n, p} \boldsymbol{\Upsilon}_{\boldsymbol{r}}^{np} F_{\boldsymbol{r}}^{np} \tag{2.13}$$

where $F_{\boldsymbol{r}}^{np}$ are the GFS coefficients for $f(h, h'|\boldsymbol{r})$ (see Equation (2.3b)) and $\boldsymbol{\Upsilon}_{\boldsymbol{r}}^{np}$ are physics-capturing coefficients. In theory, $\boldsymbol{\Upsilon}_{\boldsymbol{r}}^{np}$ could be calibrated with an ensemble of microstructure exemplars and their associated responses as predicted by established physics-based models; however, this would require the determination of a large set of coefficients. Fortunately, principal component analysis (PCA) may be used to reduce the dimensionality of $F_{\boldsymbol{r}}^{np}$. PCA finds orthogonal and linear combinations of the original feature data such that they are ordered from highest to lowest variance [38]. Through PCA, a microstructure instantiation may be represented in principal component (PC) space with high fidelity using many orders of magnitude fewer dimensions than in the original representation. Before presenting the PC decomposition, a simplified notation for $F_{\boldsymbol{r}}^{np}$ is established. The GFS coefficients will be denoted by $F_t^{(j)}$, where t indexes combinations of $(\boldsymbol{t}, n, p)$ and j indexes individual microstructure exemplars. With this definition in place, the reduced-dimensional representation of $F_t^{(j)}$ is given by

$$F_t^{(j)} = \sum_{i=1}^{min(J-1,R)} \alpha_i^{(j)} \phi_{it} + \overline{F}_t \tag{2.14}$$

where $\alpha_i^{(j)}$ are the coordinates of the exemplar indexed by j in PC space (denoted PC scores), ϕ_{it} represent the directions of maximum variance determined by PCA (denoted PC directions), $\overline{F}_t$ is an average over the spatial statistics of all exemplars and J and R represent the maximum number of microstructure exemplars and features in the GFS coefficients, respectively. By employing the full set of PC scores, exemplars may be represented with no loss of fidelity. In some cases, however, it is desirable to take further advantage of PCA and represent the spatial statistics with only a handful of PC scores. In that case, the maximum number of PC components used in the representation of $F_t^{(j)}$ is denoted $\tilde{R}$.

Using the results of Equation (2.14), Equation (2.13) may be simplified as follows

$$\boldsymbol{C}^{eff} \approx \boldsymbol{A}_0 + \sum_{i=1}^{\tilde{R}} \boldsymbol{A}_i \alpha_i \tag{2.15}$$

where $\boldsymbol{A}_i$ are physics-capturing coefficients which describe the dependence of $\boldsymbol{C}^{eff}$ on the PC scores. Through a calibration of the $\boldsymbol{A}_i$ coefficients with a diverse set of exemplars and their associated $\boldsymbol{C}^{eff}$ tensors, $\boldsymbol{C}^{eff}$ may be predicted for new microstructures in the materials system. This prediction is often achieved at far lower computational cost than required using existing models. As mentioned in Section 2.1.3, this procedure is applicable to a wide range of properties, depending on both linear and non-linear material phenomena. Furthermore, examining the problem from a machine-learning perspective allows one to recognize the PC scores as *features*, the products of which may be taken to form higher-order features. This enables the construction of S-P linkages where the predicted properties have non-linear dependence on the PC scores.

2.1.5 MKS Localization

In the context of MKS, localization describes the prediction of local response fields given microstructure topology and a higher length-scale deformation state. In keeping with the current derivation for elastic deformation in a composite microstructure, the local elastic strain fields may be described by the following relationship,

$$\boldsymbol{\varepsilon}(\boldsymbol{x}) = \boldsymbol{a}(\boldsymbol{x}) : \overline{\boldsymbol{\varepsilon}} = (\boldsymbol{I} + \mathbf{a}(\boldsymbol{x})) : \overline{\boldsymbol{\varepsilon}} \tag{2.16}$$

where $\boldsymbol{I}$ is the fourth-rank identity tensor, $\mathbf{a}(\boldsymbol{x})$ is the polarization tensor of Equation (2.8), and $\boldsymbol{a}(\boldsymbol{x})$ is the localization tensor [19, 25]. Through the introduction of a GFS in the representation of $\boldsymbol{a}(\boldsymbol{x})$, invoking the ergodic hypothesis and substituting $\boldsymbol{r} = \boldsymbol{x} - \boldsymbol{x}'$ and $\boldsymbol{r}' = \boldsymbol{x}' - \boldsymbol{x}''$, Equation (2.16) can be expanded into the following

form,

$$\boldsymbol{\varepsilon}(\boldsymbol{x}) = \Big(\boldsymbol{I} - \int_H \int_{\Omega_{\boldsymbol{r}}} \boldsymbol{\alpha}(h,\boldsymbol{r}) m(h,\boldsymbol{x}+\boldsymbol{r}) dh d\boldsymbol{r} + \int_H \int_H \int_{\Omega_{\boldsymbol{r}}} \int_{\Omega_{\boldsymbol{r}}} \tilde{\boldsymbol{\alpha}}(h,h',\boldsymbol{r},\boldsymbol{r}') m(h,\boldsymbol{x}+\boldsymbol{r}) m(h',\boldsymbol{x}+\boldsymbol{r}+\boldsymbol{r}') dh dh' d\boldsymbol{r} d\boldsymbol{r}' - \ldots \Big) : \langle \boldsymbol{\varepsilon} \rangle \tag{2.17}$$

where $\boldsymbol{\alpha}(h,\boldsymbol{r})$ and $\tilde{\boldsymbol{\alpha}}(h,h',\boldsymbol{r},\boldsymbol{r}')$ are the first- and second-order influence functions (both fourth-rank tensors) [19, 25] and $\langle\ \rangle$ is the ensemble average. As in the homogenization example, the physics of the materials system and the specific microstructure topology are independently captured by the influence functions and microstructure function, respectively. The influence functions are analogous to the Green's function and describe the contribution to $\boldsymbol{\varepsilon}(\boldsymbol{x})$ due to the presence of local state h at the spatial location $\boldsymbol{x}+\boldsymbol{r}$.

Unfortunately, the influence functions of Equation (2.17) are notoriously difficult to evaluate analytically. The MKS approach avoids these difficulties through a calibration of the influence functions with sets of diverse microstructure exemplars and their response fields as evaluated using previously-validated physics-based models. To enable the efficient calibration of the localization relationship, GFS representations of the microstructure function and the first-order influence function, given by

$$m(h,\boldsymbol{x})\Delta h \approx \sum_n \sum_{\boldsymbol{s}} M^n_{\boldsymbol{s}} \chi_n(h) \chi_{\boldsymbol{s}}(\boldsymbol{x}) \tag{2.18a}$$

$$\boldsymbol{\alpha}(h,\boldsymbol{r})\Delta h \approx \sum_n \sum_{\boldsymbol{t}} \boldsymbol{A}^n_{\boldsymbol{t}} \chi_n(h) \chi_{\boldsymbol{t}}(\boldsymbol{r}) \tag{2.18b}$$

respectively, are substituted into Equation (2.17), resulting in a generalized equation for MKS localization [25]:

$$\boldsymbol{\varepsilon}_{\boldsymbol{s}} \approx \Big(\sum_n \sum_{\boldsymbol{t}} \boldsymbol{A}^n_{\boldsymbol{t}} M^{n*}_{\boldsymbol{s}+\boldsymbol{t}} + \sum_n \sum_{n'} \sum_{\boldsymbol{t}} \sum_{\boldsymbol{t}'} \boldsymbol{A}^{nn'}_{\boldsymbol{t}\boldsymbol{t}'} M^{n*}_{\boldsymbol{s}+\boldsymbol{t}} M^{nn'*}_{\boldsymbol{s}+\boldsymbol{t}+\boldsymbol{t}'} + \ldots \Big) : \langle \boldsymbol{\varepsilon} \rangle \tag{2.19}$$

Once the GFS coefficients of the influence functions have been determined, the MKS can predict the response fields of new microstructures in the materials system, often at significantly lower cost than with the original physics-based model. In one study, the MKS was shown to predict elastic strain fields nearly 360 times faster than FEM in 2-phase composite microstructures [14].

2.1.6 Fatigue Indicator Parameters

Computational evaluation of the fatigue performance of polycrystalline metals is an appealing alternative to the numerous costly tests required for the experimental determination of fatigue life. Unfortunately, computational fatigue modeling is a complex endeavor due to the variety of physical mechanisms which act at different length- and time-scales [58]. The growth of long cracks in polycrystalline metals is well described by the stress intensity factor from linear-elastic fracture mechanics (LEFM) [59] in addition to other energy-, stress- and strain-based relationships [60]. In contrast, the driving forces for fatigue crack formation and early growth are highly dependent on local, directional, cumulative plastic slip, in addition to the local stress and elastic strain [58, 61]. These field responses are directly controlled by the local microstructure. It is critical to effectively characterize this driving force, as a large proportion of the fatigue life is occupied by the formation and growth of small cracks [62].

Fatigue indicator parameters (FIPs) are surrogate measures of the driving force for fatigue crack formation and early growth [62]. FIPs may take different forms depending on the dominant mechanisms in the material of interest, yet all depend on local microstructure responses. The Fatemi-Socie (F-S) FIP has been shown to correlate with fatigue crack formation and early growth in the LCF and HCF regimes under multi-axial loading [60, 62–64]. The F-S FIP in particular is effective for metals

which undergo planar slip (such as titanium) [51]. The F-S FIP is given by

$$FIP_{FS} = \frac{\Delta\bar{\gamma}^p_{max}}{2}\left[1 + k\frac{\bar{\sigma}^n_{max}}{\sigma_y}\right], \tag{2.20}$$

where $\Delta\gamma^p_{max}$ is the maximum cyclic plastic shear strain range, σ^n_{max} is the maximum stress normal to $\Delta\gamma^p_{max}$, σ_y is the macroscopic material yield strength and k is a constant which controls the impact of normal stress (typically ranging between 0.5 and 1.0). The over-bar on the shear strain and normal stress represents a volume averaging of the field quantities over a limited length-scale, generally a small number of voxels [65].

Locations in the microstructure with severe FIP responses are most likely to be the sites of crack formation. Furthermore, microstructures with numerous severe FIP locations can be expected to be more susceptible to fatigue crack formation and growth than microstructures with fewer and less severe extreme FIP locations. In several previous studies, microstructures have been rank-ordered by their resistance to HCF through the extreme value distributions (EVDs) of their FIP responses as computed using CPFEM simulations [66–68].

2.2 Dataset Generation

Throughout this work, common sets of microstructure volumes and simulation techniques are employed in multiple studies. It is advantageous to expend less effort on obtaining the datasets than on the development of protocols. Microstructures and their responses are employed both to calibrate S-P linkages and to validate their predictive capabilities. The material system studied in this work is polycrystalline α-titanium, which exhibits significant microstructure heterogeneity in addition to elastic and inelastic anisotropy on multiple length-scales. Details of the generation of microstructures and the crystal plasticity model employed in this work are discussed

in the subsequent sections.

2.2.1 Microstructure Generation

To best demonstrate the protocols developed in this work, a diverse set of microstructures with a wide range of properties are obtained. Due to the scarcity of detailed three-dimensional characterizations of α-titanium microstructures in the literature, synthetic microstructures are generated that are differentiated predominantly by their texture. The twelve selected microstructures have textures inspired by 2-dimensional EBSD scans [69] as well as textures in the literature [70–73]. Furthermore, a log-normal grain size distribution is assigned with a mean grain size of $30\mu m$ and a standard deviation of $15\mu m$.

For each target microstructure, a set of 500 synthetic volumes are generated. These exemplars, named material volume elements (MVEs), are intended for the calibration and validation of S-P linkages. MVEs must be large enough to capture the maximum length-scale of interaction between distinct features in the microstructure. Fortunately, the MKS influence coefficients in localization problems capture the decaying strength of interaction between microstructure features separated by increasing distance. In numerous previous studies with low to medium contrast in local properties for both elastic and inelastic responses, it was demonstrated that 21x21x21 voxel MVEs are sufficiently large to allow these interactions to fully decay [13, 14, 17, 21, 23, 74]. This size of MVE is selected in this work with a side length of $210\mu m$.

Synthetic MVEs are generated for each target microstructure using the open-source DREAM.3D software package [46]. From the microstructure dimensions and target grain size distribution, DREAM.3D constructs synthetic microstructure volumes through an ellipsoidal packing algorithm. Orientations are subsequently assigned to individual grains to match the target texture. Grain ID maps and (0001)

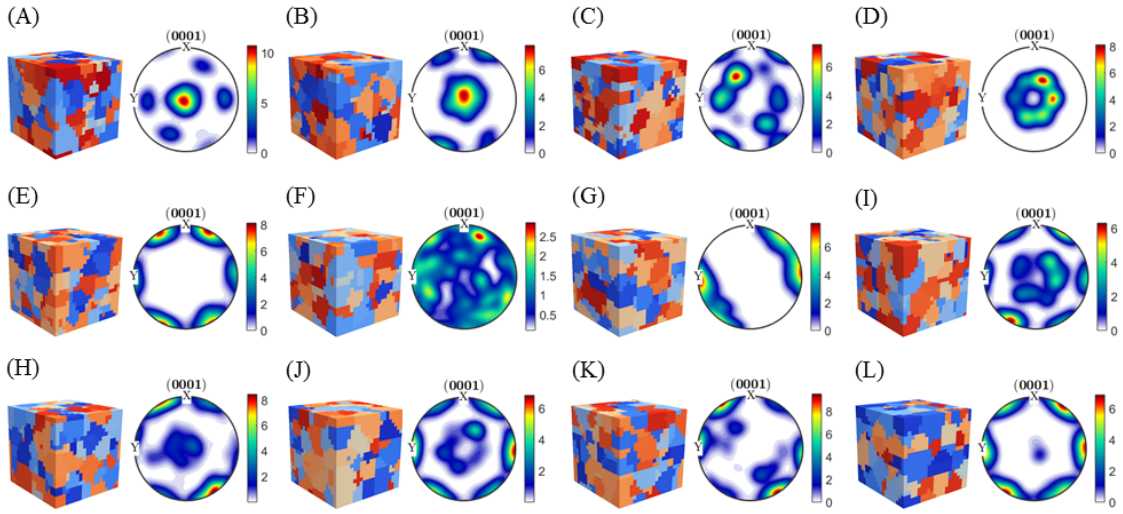

Figure 2.1: Grain ID maps and (0001) pole figures of sample MVEs for microstructures A through L.

pole figures are presented in Figure 2.1 for an example MVE from each of the twelve target microstructures (labeled A through L). Note that the MVE ensembles employed in this work were generated over the course of several studies [74–76].

2.2.2 Crystal Plasticity Simulations

Crystal plasticity simulations are employed in this work to generate the requisite data for the calibration and validation of structure-property linkages. The crystal plasticity framework was developed by McDowell and coworkers over the past two decades for the Ti-6Al-4V material system [6, 47–51]. The framework is implemented in ABAQUS [77] through a user-material subroutine in addition to single-point calculations. Further details, including the elastic and inelastic material parameters, are provided in Section 4.3.1.

The performance of this framework has been extensively validated in prior work. In one recent study, Smith et al. calibrated the crystal plasticity model parameters with monotonic and cyclic experimental results for β-annealed Ti-6Al-4V at different loading rates and strain amplitudes [6]. Cyclic stress-strain curves were subsequently

compared between an experiment and associated CPFEM simulation (for a loading condition not employed in the calibration set) to validate the parameter set. In a later study, the framework was employed to rank-order the HCF performance of different titanium microstructures following the protocols introduced in Section 2.1.6 [69]. In that work, it was demonstrated that coupled CPFEM and extreme value FIP analyses reproduce experimentally observed trends in fatigue performance with respect to crystallographic texture, grain size and loading direction in Ti-6Al-4V. These studies are emphasized to justify the use of CPFEM simulations to validate the results of this work. The quality of an S-P linkage cannot exceed the quality of the data used for its calibration. Consequently, it is most informative to validate the S-P linkages resulting from this work with CPFEM results and not experimental results.

2.3 Summary of Findings

2.3.1 MKS Homogenization Protocols to Predict the Bulk Properties of Polycrystalline Microstructures

In this study, protocols are developed to predict the bulk properties of polycrystalline microstructures using the MKS homogenization framework. Specifically, elastic stiffness and yield strength are evaluated for the 12 α-titanium microstructures discussed in Section 2.2.1. The ensemble of MVEs (and their associated properties as predicted via CPFEM simulations) used to calibrate the S-P linkages consists of 30 MVEs each from microstructures A through G. The ensemble used to validate the linkages (i.e. evaluate their predictive capability versus CPFEM simulations) consists of 30 (different) MVEs each from microstructures A through G and 30 MVEs each from microstructures H through L. Microstructures H through L are called validation microstructures because they are not employed in the calibration of the S-P linkage.

In annealed polycrystals, the local state of interest is the crystal lattice orientation, g, which is a function of three Bunge-Euler angles. Consequently, should a binning approach be used to represent the functional dependence of the spatial statistics on orientation (as presented in Section 2.1.2), the MKS framework would be burdened with a huge number of orientation bins. Instead, generalized spherical harmonic (GSH) basis functions are employed to represent the functional dependence on crystal lattice orientation. This choice results in massive computational savings versus the naive binning approach.

These benefits are most obvious after PCA is employed to reduce the dimensionality of the spatial statistics of each polycrystalline MVE. Figure 2.2 presents the cumulative explained variance (where the explained variance in each PC dimension is given by the variance of the PC scores of all calibration MVEs in that dimension) for increasing numbers of PC dimensions and for a given truncation in the number of GSH basis functions (denoted by $\tilde{L}$) used in the GFS representation of the spatial statistics. Notice that with increasing $\tilde{R}$, the percentage cumulative explained variance asymptotically approaches 100%. To emphasize the compaction achieved, notice that 85% of the variance is explained for spatial statistics represented by 15 GSH basis functions (this was shown in previous work to be the complete set required to represent functional dependence of elastic properties on GSH [19, 21, 52, 76, 78, 79]) and only two PCs.

Furthermore, as demonstrated in Figure 2.3, MVEs are well clustered by their associated target microstructure in the first two PC dimensions. MVEs which are nearby in PC space exhibit similar structures, while well separated MVEs have significantly different structures. Referring back to Figure 2.1, the example MVEs from neighboring microstructures K and L both have strong transverse texture, while the example MVE from microstructure D (which is far from K and L in PC space) has basal texture.

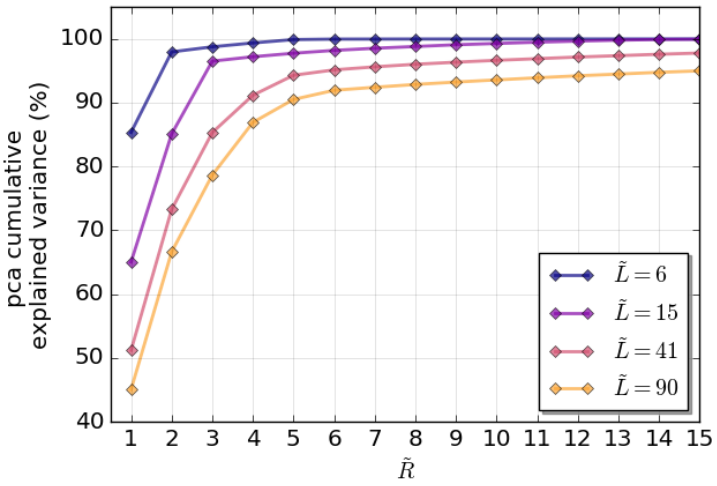

Figure 2.2: Percentage PCA explained variance versus $\tilde{R}$ and $\tilde{L}$.

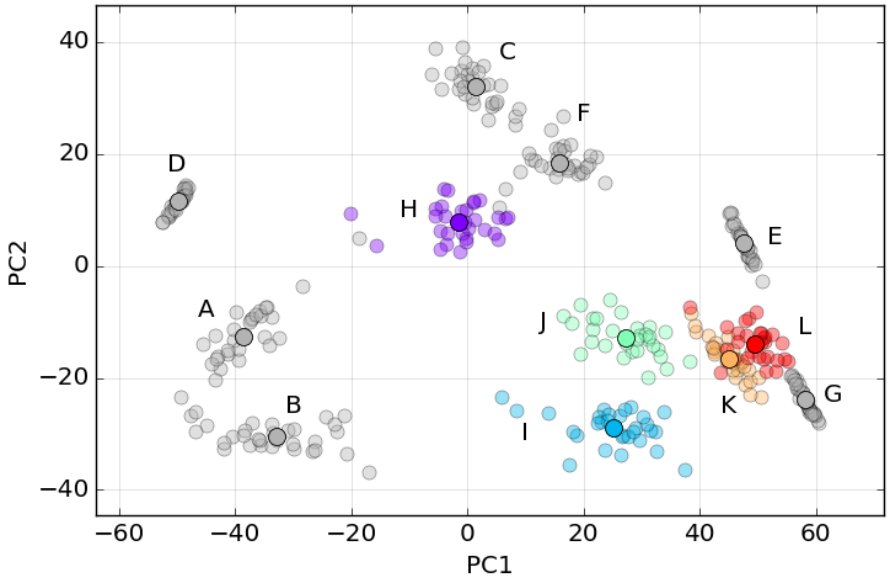

Figure 2.3: The full ensemble of MVEs in PC1 and PC2 (for $\tilde{L} = 15$). MVEs employed for the calibration of the PC space and the S-P linkages are colored gray.

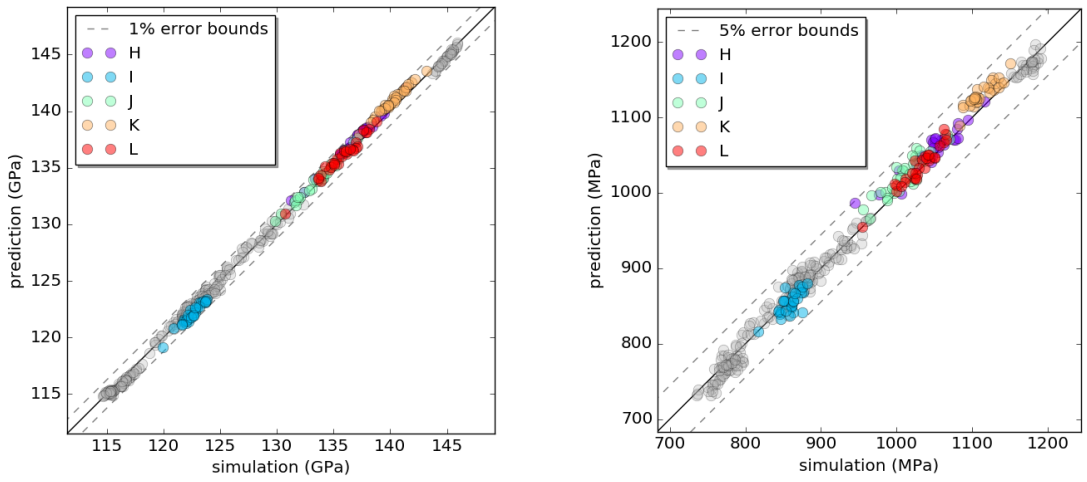

(a) (b)

Figure 2.4: Predicted versus simulated response for (a) elastic stiffness with 3 PCs and (b) yield strength with 6 PCs. Grey markers are for validation MVEs generated with target microstructure statistics for microstructures A through G.

After the application of PCA, the physics-capturing coefficients of Equation (2.15) are calibrated using reduced-dimensional representations of the calibration MVEs and their effective properties as predicted via CPFEM simulations. To identify the final form of the S-P linkage, the values of $\tilde{R}$ and $\tilde{L}$ mostly likely to provide high predictive capability in a reduced-order form are selected. The final S-P linkages in this study are specified by $\tilde{R} = 3$ and $\tilde{L} = 15$ for elastic stiffness and $\tilde{R} = 6$ and $\tilde{L} = 41$ for yield strength. The results of this study are presented in Figure 2.4, where the property obtained via CPFEM simulation is compared against the property predicted by the reduced-order S-P linkage for each MVE in the validation set. Both linkages consistently predict the effective properties with a high degree of accuracy, even for MVEs associated with microstructures in the validation set (such MVEs are highlighted in color).

Finally, it is important to emphasize the computational benefits of this approach. In the prediction of yield strength, the reduced-order protocols enabled nearly a 10,000 times speed-up in required CPU time versus CPFEM simulations per MVE (note

that the linkage must be employed for MVEs that are not significant extrapolations beyond the calibration MVEs). The computational efficiency and simplicity of this framework have the potential to greatly aid both forward and inverse materials design tasks. Furthermore, they are expected to be a crucial component in efforts aimed at the dramatic reduction of the time and cost required to develop and deploy novel polycrystalline materials.

2.3.2 MKS Localization Protocols to Rank-Order the High Cycle Fatigue Resistance of Polycrystalline Microstructures

In this study, a novel localization approach is developed to rank-order the HCF resistance of polycrystalline microstructures. This approach relies on the assumption that in HCF, plastic strains are small in magnitude and localized to specific features of the microstructure [62]. Consequently, the elastic strains (and therefore stresses) can be directly computed using linear-elastic simulations and the cyclic plastic strains can be separately estimated in each voxel through a forward Euler scheme. Crucially, this approach is far more computationally efficient than traditional CPFEM when an MKS localization linkage is used to predict the elastic strains.

Traditionally, a representative volume element (RVE) is selected for the analytical or numerical evaluation of the properties of a microstructure (in this case HCF performance). The size of the RVE (and the number of features it contains), must be selected such that it is statistically representative of the microstructure [80]. Specifically, it is required that the properties of interest are not sensitive to the specific sample of microstructure selected or to a small increase in its size. Unfortunately, the RVE for fatigue properties is expected to be prohibitively large for analysis using existing physics-based models. Kanit et al. [80] suggested an alternate approach where a set of smaller statistical volume elements (SVEs) replace the single RVE. Each SVE must be large enough to capture the maximum length-scale of interaction between

microstructure features. In this work, the MVEs discussed in Sec 2.2.1 are employed as SVEs to approximate the RVE for HCF performance. Through an examination of the convergence of effective elastic stiffness for x-, y- and z-direction loading, it was determined that the SVE ensemble for each microstructure should include 500 SVEs.

As in previous studies [66, 67, 69], the HCF analysis is performed for fully-reversed cyclic loading (R=-1) up to 0.5% strain amplitude (or roughly 60-67% of the strain to yielding). Three loading cycles are performed to allow the cyclic plastic strains to saturate before the F-S FIPs are computed. Displacement-controlled, periodic boundary-conditions are employed in the x-, y- and z-directions for uniaxial strain. As a first step, the MKS influence coefficients are calibrated using an ensemble of polycrystalline MVEs and their elastic strain fields as obtained via linear-elastic FEM simulations. These influence coefficients are employed to efficiently predict the tensorial elastic strain fields in the ensembles of SVEs at both the minimum and maximum of a loading cycle. The MKS approach takes 0.7 seconds to compute strain fields in each SVE. The equivalent linear-elastic FEM simulation would require ten minutes to perform. Stress fields are subsequently computed from the strain fields using Hooke's Law.

Next, a decoupled algorithm is used to compute the plastic strains in the SVEs throughout the three loading cycles. First, the stress at each voxel location is resolved onto the HCP slip systems. Then, numerical integration is performed on the crystal plasticity flow rule (see Section 4.3.1) throughout three loading cycles to obtain the cumulative plastic shear strains at each time step. The plastic strain tensor at the minimum and maximum of the third loading cycle are computed from the cumulative plastic shear strains. The success of this approach is demonstrated in Figure 2.5, where ϵ_{11}^{p} strain fields at the maximum of the third loading cycle are compared between the predictions of the novel protocols and a traditional CPFEM simulation. As the plastic strains can vary by orders of magnitude, the strain fields are plotted

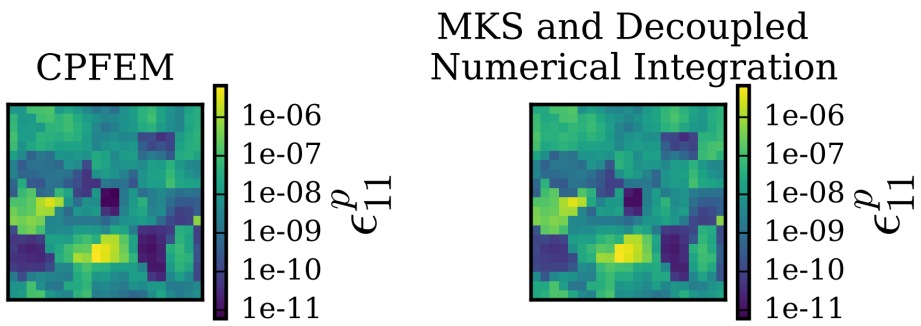

Figure 2.5: A two-dimensional cross-section comparison of the ϵ_{11}^p values from CPFEM (left) and MKS plus numerical integration (right).

with a log-scaled color-scheme.

Next, the F-S FIPs are computed for all voxel locations in each SVE according to Equation (2.20). To construct the extreme value distributions of the FIP responses, the maximum-valued FIP from each SVE in the ensemble is extracted. Through the comparison of these FIP EVDs, the resistance to fatigue crack formation and growth can be rank-ordered for different microstructures and loading conditions. Figure 2.6 compares the FIP EVDs between the novel protocols and CPFEM simulation results for a set of 100 SVEs belonging to the β-annealed microstructure (labeled A in Figure 2.1). In general, the results of the novel protocol and CPFEM match closely; loading in the x- and y-directions results in similar FIP EVDs and loading in the z-direction results in a more severe FIP response (representing greater susceptibility to HCF). These protocols are also demonstrated on microstructures B, F and G for x-, y- and z-direction loading.

These protocols do indeed provide significant computational benefits versus traditional CPFEM simulations; an approximate speed-up of 40 times is achieved. Furthermore, this approach is able to extract accurate simulation results from 6000 SVEs without the use of ABAQUS simulations.

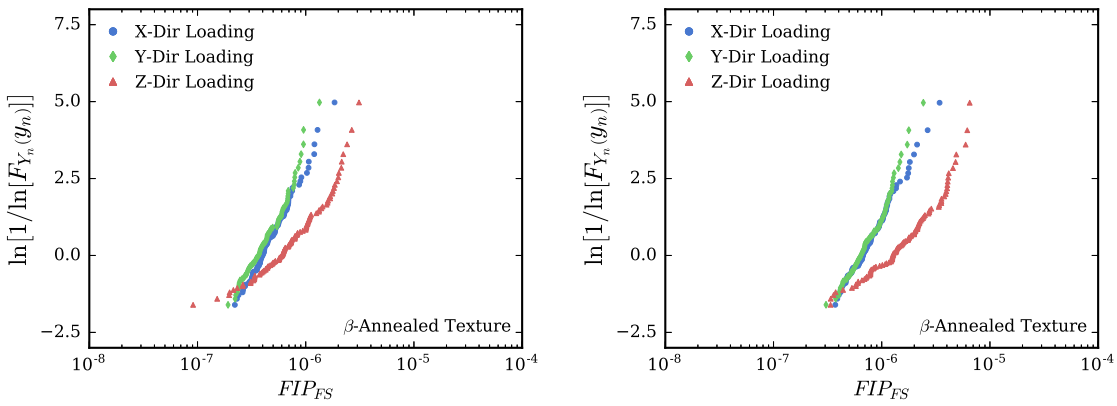

(a) (b)

Figure 2.6: Comparison of the β-annealed microstructure extreme value distribution Fatemi-Socie FIP plot with 100 SVEs for (a) MKS plus numerical integration and (b) CPFEM.

2.3.3 MKS Homogenization Protocols to Rank-Order the High Cycle Fatigue Resistance of Polycrystalline Microstructures

In this study, the MKS homogenization framework is extended to rank-order the HCF resistance of polycrystalline microstructures. While the goals of this and the previous study are similar, in this work, reduced-order representations of the microstructures and their associated HCF performance are employed. This formulation enables the accelerated optimization of microstructures for target properties in materials development efforts. The full set of 500 MVEs for each of the twelve microstructures are utilized, for a total of 6000 MVEs. Instead of using CPFEM to obtain the field quantities used to compute FIPs, the protocols described in Section 2.3.2 are employed. This choice dramatically reduced the cost of obtaining the set of calibration and validation simulations, as the results for 8 of the microstructures were available from previous studies [74, 75]. Simulations are performed for three cycles of fully reversed uniaxial loading in the x-direction to 0.5% strain amplitude.

The basic elements of this framework are similar to those of the MKS homogenization framework for the prediction of bulk properties, except that details of the

representation of both the microstructure and the property of interest differ significantly. As in Section 2.3.2, each microstructure is represented by an ensemble of SVEs. Consequently, reduced-order representations of the microstructure must include the mean structure in addition to some measure of the variation exhibited in the SVE ensemble. Furthermore, the HCF performance of the microstructure is represented by the distribution of discrete, extreme-valued FIP responses in the SVE ensemble. To characterize the HCF performance in a reduced-order manner, the FIP EVDs are fit to some pre-selected distribution, and the resultant fitting parameters (herein called performance characteristics) serve as the effective properties in the MKS homogenization linkage. Specifically, the gamma distribution given by

$$f\left(z|\,\alpha\right) = \frac{1}{\Gamma\left(\alpha,0\right)} z^{\alpha-1} e^{-z} \tag{2.21a}$$

$$F\left(z|\,\alpha\right) = \frac{\Gamma\left(\alpha,z\right)}{\Gamma\left(\alpha,0\right)} \tag{2.21b}$$

$$\Gamma\left(\alpha,z^*\right) = \int_{z^*}^{\infty} z^{\alpha-1} e^{-z} dz, \qquad z = \frac{x-\mu}{\sigma}, \qquad \alpha > 0 \tag{2.21c}$$

is employed, where α, μ and σ control the shape, location and spread of the distribution, respectively, $f\left(z|\,\alpha\right)$ is the probability density function (PDF) and $F\left(z|\,\alpha\right)$ is the cumulative distribution function (CDF) [68, 81]. The FIP EVD can therefore be represented by the three performance characteristics, α, μ and σ. Instead of selecting the maximum FIP in each SVE as in Section 2.3.2, the FIP EVD is constructed by taking a threshold on the distribution of all FIPs in the ensemble of SVEs (in this case the threshold is the top 1% of all FIPs). Note that α and σ have competing effects on the shape of the EVD in the ranges of interest. Consequently, a reasonable value for α is selected and held constant prior to identifying μ and σ.

In practice, the first step in the construction of the linkage is to compute the 2-point spatial correlations (with the functional dependence on the local state captured by the GSH basis functions as in Section 2.3.1) of all SVEs under consideration. Next,

the reduced-dimensional PC space is established for SVEs in the calibration ensemble (in this case SVEs associated with all microstructures introduced in Section 2.2.1 except for microstructure J) and the spatial statistics for all SVEs are transformed into this space. Each microstructure is represented by the mean set of coordinates in PC space and the total variance, given by

$$VAR_{tot} = \sum_{i=1}^{\tilde{R}} var(\alpha_i^{(j)}) \tag{2.22}$$

where the variances of the PC scores for the SVEs are computed in each PC dimension and summed.

It now becomes clear that only 11 data points (corresponding to the 11 calibration microstructures) are available to calibrate the S-P linkage. One option is to generate more synthetic microstructures and perform physics-based simulations to obtain their responses. Unfortunately, this would require significant effort and computational expenditure. Alternately, it is proposed that the SVE ensemble for each microstructure may be sub-sampled to establish numerous unique SVE subsets from each original microstructure SVE ensemble. The first step in such an approach is to establish the minimum number of SVEs required to approximate an RVE. In this study, it was determined that 100 SVEs are sufficient by examining the convergence of α, μ and σ with the inclusion of increasing numbers of SVEs. Given this information, SVE subsets are selected that exhibit significant diversity of mean PC locations and variances.

Once a sufficient number of data-points are obtained (in this study 220 subsets are extracted from the 11 original microstructure ensembles), the physics-capturing coefficients of the S-P linkage may be calibrated. To capture the potentially sophisticated dependence of the performance characteristics on the reduced-dimensional representations of microstructure, truncation levels of $\tilde{R} = 25$ and $\tilde{L} = 41$ are selected and

Table 2.1: The top ten features ranked by the Pearson correlation are presented for both performance characteristics.

Feature Ranking	μ	Pearson Correlation	σ	Pearson Correlation
1	$\overline{PC}_1 \cdot \overline{PC}_7$	-0.654	$\overline{PC}_1 \cdot \overline{PC}_7$	-0.730
2	$\overline{PC}_1 \cdot \overline{PC}_5$	0.647	$\overline{PC}_1 \cdot \overline{PC}_5$	0.639
3	$\overline{PC}_7$	0.586	$\overline{PC}_6$	0.590
4	$\overline{PC}_6$	0.574	$\overline{PC}_7$	0.588
5	$\overline{PC}_7 \cdot VAR_{tot}$	0.547	$\overline{PC}_6 \cdot VAR_{tot}$	0.529
6	$\overline{PC}_5 \cdot \overline{PC}_6$	0.535	$\overline{PC}_7 \cdot VAR_{tot}$	0.518
7	VAR_{tot}	0.519	$\overline{PC}_3 \cdot \overline{PC}_5$	0.517
8	$\overline{PC}_6 \cdot VAR_{tot}$	0.515	$\overline{PC}_1 \cdot \overline{PC}_{25}$	0.514
9	${VAR_{tot}}^2$	0.495	${\overline{PC}_1}^2$	-0.506
10	$\overline{PC}_1 \cdot \overline{PC}_{25}$	0.491	$\overline{PC}_5$	-0.472

2nd order combinations of features are allowed. To down-select from this large set of 378 features, Pearson correlations are employed [82] to identify which features are likely to contribute most to the prediction of the performance characteristics. The top ten features for both μ and σ are provided in Table 2.1 along with their Pearson correlations. Notice that certain features frequently arise in both lists; this is likely due to the high degree of correlation between the performance characteristics (the Pearson correlation between of μ and σ is 0.941).

The specific number of features included in the S-P linkage is determined through an examination of the calibration and cross-validation errors (as briefly discussed in Section 2.3.1). As a result, 61 and 50 features are selected for μ and σ, respectively. The final FIP EVDs are reconstructed using Equation (2.21) and the performance characteristics are predicted by the S-P linkage. The results of this study are presented in Figure 2.7, where the true FIP EVDs (on the left) are compared to those predicted by the MKS homogenization linkage (on the right) for the 12 original microstructures. Clearly, the ranking of the FIP EVDs (and therefore resistance to HCF) is preserved in the new approach with high accuracy, even for microstructure J (which was not included in the set of calibration microstructures).

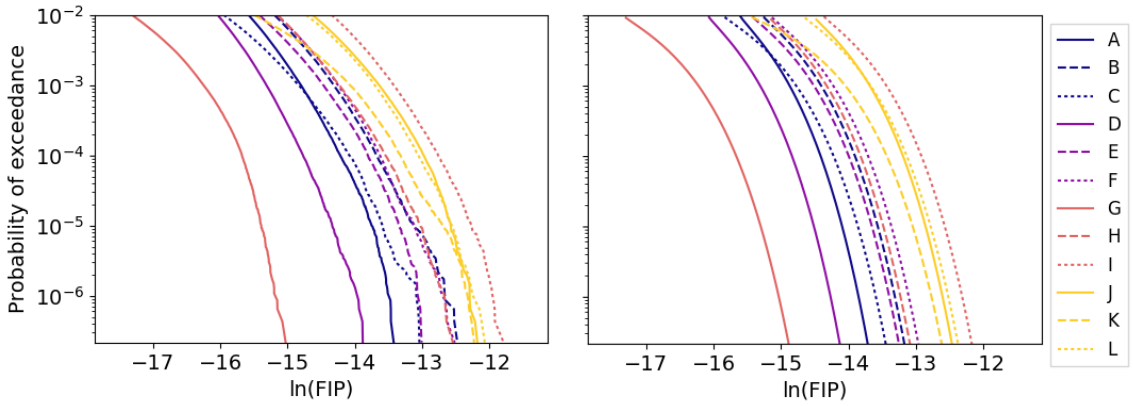

(a) (b)

Figure 2.7: FIP EVDs extracted from (a) the original simulations, and (b) the novel MKS protocols are plotted for microstructures A through L.

Furthermore, the computational savings of the MKS homogenization protocols versus the traditional CPFEM approach are massive. Only 6 hours are required to predict the FIP EVDs for the 12 microstructures using the novel MKS homogenization framework. In contrast, the equivalent set of 6000 CPFEM simulations would require 18,000 hours of CPU time. This is more than a 3000 times reduction. This drastic computational savings and the reduced-order representation of both microstructures and their performance enables the rapid exploration of microstructures for improved HCF resistance.

2.3.4 MKS Homogenization Protocols to Rank-Order the Transition Fatigue Resistance of Polycrystalline Microstructures

Given the successes of the new MKS protocols in rank-ordering the HCF resistance of polycrystalline materials (see Section 2.3.2 and Section 2.3.3), it is desirable to demonstrate their robustness in a different fatigue regime. While plastic strains are very small in HCF, in the transition fatigue regime they are similar in magnitude to elastic strains [58, 83]. Furthermore, nearest neighbor interactions are expected to be significant, made evident by phenomena such as the redistribution of cyclic stress

and strain. Unfortunately, these characteristics are not compatible with the major assumptions of the framework described in Section 2.3.2; namely that the plastic strains are small and not subject to nearest neighbor interactions. In contrast, the framework described in Section 2.3.3 requires no such assumptions. In this study, that same framework is employed to construct FIP EVDs for the transition fatigue regime without modification (except for certain model parameters).

In this study, cyclic CPFEM simulations are performed to obtain the stress and plastic strain fields required to compute FIPs. These are used to construct the FIP EVDs required for the calibration and validation of the S-P linkage. These simulations are performed to 0.75% strain amplitude, or roughly 90-99% of the strain to yielding. Three cycles of fully-reversed loading are applied using displacement-controlled, periodic boundary-conditions for uniaxial stress in the x-direction. First, CPFEM simulations were performed for 500 MVEs associated from microstructure I. From these results, it was determined that 150 MVEs are required to approximate an RVE based on the convergence of α, μ and σ. To enable the subset selection algorithm described in Section 2.3.3, CPFEM simulations were performed for 300 MVEs associated with each of the remaining microstructures.

The remaining protocols in the calibration and validation of the S-P linkage are identical to those described in Section 2.3.3. The results of this study are presented in Figure 2.8, with the CPFEM predicted FIP EVDs on the left and the FIP EVDs predicted by the MKS homogenization protocols on the right. This figure demonstrates that the protocols reliably rank-order the FIP EVDs for all twelve microstructures with only several slight exceptions (for example, the rank-ordering of microstructures A and B is reversed at a high probability of exceedance). Furthermore, the predictive capabilities of the linkage are similar to the previous linkage for HCF. This indicates that the GSH spatial statistics and PCA are well suited to account for the local cyclic plastic strain in both fatigue regimes, and for the significant stress and strain

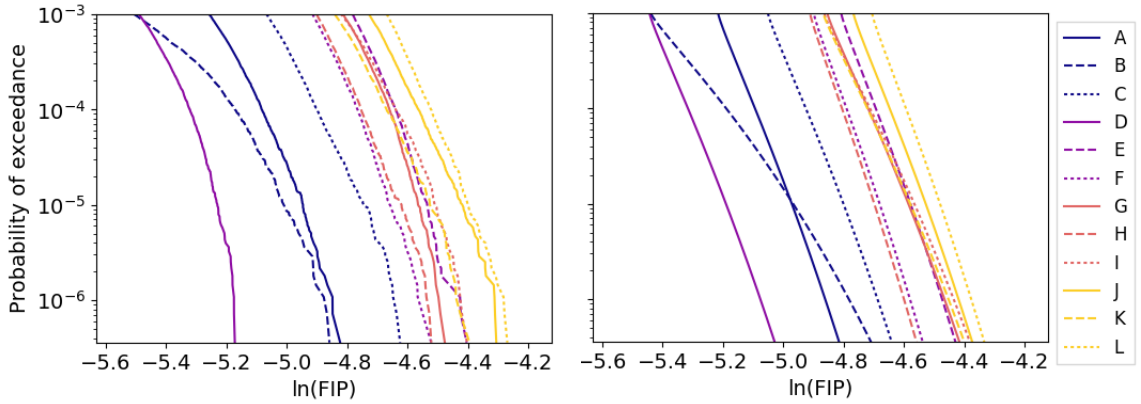

(a) (b)

Figure 2.8: FIP EVDs are plotted for each of the twelve microstructures extracted using (a) the original simulations, and (b) the novel MKS protocols.

redistribution (and nearest neighbor interactions) exhibited in the transition fatigue regime.

It is also worth taking this opportunity to compare these HCF performance rankings with a previous experimental characterization. In a study by Peters et al. [70], the fatigue strengths of three different Ti-6Al-4V microstructures were evaluated for cyclic loading in the transverse and rolling directions (our x- and y-directions, respectively). Notably, in that study, the microstructures employed had very similar grain morphologies (homogeneous equiaxed with a small α-phase grain size of 1-2μm), yet had distinct textures. These microstructures, labeled basal, basal-transverse, and transverse most closely match the B, D and G labeled microstructures in this study, respectively. After 10^7 cycles of fully reversed (R=-1) loading in the x-direction, the basal, basal-transverse and transverse microstructures had fatigue strengths of 620 MPa, 690 MPa and 590 MPa, respectively. This is similar to the results achieved in this work, where microstructures B and D perform comparably well while microstructure G performs worse than both. It is noted that these comparisons should not be taken too seriously, as the microstructures employed in this transition fatigue work only contain the α-phase and likely exhibit significantly higher levels of inelastic

deformation.

The computational advantages of the MKS protocols are even more dramatic for transition fatigue analyses than for HCF. This is due to the time-consuming nature of CPFEM simulations in the transition fatigue regime. The MKS protocols provide more than a 22,000 times speed-up in CPU time versus traditional methods (for new microstructures in the same material system that are not significant extrapolations beyond the calibration microstructures). The success of these protocols for both HCF and transition fatigue demonstrate the wide applicability of the approach, and encourage the exploration of similar protocols for other extreme-value phenomena.

2.3.5 Conclusions

In this work, a diverse suite of tools are developed to evaluate the properties and performance of polycrystalline materials using MKS homogenization and localization approaches. Each approach provides remarkable reductions in the expense of performing computational property analysis. Furthermore, these protocols demonstrate the versatility of the MKS framework for polycrystalline materials. Both elastic and inelastic material performance is captured in addition to complex extreme-value phenomena driven by the behavior of materials under cyclic loading. Furthermore, reduced-order representations of microstructures and performance are extensively investigated to aid the rapid exploration of material structures for desired properties.

Throughout this dissertation work, it was necessary to employ simple synthetic microstructures and the results of crystal plasticity simulations to efficiently develop and demonstrate the capabilities of the MKS framework. In future work, however, it would be highly desirable to obtain a diverse set of experimentally obtained microstructures and responses. This would enable the calibration of S-P linkages directly applicable to the design and development of next-generation polycrystalline microstructures with improved bulk properties and fatigue performance. Furthermore, future studies

should employ this framework to construct linkages to characterize other extreme value phenomena, including damage, fracture and void formation. Lastly, further improvements to the linkages presented in this dissertation work could be achieved through the implementation of more advanced machine learning algorithms for dimensionality reduction, linkage selection and the quantification of uncertainty propagated through the linkage.

CHAPTER 3

MKS HOMOGENIZATION PROTOCOLS TO PREDICT THE BULK PROPERTIES OF POLYCRYSTALLINE MICROSTRUCTURES

This work was accepted by the journal Acta Materialia on March 6, 2017 and first made available on March 8th, 2017 [76]. The title of the paper is *Reduced-order structure-property linkages for polycrystalline microstructures based on 2-point statistics*. The order of authorship is as follows: Noah H. Paulson, Matthew W. Priddy, David L. McDowell and Surya R. Kalidindi.

3.1 Abstract

Computationally efficient structure-property (S-P) linkages (i.e., reduced order models) are a necessary key ingredient in accelerating the rate of development and deployment of structural materials. This need represents a major challenge for polycrystalline materials, which exhibit rich heterogeneous microstructure at multiple structure/length scales, and exhibit a wide range of properties. In this study, a novel framework is described for extracting S-P linkages in polycrystalline microstructures that are obtained using 2-point spatial correlations (also called 2-point statistics) to quantify the material's microstructure, and principal component analysis (PCA) to represent this information in a reduced dimensional space. Additionally, it is demonstrated that the use of generalized spherical harmonics (GSH) as a Fourier basis for

functions defined on the orientation space leads to a compact and computationally efficient representation of the desired S-P linkages. In this study, these novel protocols are developed and demonstrated for elastic stiffness and yield strength predictions for $\alpha-$Ti microstructures using a dataset produced through microscale finite element simulations.

3.2 Introduction

Materials development and deployment efforts require evaluation of the properties of large sets of potential material internal structures (generically referred to as microstructures; this description also includes information regarding chemical composition at the relevant length scales) [25, 52, 84–94]. Currently, experiments and simulations are used for such analyses at a high cost, severely limiting the extent of the materials design spaces explored [1, 95]. In addition, most of the current approaches (e.g., finite element models) employed in modeling and simulation are not readily invertible, i.e., it isn't easy to determine a candidate microstructure given a set of desired properties. Reduced order models are critical to the acceleration of materials discovery and development, as they enable high throughput exploration of the materials design spaces for rapid down selection [19, 25, 87, 88, 96, 97]. In this work, we specifically focus on reduced order structure-property (S-P) linkages for polycrystalline microstructures that exhibit rich heterogeneity in the spatial distribution of the crystal lattice orientation at the mesoscale (also referred to as grain-scale). These microstructures exhibit strongly anisotropic elastic and inelastic properties at the macroscale [3, 11, 19, 23, 43, 52, 79, 98–105].

It is important to pursue the development of reduced order models within the context of established physically-based theories. There is indeed a rich literature on homogenization theories for polycrystalline microstructures that can be used to guide the development of surrogate models. For elastic stiffness or compliance components,

the foundational concepts can be traced back to the elementary bounds established by Voigt [106], Reuss [107], and Hill [108], as well as the more sophisticated self-consistent approaches of Kroner [10], which leverage Eshelby's solution [9]. For inelastic properties, analogous foundations can be traced to the works of Taylor [109] and Sachs [110]. Detailed discussion of these theories cast in a modern continuum mechanics framework can be found in Nemat-Nasser and Mori [111], Milton [57], Mura [53], Qu and Cherkaoui [112] and Roters [5].

The central limitation of the theories mentioned above is that they can only incorporate a very limited amount of information regarding the material microstructure. To date, microstructural information included in the application of established composite theories to polycrystalline microstructures has largely been limited to the orientation distribution (also called texture) in the sample, and in some cases, averaged shape factors (based on idealizing the grains as ellipsoids) [11, 12]. The main exception to these statements comes in the form of statistical continuum theories formulated originally by Brown [31] for electrical properties of materials, and subsequently introduced by Volkov and Klinskikh [113], Lomakin [114], and Beran and Molyneux [115] for mechanical properties. These ideas have been further refined in later years by Beran [32, 116], Kröner [33, 117, 118], Torquato [119–121], Adams [19, 35, 36], and others [55, 56, 122–124]. A unique feature of this formulation is that the effective property is expressed as a series expansion, where each term represents a contribution of a specific microstructural attribute expressed in the formalism of n-point statistics [34–37]. In some cases, the pre-factor for each term in the series can be evaluated using known Green's functions [19, 56]. Most importantly, this approach allows one to include as much detail of the material microstructure as one wishes in arriving at the homogenized properties of interest.

The sophisticated higher-order homogenization theories mentioned above have encountered some difficulties in their implementation. First, the Green's functions

required for the implementation of these theories are only available for a limited number of physical phenomena. Second, the convergence of the series is rather slow for high contrast composites [40, 119]. Over the past decade, Kalidindi and coworkers [13–19, 21–26, 74] have developed a novel data science approach that still utilizes the basic mathematical formulation of the statistical continuum theories, and circumvents the central impediments mentioned above by employing modern data science tools. Mainly, it has been shown that the elusive pre-factors (related to Green's functions) in the series expansion can be calibrated to results from numerical simulations (e.g., performed using finite element models). This new framework for establishing S-P linkages has been referred as materials knowledge systems (MKS), and has addressed both homogenization (bottom-up) [15, 18, 22, 24], and localization (top-down) problems [13, 14, 16, 17, 21, 23, 26, 74]. It is clarified here that the term "MKS framework" in our prior work was used exclusively with the latter linkages. However, since both the homogenization and localization linkages developed in this new data science framework share the same foundations (they both come from the same statistical continuum theories discussed earlier), we will henceforth refer to both homogenization and localization linkages established using this approach as MKS linkages.

In the MKS framework, the homogenization S-P linkages (reduced-order models) [15, 18, 22, 24, 25] connect the microstructure descriptors (inputs) to the effective macroscale properties (outputs). These linkages are typically expressed in the form of a polynomial series. The input microstructure descriptors are generally based on principal component analysis (PCA) [38] of the 2-point spatial correlations obtained from all the microstructures in the ensemble studied. The outputs have frequently included elastic stiffness or compliance components and the yield strength. Much of the prior work has been limited to materials with multiple distinct phases [15, 18, 22, 24, 25].

The main goal of this work is to extend the MKS homogenization framework to

polycrystalline microstructures, where the local material state in each voxel is characterized by a crystal lattice orientation (defined by an ordered set of three Euler angles). Prior attempts [39, 40] in this direction have binned the local state space (i.e., the orientation space) and treated the material as a composite; each bin in the orientation space corresponded to a distinct local state. However, this approach requires a very large number of orientation bins in order to obtain a representation of satisfactory fidelity. In this work, we will develop an extension to the existing MKS framework for homogenization S-P linkages by using generalized spherical harmonics (GSH) [41] for the functional components over the orientation space. We will specifically demonstrate that this approach produces computationally efficient, highly compact representations of reduced-order S-P linkages for polycrystalline microstructures. Note that GSH have already been used successfully in related problems [23, 36, 42–44], including certain MKS localization linkages [21, 23, 74]. The efficiency and efficacy of the new approach developed and presented in this work is specifically demonstrated through the predictions of the elastic stiffness and yield strengths in a variety of α-titanium microstructures. It is emphasized that S-P linkages can only attempt to match the physics of whatever process was used to produce the set of calibration data. Consequently, the linkages in this work are calibrated using the results of CPFE simulations on synthetic microstructures, and the success of this approach is evaluated by comparing against results of that same model.

3.3 Current Theoretical Framework

In order to construct S-P linkages, microstructural information must be presented in a form that allows for a rigorous quantitative comparison. Unfortunately, images of microstructure cannot fulfill this role in their raw representations. In other words, a pixel by pixel comparison of two random microstructures, either from the same sample or from different samples, will not reveal useful information. Traditionally,

metrics such as grain size distributions and phase volume fractions have been used to capture the salient microstructural information [7, 8]. However, these approaches do not consider the complexities of the microstructure geometry with sufficient fidelity for many properties of interest. In recent years, Kalidindi and co-workers have employed 2-point spatial correlations to evaluate microstructural distances [37], cluster microstructures [15, 20], and to provide a basis for the construction of S-P linkages [18, 22, 24]. This higher order statistical representation of microstructure precludes the need to manually select microstructure features (and potentially introduce bias) in the construction of S-P linkages; the 2-point spatial correlations already include many of the conventionally defined metrics of the microstructure.

Following the framework developed by Adams et al. [19, 36, 52], the microstructure in hierarchical materials systems can be mathematically captured through the function $m(h, \boldsymbol{x})$, which reflects the probability density of finding local state h (within an incremental Δh around h) at the spatial location $\boldsymbol{x}$. In this formalism, h and $\boldsymbol{x}$ are both treated as continuous variables. However, in practice it is much more useful to employ a discretized description of the microstructure function. Moreover, most experimental characterization techniques recover only a discretized description of the microstructure (as a consequence of the resolution limits of the equipment). Recognizing this, Adams et al. [19, 36, 52] have proposed a discretized description of the microstructure function $M_{\boldsymbol{s}}^n$ based on primitive binning of both the spatial domain and the local state space, i.e.,

$$m(h, \boldsymbol{x})\Delta h \approx \sum_{n=1}^{N} \sum_{\boldsymbol{s}=\boldsymbol{1}}^{\boldsymbol{S}} M_{\boldsymbol{s}}^n \chi_n(h) \chi_{\boldsymbol{s}}(\boldsymbol{x}) \tag{3.1}$$

where the indicator function $\chi_i(\ )$ is defined such that it is equal to one if and only if the argument belongs to the bin labeled i and zero otherwise, and Δh denotes the size of the local state bin employed. An important consequence of this definition is

that $M_{\boldsymbol{s}}^n$ has a very simple interpretation - it is essentially the volume fraction of local states belonging to the bin n (in the local state space) present in the bin $\boldsymbol{s}$ (in the spatial domain). It is important to recognize that both n and $\boldsymbol{s}$ are simply indices that point to a specific local state and spatial bin (i.e., voxel), respectively.

Although $M_{\boldsymbol{s}}^n$ has a simple interpretation and provides a useful description of the microstructure, it alone does not provide the salient information on the topological features of the microstructure. For this, one has to compute the spatial correlations. The most systematic approach to quantifying the spatial correlations in a given microstructure is through the use of the n-point spatial correlations framework [18, 34, 37, 55, 119, 125–127]. The most basic spatial correlations can be computed in the form of 2-point statistics formally expressed as

$$f(h, h'|\boldsymbol{r}) = \frac{1}{Vol(\Omega_{\boldsymbol{r}})} \int_{\Omega_{\boldsymbol{r}}} m(h, \boldsymbol{x}) m(h', \boldsymbol{x} + \boldsymbol{r}) d\boldsymbol{x} \tag{3.2}$$

In Equation (3.2), $f(h, h'|\boldsymbol{r})$ denotes the 2-point statistics reflecting the conditional probability density associated with finding the local state h at the spatial location $\boldsymbol{x}$ and the local state h' at the spatial location $\boldsymbol{x} + \boldsymbol{r}$. As before, $f(h, h'|\boldsymbol{r})[\Delta h]^2$ denotes the corresponding conditional probability. Note that the volume examined in evaluating the integral (denoted $\Omega_{\boldsymbol{r}}$) is expected to depend on the choice of $\boldsymbol{r}$ (this is because of the need to know the local states at both spatial locations $\boldsymbol{x}$ and $\boldsymbol{x}+\boldsymbol{r}$). For the same reasons that were mentioned earlier, a much more practical form of the 2-point spatial correlations is a discretized version expressed as

$$f(h, h'|\boldsymbol{r})[\Delta h]^2 \approx \sum_{p=1}^{N} \sum_{n=1}^{N} \sum_{\boldsymbol{t}} F_{\boldsymbol{t}}^{np} \chi_n(h) \chi_p(h') \chi_{\boldsymbol{t}}(\boldsymbol{r}) \tag{3.3}$$

Once again, the discretized version $F_{\boldsymbol{t}}^{np}$ has a simple physical interpretation - it captures the conditional probability of finding ordered local states belonging to bins n and p (in the local state space) in spatial bins whose centers are separated by the set

of vectors indexed by $\boldsymbol{t}$. Further details and a rigorous treatment of this framework can be found in Ref. [36]. The discretized forms of the microstructure function and the 2-point spatial correlations are indeed related by the following simple relation:

$$F_{\boldsymbol{t}}^{np} = \frac{1}{|\boldsymbol{S_t}|} \sum_{\boldsymbol{s}=\boldsymbol{1}}^{\boldsymbol{S_t}} M_{\boldsymbol{s}}^{n} M_{\boldsymbol{s}+\boldsymbol{t}}^{p} \tag{3.4}$$

Specific attention needs to be afforded to several details of Equation (3.4) before one endeavors to implement it in a computational algorithm: (i) the mapping of the vector $\boldsymbol{r}$ to the index $\boldsymbol{t}$ needs to follow specific protocols such as those outlined in Ref. [36], (ii) the earlier discussion regarding $\Omega_{\boldsymbol{r}}$ translates to $\boldsymbol{S_t}$ to identify the set of valid trials involved in evaluating $F_{\boldsymbol{t}}^{np}$, which depends on the vector index $\boldsymbol{t}$ [54], (iii) it is often convenient to employ multidimensional index arrays for $\boldsymbol{s}$ and $\boldsymbol{t}$ to naturally index the spatial bins in 2-D and 3-D microstructures [25], and (iv) $|\boldsymbol{S_t}|$ denotes the total number of spatial bins involved when $\boldsymbol{s}$ is used as a multidimensional array index.

For a complete representation of $f(h, h'|\boldsymbol{r})$ from equation (3.3), $F_{\boldsymbol{t}}^{np}$ must be calculated for all $\boldsymbol{t}$, n and p. Depending on the size of the microstructure and choice of basis functions, this set can be large and unwieldy. For example, $F_{\boldsymbol{t}}^{np}$ contains close to one-million features for a 3-dimensional microstructural sample with 21 elements per edge and 10 local state bins. At this stage, data-science techniques can be applied to reduce the dimensionality of the problem. One approach is to use principal component analysis (PCA), which is a distance-preserving linear transformation. PCA finds orthogonal and linear combinations of the original features such that they are ordered from highest to lowest contributors to the variance in the dataset [38]. Let $j = 1, 2, ..., J$ index the individual elements (i.e., microstructure exemplars) in the dataset being studied. Let $\{F_t^{(j)}|t = 1, 2, .., R\}$ denote a vectorized set of all spatial statistics of interest for a single microstructure exemplar. As an example, this set

might include all of the 2-point statistics computed from Equation (3.4) for all combinations of ($\boldsymbol{t}$, n, p). This set can also include higher-order spatial statistics (e.g., 3-point statistics), if deemed essential for the specific study. R denotes the total number of features (i.e., microstructure measures) included in the analysis. With this notation, PCA allows an orthogonal decomposition of $F_t^{(j)}$ as

$$F_t^{(j)} = \sum_{i=1}^{\min((J-1),(R))} \alpha_i^{(j)} \varphi_{it} + \overline{F}_t \tag{3.5}$$

where φ_{it} are the PC basis vectors, $\alpha_i^{(j)}$ are the transformed coordinates of the exemplar in the space spanned by the PC basis vectors, and $\overline{F}_t$ is ensemble average of $F_t^{(j)}$. Note that the maximum number of principal components is limited by the smaller value of R and $(J-1)$. However, in most practical applications, only a handful of $\alpha_i^{(j)}$ (called PC scores) are employed in the reduced-order representation of the original dataset. This representation may be written as $\{\alpha_i^{(j)} | i = 1, 2, ..., \tilde{R}\}$, where the truncation level $\tilde{R}$ is objectively decided based on the variance explained from the original dataset. The low-dimensional PC scores of the microstructures have been successfully utilized in building searchable microstructure databases [20] as well as in the construction of robust and reliable reduced-order S-P linkages [22, 24].

The introduction of PC representations of the n-point statistics in the series expressions developed in statistical continuum theories for effective properties produces a surprisingly simple expression [24, 25], i.e.,

$$P_{\text{eff}} \approx A_0 + \sum_{i=1}^{\tilde{R}} A_i \alpha_i \tag{3.6}$$

where A_i capture the underlying physics of the problem, P_{eff} is the effective property of interest, and $\tilde{R}$ is the truncation level selected for the PC representations. Indeed, Equation (3.6) expresses a linear relationship between P_{eff} and the scores of a chosen

set of PC basis vectors (which themselves are extremely rich sets of microstructural features). Although the above equation is easily derived for elastic response of composite material systems, it can be extended to nonlinear effective properties with suitable modifications [15, 22, 24, 25, 55–57]. In the MKS framework, the A_i coefficients are established through regression using datasets generated by numerical simulation tools (e.g., finite element models) on selected microstructure exemplars.

3.4 Extensions to the Theoretical Framework

Local states for the general class of polycrystalline metals may include descriptors such as crystal symmetry, dislocation density, and chemical composition (among others). However, for single-phase annealed polycrystals, the main local state of interest at the grain-scale is the crystal lattice orientation, g. The corresponding local state space is simply the orientation space. Based on the concepts discussed thus far, a simple approach to address polycrystalline microstructures is to bin the fundamental zone of orientation space [36]. As a specific example, the fundamental zone of orientation space for hexagonal crystals is expressed as

$$FZ_h = \{g = (\phi_1, \Phi, \phi_2) \mid 0 \leq \phi_1 < 2\pi,\ 0 \leq \Phi \leq \pi/2,\ 0 \leq \phi_2 \leq \pi/3\} \tag{3.7}$$

The main impediment to primitive binning of the orientation space (as implied in Equation (3.1)) comes essentially from the fact that a very large number of bins are needed to capture the orientation information accurately in the microstructure function and the 2-point spatial correlations. As an example, if one were to use one degree bins for each of the three Bunge-Euler angles involved in the definition of the orientations (cf. Equation(3.7)), one would end up with 1,944,000 local state bins. This large number of bins makes the computation, storage, and utilization of the 2-point spatial correlations highly unwieldy.

As an alternative, we explore here the utilization of generalized spherical harmonics [41, 52, 128, 129] as an efficient Fourier basis for the computation of the 2-point spatial correlations in polycrystalline microstructures. In this approach, we retain the primitive binning for the spatial variables and only change the basis for the orientation variables. With these changes, the microstructure function can now be expressed as

$$\begin{aligned} m(g,\boldsymbol{x})dg &\approx \sum_{l,m,\nu}\sum_{\boldsymbol{s}=\boldsymbol{1}}^{\boldsymbol{S}} M_{l\boldsymbol{s}}^{m\nu} T_l^{m\nu}(g)\chi_{\boldsymbol{s}}(\boldsymbol{x})dg \\ M_{l\boldsymbol{s}}^{m\nu} &= \frac{2l+1}{|\Delta\boldsymbol{x}|}\int_{FZ_h}\int_{\Omega_{\boldsymbol{x}}} m(g,\boldsymbol{x})T_l^{m\nu *}(g)\chi_{\boldsymbol{s}}(\boldsymbol{x})d\boldsymbol{x}dg \end{aligned} \tag{3.8}$$

where $T_l^{m\nu}(g)$ denote symmetrized GSH functions (in the present work, the symmetry of interest is the hexagonal-triclinic symmetry, where the first symmetry refers to crystal symmetry and the second one to the sample symmetry), * denotes a complex conjugate, $|\Delta\boldsymbol{x}|$ is the uniform size (volume) of a spatial bin, and $M_{l\boldsymbol{s}}^{m\nu}$ are the GSH Fourier coefficients. As a special case, when there is a single crystal of lattice orientation g_0 in a spatial bin $\boldsymbol{s}$, the corresponding GSH Fourier coefficients are simply given by

$$M_{l\boldsymbol{s}}^{m\nu} = (2l+1)T_l^{m\nu *}(g_0) \tag{3.9}$$

For simplicity of notation, we will map every distinct combination of (l,m,ν) to a single index L in all of the ensuing equations. As a result of this simplification, $M_{l\boldsymbol{s}}^{m\nu}$ will be henceforth denoted simply as $M_{\boldsymbol{s}}^{L}$. Extending the concept above, the description of the 2-point spatial correlations of orientations in the polycrystalline microstructure is expressed as

$$f(g,g'|\boldsymbol{r})dgdg' \approx \sum_{K}\sum_{L}\sum_{\boldsymbol{t}} F_{\boldsymbol{t}}^{LK} T_L(g)T_K(g')\chi_{\boldsymbol{t}}(\boldsymbol{r})dgdg' \tag{3.10}$$

However, if one were to start with the formal definition of the 2-point spatial corre-

lation (Equation (3.2)) and substitute the GSH representations of the microstructure function from Equation (3.8), we can derive the following relationship between the GSH Fourier coefficients in Eqs. (3.8) and (3.10):

$$F_{\boldsymbol{t}}^{LK} = \frac{1}{|\boldsymbol{S_t}|} \sum_{\boldsymbol{s=1}}^{\boldsymbol{S_t}} M_{\boldsymbol{s}}^{L} M_{\boldsymbol{s+t}}^{K} \tag{3.11}$$

The implicit convolution in Equation (3.11) (same as in Equation (3.4)) allows the exploitation of the FFT algorithms in computing the 2-point spatial correlations [20, 37, 125, 126].

As mentioned earlier, the set of 2-point statistics computed using Equation (3.11) will be large and unwieldy. As before, we will seek a lower dimensional representation of this set using PCA. In this case, however, the Fourier coefficients computed using Equation (3.11) are complex. One can either perform the PCA directly on these complex representations, or reshape them into separate real and imaginary components prior to performing the PCA. Both of these approaches would be completely equivalent, especially given that half of the $F_{\boldsymbol{t}}^{LK}$ coefficients are complex conjugates of the other half in our application. In order to construct the S-P linkage, we would continue to use the model form shown earlier in Equation (3.6) and calibrate the physically-based coefficients A_i with numerical simulation results obtained from finite element models for a selected number of microstructure exemplars.

3.5 Case Study

The purpose of this case study is to demonstrate the viability and potential of the data-driven protocols developed in the previous sections for the creation of S-P linkages. In these approaches, the physics capturing coefficients of Equation (3.6) will be determined through the following steps: (i) An ensemble of microstructure exemplars will be generated which exhibit a rich and diverse set of topological features

(these might include grain size, shape, and orientation distributions) covering a range of microstructures of interest for the intended application of the S-P linkages being produced. (ii) Crystal plasticity finite element (CPFE) simulations are performed on each microstructure exemplar in the ensemble to extract the effective (bulk) properties of interest. (iii) Each microstructure exemplar is quantified using 2-point spatial statistics with GSH basis functions. (iv) PCA is performed on the 2-pt statistics representations of the microstructure exemplars in the ensemble to produce a low-dimensional representation of each exemplar microstructure in the form of their PC scores. (v) Multivariate linear regression is performed on the assembled dataset (from steps (i)-(iv)) to calibrate the physics capturing coefficients of Equation (3.6). This calibrated model may then be validated by comparing the CPFE computed properties for new microstructure exemplars against the predictions of the reduced-order model. Each of the steps described above will be detailed in the following sections.

3.5.1 Generation of Microstructure Ensemble

In this work synthetic microstructure volume elements (MVEs) are generated both for establishing the S-P linkages of interest and for validating them. The MVEs must be sufficiently large to capture the rich microscale interactions between grains of different sizes, shapes, and orientations. In prior work, it was shown that these microscale interactions are most efficiently captured through influence kernels [13, 14, 16, 17, 21, 23, 26, 74]. More specifically, the decay in these Green's function-based influence kernels provides guidance for the minimum size of the MVEs. It is generally noted that the size of the MVEs should be larger for material systems with higher contrast in the local properties of the microscale constituents. Based on our prior experience [21, 23, 74], we employ MVEs of size 21x21x21 voxels in this work, where each voxel has a side length of $10\mu m$.

The MVEs used in this work are generated using the open-source DREAM.3D

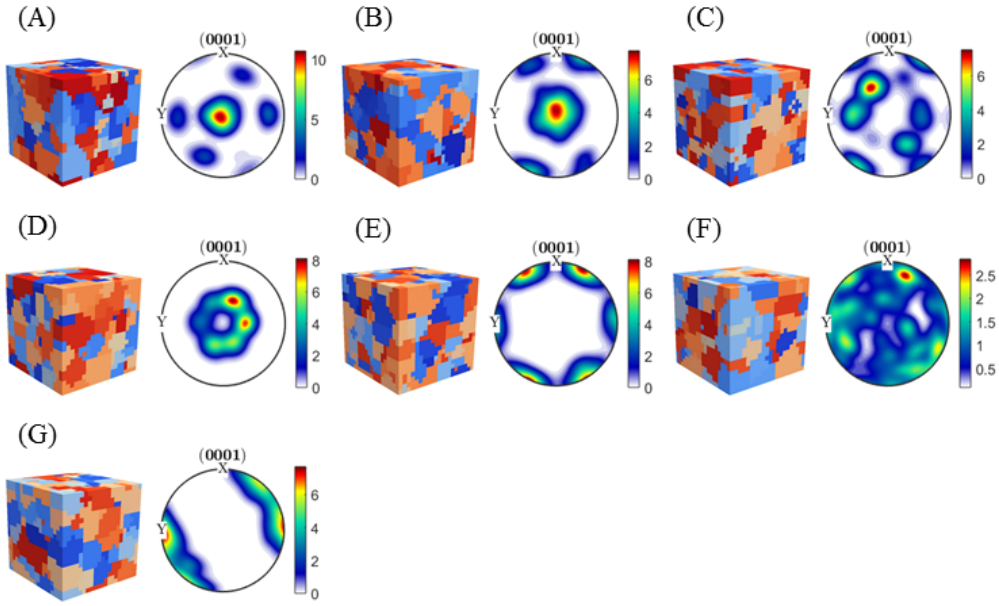

Figure 3.1: Sample MVEs (displayed using Grain ID maps) and (0002) pole figures for the generated microstructures classes A through G.

package [46], which accepts as inputs microstructure measures such as grain size, grain shape, orientation and misorientation distributions. In this first study on polycrystalline microstructures, we will focus our attention on the distribution of grain orientations (this is the main reason for using the GSH representations described earlier). Consequently, we restrict our attention to MVEs with different textures, but exhibiting a common grain size distribution. In part, this choice is also made due to lack of a significant collection of experimental characterizations of polycrystalline titanium materials accessible to us. In future work, it would be desirable to expand the range of the generated MVEs using more sophisticated approaches [130].

The targeted grain size distribution for the synthetically generated MVEs follows a log-normal distribution with an average grain size of $30\mu m$ and a $15\mu m$ standard deviation. Each MVE is comprised of an average of 215 distinct grains. Seven unique textures are selected as targets for the synthetic microstructure generation. These textures are inspired by those seen in our prior work as well as in literature [131, 132]. The target textures are entered into DREAM.3D as lists of orientations expressed as

triplets of Euler angles with associated weights and spreads. DREAM.3D is then utilized to randomly generate thirty polycrystalline MVEs for each microstructure class through an ellipsoidal packing algorithm. Then, DREAM.3D matches the target texture information for each microstructure class. Figure 3.1 shows example MVEs and (0002) pole figures for each microstructure class (corresponding to each selected texture). This figure only enables a qualitative comparison of microstructures. However, in later sections, the 2-pt spatial correlations and PCA will be used to quantify and visualize the differences between these microstructures.

3.5.2 CPFE Simulations

In this work, CPFE simulations are used to extract the homogenized properties for each MVE. The combination of each MVE and its associated properties constitutes one data point for the desired S-P linkages. The crystal plasticity framework used here was developed in prior work for α-phase grains in Ti6-4 [6, 47–51, 74, 75]. The model parameters relevant to the predictions of the effective (bulk) elastic stiffness and yield strength are summarized in Table 3.1. These include the five independent components of the transversely isotropic elastic stiffness tensor and the critical resolved shear strengths (CRSS) of relevant slip families. These elastic and inelastic parameters were obtained in prior work through fitting to experimental results on Ti6-4 [6, 49, 133]. As mentioned in the introduction, the S-P linkages resulting from this work learn the physics of the model used to generate the calibration data. So long as the results of the S-P linkage and CPFE simulations match, the goals of this work are achieved. Therefore, beyond the calibration of the crystal plasticity model, no further attempt is made to experimentally validate the simulated properties; these homogenized properties are taken as ground truth in the remainder of this work.

Periodic boundary conditions are applied to all surfaces of the three-dimensional MVEs to simulate the loading conditions needed to extract the effective properties

Table 3.1: Model parameters used in CPFE simulations.

Parameter	Value	Parameter	Value
c_{11}	172.8 GPa	τ_{CRSS}^{basal}	350 MPa
c_{12}	97.91 GPa	τ_{CRSS}^{prism}	275 MPa
c_{13}	73.43 GPa	$\tau_{CRSS}^{pyr\langle a\rangle}$	470 MPa
c_{33}	192.3 GPa	$\tau_{CRSS}^{pyr\langle a+c\rangle}$	570 MPa
c_{44}	49.70 GPa		

of interest for this study [134]. Displacement-controlled loading is imposed on the X-faces of the cuboidal MVEs, with zero net traction lateral faces to mimic the uniaxial stress state commonly observed in uniaxial tensile tests [48]. The loading is performed to 1.5% strain, a sufficient level to capture the elastic-plastic transition at the macroscale. The ABAQUS [77] mesh used in this work contains 9,261 C3D8R elements (one per voxel in each MVE); these element types have been used in previous work [6, 66, 68] with good agreement as compared to C3D8 elements for the determination of bulk properties. The simulations produce engineering stress-strain curves; the elastic stiffness of each digital microstructure is measured from the initial elastic portion of the engineering stress-strain curve and the yield strength is determined using a 0.2% offset with the calculated elastic stiffness.

3.5.3 Computation of 2-point Spatial Correlations

Equation (3.10) allows for the computationally efficient calculation of the 2-point spatial correlations in polycrystalline microstructures through the use of GSH representations for the functional dependencies on the orientation space. This is mainly because the number of GSH coefficients (determined by the truncation level used on L) required is expected to be far smaller than the number of discrete orientation bins needed to attain comparable accuracy in the desired S-P linkages. In prior work (cf. [21, 23]), this economy in the representation of S-P linkages was largely attributed to the fact that the physics-capturing kernels and coefficients (based on Green's func-

tions) operating on the microstructure descriptors (e.g., n-point spatial correlations) could be captured in a small number of terms in GSH-based expansions. We anticipate similar economy in the present application. For example, it can be shown theoretically that only $l = (0, 2, 4)$ terms in the GSH expansions should appear in homogenization linkages for effective elastic properties [19, 52, 78, 79]. However, we do not know a priori the acceptable truncation level on L for capturing the S-P linkages for the effective inelastic properties. Therefore, we treat the truncation level in the GSH coefficients as a hyper-parameter in the establishment of the S-P linkages (we will return to this parameter subsequently). It should be noted that the truncation on L should be carried out such a way that the complete set of terms corresponding to any selected value of l are included as a group. In other words, if one truncates at $l = 4$, then it is important to include all GSH terms corresponding to all combinations of μ and ν for $l \leq 4$ [19, 25]. For the hexagonal-triclinic GSH basis employed in this work, adoption of this consideration results in acceptable truncation levels of L at values of 6, 15, 41, and 90 (these correspond to l values truncated at 2, 4, 6 and 8, respectively).

Once a truncation level has been selected for L, the Fourier coefficients of the 2-point statistics may be computed using Equation (3.11). Let us denote this truncation value as $\tilde{L}$. In employing Equation (3.11) one can take advantage of a few strategies known to dramatically reduce the computational cost involved. First, the number of 2-point spatial correlations is $\tilde{L}^2$ (this includes all possible pairings of indices L and K in Equation (3.11)). In prior work on the multiphase microstructures [126], analytic relationships were derived between the spatial correlations. Appendix A presents these interrelationships for the 2-point statistics computed here on polycrystalline microstructures, where it is shown that the number of independent correlations is $2\tilde{L}-1$. It is important to recognize that these dependencies are not all linear. Furthermore, since PCA automatically removes the linearly dependent correlations, we do not need

to worry about the linearly dependent correlations. By repeated trials, the optimal set of spatial correlations to represent each MVE was selected (further details are provided in Appendix A). It was determined through these trials that the specific set of $2\tilde{L} - 1$ correlations identified in Appendix A produces the best compromise between accuracy and computational cost for the S-P linkages produced in this work.

3.5.4 Reduced Dimensional Microstructure Representation

Once spatial statistics are computed for all MVEs in the selected ensemble, PCA is performed to obtain reduced dimensional representations of the microstructure statistics. In this study, there are far more features (coefficients in the Fourier representation of the spatial statistics) than samples (MVEs). Therefore, the maximum number of PC scores that can be computed is 209 (one less than the number of MVEs used to build the PC space; see Equation (3.5)) [15]. However, a much smaller number of PCs are required to satisfactorily represent the spatial statistics for this case study. Figure 3.2 shows the cumulative variance captured by the inclusion of additional PCs. As $\tilde{R}$ increases, the cumulative explained variance (representing the 2-point statistics information) asymptotically approaches 100%. In addition, as the number of GSH basis functions used in the Fourier representation of the 2-point statistics increases (improving the fidelity of the microstructure representation), so does the $\tilde{R}$ required to achieve a given explained variance.

PCA also serves as an effective method to cluster MVEs and to evaluate the distances between them [15, 18, 20, 22, 24]. It is important to note that PCA results in unsupervised classification as the MVEs are not identified or labeled in any manner. Figure 3.3a demonstrates this natural clustering of the MVEs in the first two PC dimensions (the dimensions with the largest and the second-largest variances) for GSH spatial statistics at a truncation level of $\tilde{L} = 15$. Remarkably, even in just two dimensions, the MVEs distinctively cluster by their associated microstructure class

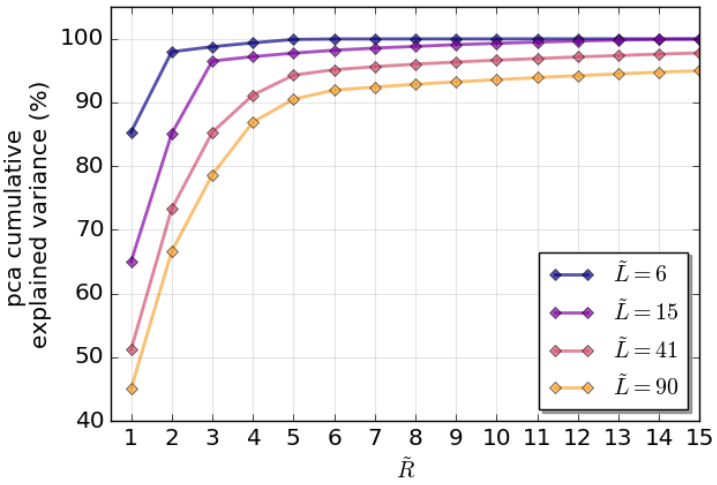

Figure 3.2: Percentage PCA explained structural variance versus $\tilde{R}$ and $\tilde{L}$

(here differentiated exclusively by target texture). In other words, even though the PCA is not informed explicitly about the textures in the MVEs, the first two PC scores effectively cluster the MVEs based on their differences in texture (note that the texture information is included in the 2-point statistics). Furthermore, it is seen that the intraclass variance in each cluster is not the same. For example, the MVEs belonging to class A exhibit more differences among themselves compared to the MVEs of class G in the first two PCs. This is, of course, a consequence of how each MVE is randomly generated for target microstructure statistics in the DREAM.3D software. Comparing Figure 3.1 and Figure 3.3a, it is also seen that microstructures with similar textures are nearby in the PC space, while microstructures with dramatically different textures are well separated. Notice that microstructure classes with strong basal texture components are located towards the left of Figure 3.3a, while microstructure classes with strong transverse texture components are located towards the right of this figure. Although such observations provide intuition into the meanings of the different PCs, it should be noted that the complete information captured by each PC is actually stored in the vectors, φ_{it}, obtained in PCA (see Equation (3.5)). Given the large size of these vectors (for a truncation level of $\tilde{L} = 15$ each PC

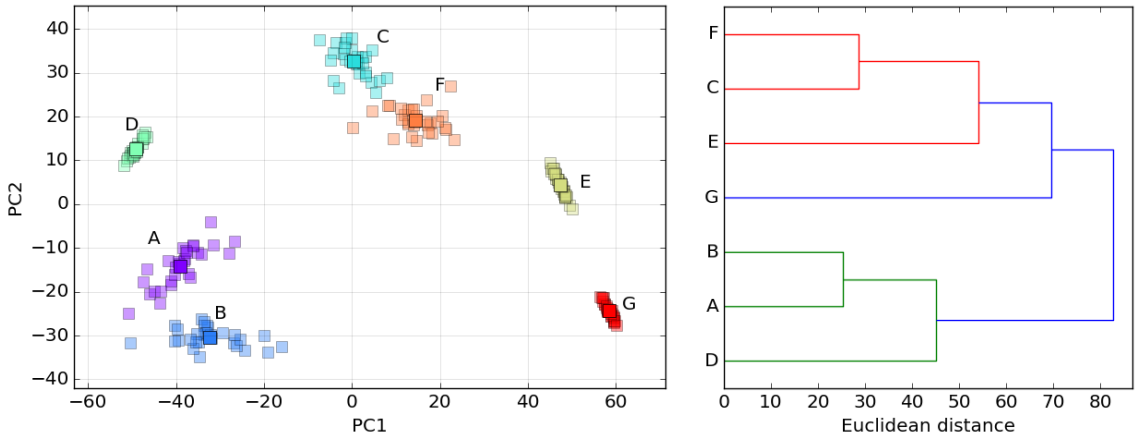

(a) (b)

Figure 3.3: Visualizations of microstructures enabled by PCA (for $\tilde{L} = 15$). (a) Clustering of MVEs by microstructure type in the first two PCs (b) Dendrogram showing the distances between microstructures and clusters of microstructures in PC space

has a length of 268,569 in the present study), it is not straightforward to establish their precise physical meaning.

Figure 3.3b shows the relative distances between the centers of the microstructure clusters in PC space, presented by way of a dendrogram. The advantage of this representation is that the displayed distances are computed over all available dimensions (in the present work this is 209). From the dendrogram, it can be seen that the first two PC dimensions adequately capture the relative distances between the microstructure classes. This is indeed the power of PC representations; they provide high value low dimensional representations of practical worth in quantifying the microstructure statistics. As such, this is an important component in the effort to extract robust and reliable S-P linkages.

3.5.5 Extraction of Structure-Property Linkages

The low dimensional representation of each MVE and its associated properties established using the CPFE model described earlier constitute the calibration dataset

for extracting the desired S-P linkages. More specifically, we intend to calibrate the physics-capturing coefficients of Equation (3.6) using a simple multivariate linear regression. Prior to calibration, two critical hyper-parameters, $\tilde{L}$ and $\tilde{R}$ must be selected. These hyper-parameters cannot be arbitrarily chosen; they must be selected individually for each property of interest by systematically exploring a large number of potential values (for both parameters) and evaluating their efficacy in producing the most reliable S-P linkages.

In order to accomplish this step, it is necessary to select the metrics by which we objectively evaluate each potential S-P linkage produced in this work. One obvious metric, called the calibration error, is simply defined as the mean of the absolute error between the MKS predicted and the CPFEM simulated values of the property for all MVEs, normalized by the mean value of the simulated property. Figure 3.4 shows the calibration error for $\tilde{R}$ up to 60 and four different $\tilde{L}$ levels for elastic stiffness (Figure 3.4a) and yield strength (Figure 3.4b). It is clear from these plots that the gains in accuracy quickly diminish with increasing values of both $\tilde{R}$ and $\tilde{L}$. This observation attests to the power of the PC and GSH representations employed in this work. Note also that the average error values are remarkably low - only about 0.2% for the elastic stiffness prediction and about 1.5% for the yield strength prediction. The fact that the prediction error for the yield strength is higher than that for the elastic stiffness is quite reasonable and expected. Indeed, prior work has shown that the elastic response of polycrystalline microstructures can be represented accurately by a limited set of GSH basis functions [21, 43]. In the present work, we observe no significant improvement in the accuracy of the elastic S-P linkage beyond $\tilde{L} = 15$ (corresponding to $l \leq 4$). For the predictions of the yield strength, higher values of $\tilde{L}$ did provide a modest improvement in the accuracy. These observations of the efficacy of the GSH representations are highly consistent with prior related work [21, 41, 43]. Considering the effect of the value of $\tilde{R}$, the most dramatic decrease in error

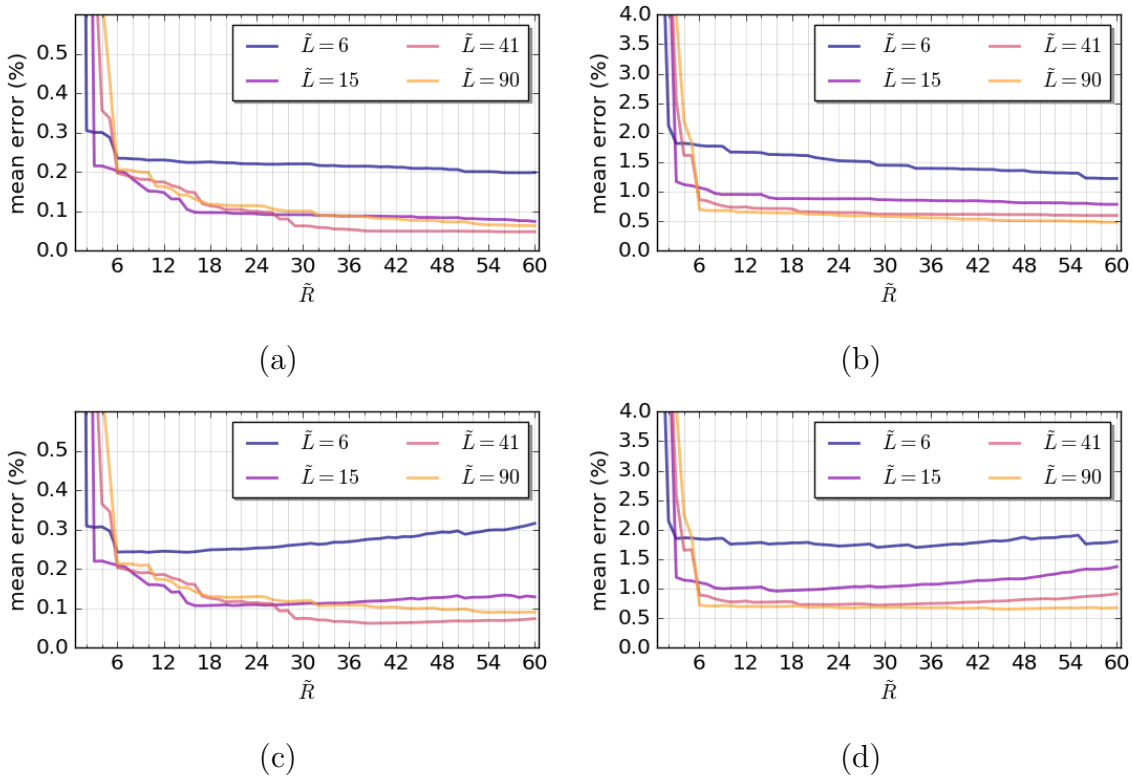

Figure 3.4: Error in the property prediction versus number of PCs included in the S-P linkage for different selections of the number of GSH basis functions. (a) Error in the prediction of elastic stiffness for MVEs in calibration set. (b) Error in prediction of yield strength for MVEs in calibration set. (c) LOOCV error in prediction of elastic stiffness for MVEs in calibration set. (d) LOOCV error in prediction of yield strength for MVEs in calibration set.

occurs within the inclusion of the first 10 PCs. This is consistent with the observation in Figure 3.2 that the explained structural variance quickly approaches 100% with increasing numbers of PCs.

Figures 3.4a and 3.4b illustrate the potential for overfitting the S-P linkages. The calibration error is usually not a good indicator for overfitting as it always decreases for increasing values of hyper-parameters such as $\tilde{R}$. In prior work, the Leave-One-Out Cross Validation (LOOCV) error metric was employed as an indicator of overfitting [22, 24]. In this approach, the S-P linkage is calibrated using the data for all MVEs in the ensemble except for one, and the error in the prediction of the property for the excluded MVE is recorded. The entire procedure is repeated for each MVE in the

ensemble. The LOOCV error is computed as the mean of the prediction errors for each excluded MVE in the ensemble and normalized the same way as the calibration error. The normalized LOOCV error is plotted for elastic stiffness and yield strength linkages in Figure 3.4c and Figure 3.4d, respectively. For both properties, the LOOCV error drops quickly for small values of $\tilde{R}$. The LOOCV error, however, begins to increase at higher values of $\tilde{R}$ indicating overfitting. It is also observed that the minimum LOOCV error occurs at a higher value of $\tilde{R}$ for the higher GSH truncation levels. This is once again consistent with the observation in Figure 3.2 that a higher $\tilde{R}$ is required to achieve the same explained variance for at higher values of $\tilde{L}$.

The optimal selection of $\tilde{L}$ and $\tilde{R}$ depends on the desired characteristics of the S-P linkages to be produced. If the minimization of error is paramount, the linkage with the lowest LOOCV error should be chosen. Such a linkage is expected to perform the best for new MVEs. However, if compactness is desired, then the linkage which has the minimum $\tilde{L}$ and $\tilde{R}$ yet has a LOOCV error below some acceptable threshold should be selected. In this study, reduced-order (low-dimensional) linkages are prioritized to demonstrate their applicability for inverse materials design problems. Through the consideration of Figure 3.4c a linkage for elastic stiffness is selected with 3 PCs and 15 GSH basis functions. From Figure 3.4d a linkage for yield strength is selected with 6 PCs and 41 GSH basis functions. This means that the S-P linkages produced in this study for elastic stiffness and yield strength only have 4 and 7 coefficients, respectively, in Equation 3.6.

3.5.6 Validation of Structure-Property Linkages

In the previous sections, a novel data science framework is developed and implemented for the extraction of highly accurate and robust S-P linkages (note the very low error values in Figure 3.4). We now seek to further validate these linkages using completely new MVEs (those that have not been used in the calibration). For this purpose, a

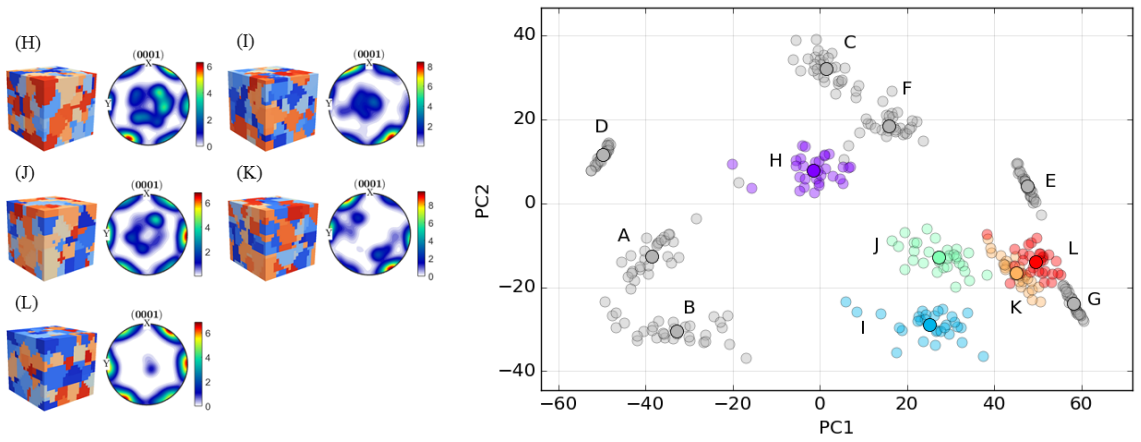

(a) (b)

Figure 3.5: (a) Sample MVEs (with Grain ID displayed) and (0002) pole figures for microstructure classes H through L. (b) The ensemble of validation MVEs in PC1 and PC2 (for $\tilde{L} = 15$). MVEs from previously existing microstructure classes are colored gray.

new set of MVEs are generated and their properties are simulated using the same protocols described earlier in this paper. However, in an effort to make these MVEs different from the calibration MVEs, five additional target textures are employed. Example MVEs and (0002) pole figures for each of the new microstructure classes are presented in Figure 3.5a. Microstructure class H is inspired from literature [132], while classes I through L are created using different combinations of texture components present in classes A through H. The new microstructure classes are intended to be interpolations between existing classes. The S-P linkages may give good results for small extrapolations beyond the bounds of the calibration MVE ensemble, but cannot be expected to predict the properties of completely new microstructures. As before, thirty MVEs are generated for each of the five new microstructure classes. Furthermore, thirty additional MVEs are generated for each of the existing microstructure classes. CPFEM simulations are performed for all MVEs in the validation ensemble to extract their yield strength and elastic stiffness.

For each MVE in the validation ensemble, the 2-point spatial correlations are

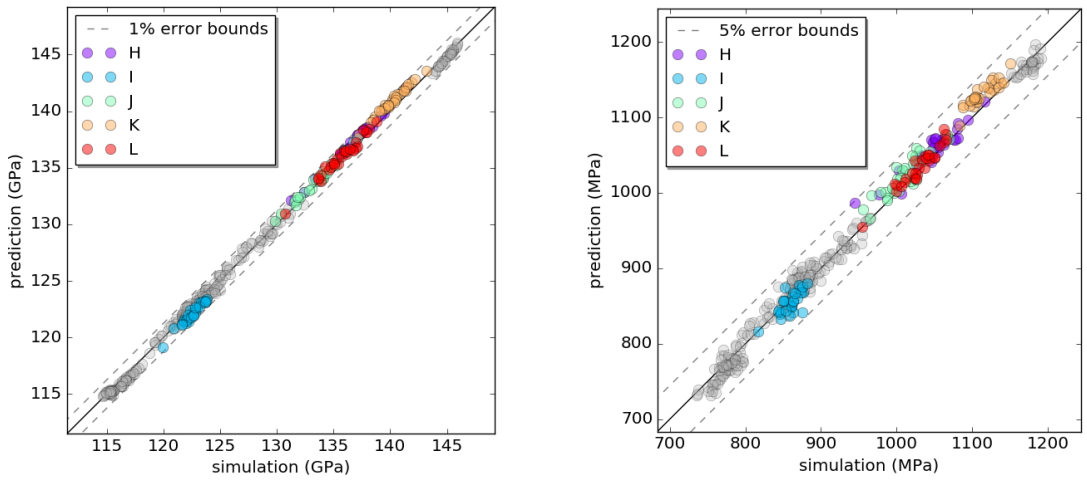

(a) (b)

Figure 3.6: Predicted versus simulated response for (a) elastic stiffness with 3 PCs and (b) yield strength with 6 PCs. Grey markers are for validation MVEs generated with target microstructure statistics from the original seven microstructure classes.

computed up to the GSH truncation levels selected for each property in Section 3.5.5. The spatial statistics for each new MVE are then transformed into the reduced dimensionality PC space already established in Section 3.3. This validation ensemble is displayed in Figure 3.5b in the PC1-PC2 space. For better visualization, the MVEs from microstructure classes H through L are highlighted in color in this figure, while MVEs from the original microstructure classes are shown in gray. The properties of each MVE in the validation ensemble are then predicted using the calibrated S-P linkages obtained in Section 3.5.5. Figure 3.6 presents parity plots for each S-P linkage, where the predicted property is plotted versus the simulated property (via CPFE simulations) for each MVE in the validation ensemble. The maximum prediction errors for elastic stiffness and yield strength in the calibration and validation ensembles are highly consistent with each other, and are below 1% and 5%, respectively. The success of both linkages in accurately predicting properties for these new microstructure classes demonstrates the robustness of the S-P linkage produced in this work.

3.6 Conclusions

In this work, novel data science protocols for the construction of reduced-order structure-property linkages in polycrystalline materials were developed and validated for the low crystal symmetry α-titanium materials system. This is the first use of GSH basis functions in the MKS framework for the computation of spatial statistics and for the construction of homogenization linkages. Protocols to predict both elastic stiffness and yield strength were developed, each in the form of polynomial equations with a small number of coefficients; it was demonstrated that only four and seven coefficients were required to predict elastic stiffness and yield strength respectively. These linkages provided massive computational savings versus traditional protocols. CPFE simulations for the prediction of yield strength in a single MVE took two hours on four processors on a super-computing cluster, while the reduced-order S-P linkage required only three seconds with one processor. This represents nearly four orders of magnitude reduction in processing time. The simplicity and efficiency of these robust structure-property linkages are well suited for inverse design protocols and will be instrumental in future materials design efforts.

Acknowledgments

This work was supported by the National Science Foundation under Grant No. CMMI-1333083. Any opinions, findings, and conclusions or recommendations expressed in this material are those of the authors and do not necessarily reflect the views of the National Science Foundation. NHP would like to thank Dipen Patel and David Brough for many illuminating conversations throughout the development of this work.

3.7 Appendix

In previous work, Niezgoda et al. [126] identified redundancies in the full set of 2-point spatial statistics. Knowledge of these redundancies is crucial for identifying an efficient yet comprehensive set of spatial statistics for the representation of microstructure. Specifically, it was shown that the discrete Fourier transforms (DFTs) of the 2-point statistics, $\tilde{F}^{np}_{\boldsymbol{j}} = \mathcal{F}(F^{np}_{\boldsymbol{t}})$, exhibit the following interrelationships:

$$\tilde{F}^{np}_{\boldsymbol{j}}\tilde{F}^{pq}_{\boldsymbol{j}} = \tilde{F}^{pp}_{\boldsymbol{j}}\tilde{F}^{nq}_{\boldsymbol{j}}, \qquad \tilde{F}^{np}_{\boldsymbol{j}} = \tilde{F}^{pn*}_{\boldsymbol{j}}, \qquad \tilde{F}^{nq}_{\boldsymbol{j}} = \frac{\tilde{F}^{pn*}_{\boldsymbol{j}}\tilde{F}^{pq}_{\boldsymbol{j}}}{\tilde{F}^{pp}_{\boldsymbol{j}}} \tag{3.12}$$

where $*$ denotes the complex conjugate. It is convenient to visualize $\tilde{F}^{np}_{\boldsymbol{j}}$ in the array $\left[\tilde{F}^{np}_{\boldsymbol{j}}\right]_{N\times N}$, where N is the number of discrete local states (in conventional binning of the local state space using indicator functions). Equation (3.12) implies that if $\tilde{F}^{np}_{\boldsymbol{j}}$ is known for a row or column of the correlation array, then the remainder of the array may be calculated. Furthermore, due to the properties of the indicator basis in the representation of the local state, only $N-1$ of the correlations in a given row or column are independent. Therefore there are only $N-1$ independent correlations in the set of the 2 point spatial correlations for an N-phase microstructure.

When the GSH basis is selected to describe the functional dependence of the grain orientation in the microstructure function, $F^{KL}_{\boldsymbol{t}}$ (see Equation (3.11)) does not have a simple interpretation as a probability. As a result, the conclusions of Equation (3.12) need to be suitably modified. Recognizing that $T_1(g) = 1$ it can be shown that

$$\tilde{F}^{Q1}_{\boldsymbol{j}=\boldsymbol{0}} = \tilde{F}^{1Q}_{\boldsymbol{j}=\boldsymbol{0}} = C_Q, \qquad \tilde{F}^{11}_{\boldsymbol{j}=\boldsymbol{0}} = |\boldsymbol{S}|, \qquad \tilde{F}^{Q1}_{\boldsymbol{j}\neq\boldsymbol{0}} = \tilde{F}^{1Q}_{\boldsymbol{j}\neq\boldsymbol{0}} = 0 \tag{3.13}$$

where C_Q are related to the 1-point statistics of the microstructure for single-phase polycrystals and contain the same information as the ODF. At this point it is useful

to introduce two different arrays of GSH-based 2-pt correlations:

$$A = \left[\tilde{F}_{\boldsymbol{j}}^{LK}\right]_{\tilde{L}\times\tilde{L}}, \qquad B = \left[\tilde{F}_{\boldsymbol{j}}^{LK}\right]_{\tilde{L}-1\times\tilde{L}-1} \text{ with } L = 1 \text{ and } K = 1 \text{ excluded} \quad (3.14)$$

Equations (3.12) and (3.13) imply that the independent set of correlations consists of the first row or column of A in addition to any row or column of B (for $2\tilde{L}-1$ total correlations).

To select the optimal set of correlations for this study, the errors associated with the S-P linkages calibrated using different sets of correlations are compared. These test linkages are developed for both elastic stiffness and yield strength at a GSH truncation level of $\tilde{L} = 6$. The following list describes a selection of correlation sets and the quality of the resultant linkages.

1. All correlations in A ($\tilde{L}^2$ correlations): This results in the lowest error of all sets.

2. The lower triangular correlations of A ($\frac{1}{2}(\tilde{L}^2 + \tilde{L})$ correlations): The error response is similar to set 1.

3. The first columns of A and B and the diagonal elements of B ($3(\tilde{L}-1)$ correlations): This results in an error slightly higher than sets 1 and 2.

4. The first column and diagonal elements of A ($2\tilde{L}-1$ correlations): This results in an error response similar to set 3.

5. The first columns of A and B ($2\tilde{L}-1$ correlations): This results in an error response worse than sets 1 and 2 but slightly better than 3 and 4.

6. The first column of A ($\tilde{L}$ correlations): This results in higher errors than in the preceding sets. Furthermore, error does not decrease beyond the inclusion of the first several PCs. This indicates that the ODF information is important, but not sufficient for high-quality predictive capability.

7. The first column of B ($\tilde{L}-1$ correlations): This results in extremely high errors (the linkages had no predictive utility). It is hypothesized that the correlations in B do not contain any information from the ODF, which is of first-order importance.

As a result of this investigation the first columns of A and B are selected as a good compromise between computational efficiency and S-P linkage quality.

CHAPTER 4

MKS LOCALIZATION PROTOCOLS TO RANK-ORDER THE HIGH CYCLE FATIGUE RESISTANCE OF POLYCRYSTALLINE MICROSTRUCTURES

This work was being prepared for submission to a peer-reviewed journal as of April 20, 2017. The title of the paper is *Strategies for rapid parametric assessment of microstructure-sensitive fatigue for HCP polycrystals*. The order of authorship is as follows: Matthew W. Priddy, Noah H. Paulson, Surya R. Kalidindi and David L. McDowell.

4.1 Abstract

Traditionally, crystal plasticity finite element method (CPFEM) simulations have been used to capture the variability in the microstructure-scale response of polycrystalline metals. However, these types of simulations are computationally expensive and require significant resources. To explore the large space of microstructures (reflecting a variety of grain shape, size, and orientation distributions) within the practical constraints of computational resources, a more efficient strategy is required. The purpose of this work is to explore the viability of leveraging the recently established, high-throughput Materials Knowledge System (MKS) for fast evaluation of high cycle fatigue (HCF) performance of candidate microstructures. More specifically, we explore the feasibility of estimating the mesoscale strain fields in hexagonal

close packed (HCP) α-titanium polycrystals during HCF loading conditions using the computationally low-cost MKS approach, and subsequently estimating the slip system activities via decoupled numerical integration of the relevant crystal plasticity (CP) constitutive relations. The computed slip activities are then used to arrive at extreme value distributions (EVDs) of fatigue indicator parameters (FIPs). As critical validation of this reduced-cost computational strategy, it is shown that the FIP distributions in the HCF regime estimated using this novel strategy are in reasonable agreement with those computed directly using the conventional CPFEM approach. Additionally, the computational advantages of the MKS and decoupled numerical integration approach over the traditional, computationally-expensive, CPFEM approach are presented and discussed.

4.2 Introduction

Titanium and its alloys have attractive strength-to-weight ratios and corrosion resistance, both of which are vital for the aerospace, automotive, and biomedical industries. The α-phase of titanium has a hexagonal close packed (HCP) crystal structure while the β-phase has a body centered cubic (BCC) crystal structure. In general, titanium alloys can be categorized as α or near α, $\alpha + \beta$, or β alloys [135]. Titanium alloys exhibit an enormous diversity of microstructure arrangements resulting from the combined effect of composition and thermo-mechanical processing routes [136]. Furthermore, these microstructures are characterized by elastic and inelastic anisotropy at multiple length-scales [21, 73, 78, 101]. This variation in microstructure and resultant mechanical properties can lead to competing objectives in the material selection or optimization process.

Fatigue resistance is an important performance characteristic for titanium alloys because of their applications of use. Experimental evaluation of the fatigue resistance of materials is costly and labor intensive. In addition, the information extracted is

often limited to simple metrics such as the number of cycles to failure. Unfortunately, it can be difficult to relate this data to microstructure variables (e.g., grain size distribution and crystallographic texture) because this requires parametric arrays of experiments and material characterization. Computational frameworks such as the crystal plasticity finite element method (CPFEM) have been used recently for relating microstructure features to macroscopic material properties [98, 103, 105]. CPFEM allows for the estimation of local plastic deformation and the associated fatigue indicator parameters (FIPs); however, the practical viability of employing CPFEM for microstructure-sensitive design of polycrystalline microstructures for improved high cycle fatigue (HCF) performance is rather limited due to the high demands placed on computational resources.

To circumvent the difficulties mentioned above, an alternative approach is proposed in this work that leverages modern machine learning techniques to significantly reduce the computational cost of evaluating the HCF performance of polycrystalline materials. Specifically, this approach takes advantage of a convenient trait of the HCF regime; the magnitudes of the cyclic plastic strains are generally much lower than the magnitudes of the cyclic elastic strains. This feature enables the use of the recently developed Materials Knowledge System (MKS) to efficiently predict the elastic strain fields in the polycrystalline microstructures [13, 14, 17, 19, 21, 23]. Stresses may be directly calculated from the elastic strains using Hooke's Law and resolved onto each slip system. Plastic strains may then be estimated by numerically integrating a crystal plasticity flow rule over a specified number of cycles. As with traditional computational approaches, these plastic quantities enable the computation of FIPs and the rank-ordering of the HCF resistance of candidate microstructures. In this work, these novel protocols are demonstrated for the analysis of the HCF resistance of a diverse set of α-titanium microstructures subjected to uniaxial loading conditions.

4.3 Background

4.3.1 Crystal Plasticity Framework

The anisotropic deformation response of polycrystalline materials can be simulated using crystal plasticity [98, 137, 138] to successfully rank-order the HCF resistance of different α-titanium microstructures. Specifically, the crystal plasticity framework considered in this work was initially developed as a CPFEM model for 2D analysis of duplex Ti-6Al-4V [47], was extended to 3-D [48], and then further modified by various authors [6, 49–51, 134]. Most recently, Smith et al. [6] calibrated the model to three distinct titanium alloy microstructures via uniaxial tension and fully-reversed tension-compression experimental data (employing periodic boundary conditions for uniaxial stress in simulation). In the remainder of this section, the features of this crystal plasticity framework relevant to the present modeling of α-titanium are discussed in detail (features relevant to the modeling of α-β titanium colony grains are not discussed).

HCP crystal structures have the following slip systems: (i) basal slip $\{0001\}\langle 11\bar{2}0\rangle$, (ii) prismatic slip $\{10\bar{1}0\}\langle 11\bar{2}0\rangle$, (iii) $\langle \mathrm{a}\rangle$ pyramidal slip $\{10\bar{1}1\}\langle 11\bar{2}0\rangle$, (iv) first-order $\langle \mathrm{c}+\mathrm{a}\rangle$ pyramidal slip $\{10\bar{1}1\}\langle 11\bar{2}3\rangle$, and (v) second-order $\langle \mathrm{c}+\mathrm{a}\rangle$ pyramidal slip $\{11\bar{2}2\}\langle 11\bar{2}3\rangle$. These slip planes and their associated slip directions are shown in Figure 4.1.

In the α-phase of Ti-6Al-4V, prismatic slip has the smallest critical resolved shear stress (CRSS), followed by basal slip, while the pyramidal families exhibit much higher slip-resistance values. Deformation twinning can also be present in titanium alloys, but is severely diminished with an Al content above 6% in Ti-6Al-4V [139]. Accordingly, we will only consider slip and will neglect twinning in this study.

The crystal plasticity model employed in this work is based on the two-term multiplicative decomposition of the deformation gradient into elastic and plastic parts

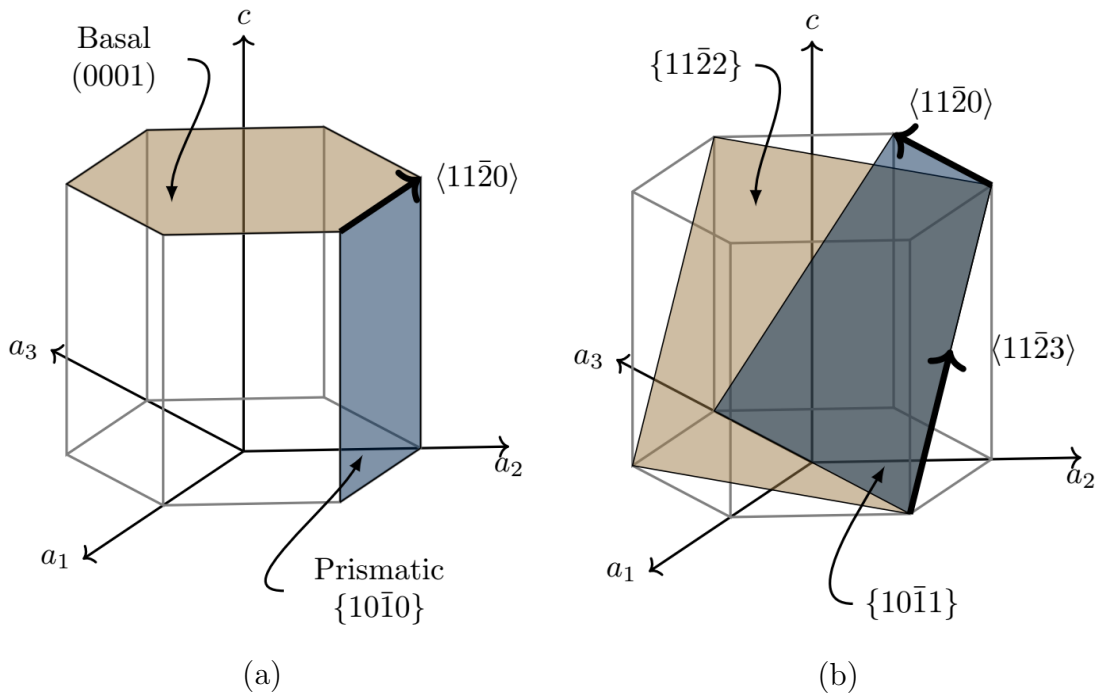

Figure 4.1: Schematic of (a) basal and prismatic slip planes and associated slip directions along with (b) ⟨a⟩ pyramidal and ⟨c + a⟩ pyramidal slip planes and associated slip directions.

(i.e. $\mathbf{F} = \mathbf{F}^{\mathrm{e}} \cdot \mathbf{F}^{\mathrm{p}}$). The plastic velocity gradient is determined in the intermediate configuration [137], which is both isoclinic and lattice invariant. The symmetric second Piola-Kirchhoff stress, $\boldsymbol{\sigma}^{PK2}$, is obtained by application of linear elasticity in the intermediate isoclinic configuration, i.e.,

$$\boldsymbol{\sigma}^{PK2} = \mathbb{C}_0 : \mathbf{E}^e \tag{4.1}$$

where $\mathbb{C}_0$ is the fourth-rank elasticity tensor in the intermediate configuration. The elastic Green strain is defined by

$$\mathbf{E}^e = \frac{1}{2}\left[(\mathbf{F}^e)^{\mathrm{T}} \cdot \mathbf{F}^e - \mathbf{I}\right]. \tag{4.2}$$

The Cauchy stress ($\boldsymbol{\sigma}$) can be found by mapping the second Piola-Kirchhoff stress to

the current configuration, i.e.,

$$\boldsymbol{\sigma} = \frac{1}{\det\left(\mathbf{F}^e\right)}\left[\mathbf{F}^e \cdot \boldsymbol{\sigma}^{PK2} \cdot \left(\mathbf{F}^e\right)^{\mathrm{T}}\right]. \tag{4.3}$$

Finally, the resolved shear stress on slip system (ξ) is given by

$$\tau^{(\xi)} = \boldsymbol{\sigma}^{PK2} : \left(\mathbf{s}_0^{(\xi)} \otimes \mathbf{n}_0^{(\xi)}\right). \tag{4.4}$$

where $\mathbf{s}_0^{(\xi)}$ and $\mathbf{n}_0^{(\xi)}$ are the slip direction and slip plane normal, respectively, in the intermediate (and reference) configuration.

The isothermal slip system shearing rate, $\dot{\gamma}^{(\xi)}$ is defined according to a power-law flow rule of the form

$$\dot{\gamma}^{(\xi)} = \dot{\gamma}_0 \left\langle \frac{\left|\tau^{(\xi)} - \chi^{(\xi)}\right| - \kappa^{(\xi)}}{D^{(\xi)}} \right\rangle^M \operatorname{sgn}\left(\tau^{(\xi)} - \chi^{(\xi)}\right), \tag{4.5}$$

where $\dot{\gamma}_0$ is the reference shearing rate, $\chi^{(\xi)}$ is the back stress, $\kappa^{(\xi)}$ is the threshold stress, $D^{(\xi)}$ is the drag stress, and M is the inverse strain-rate sensitivity exponent. The threshold stress is defined as the sum of a Hall-Petch strength term and a softening term due to breakdown of short-range order, i.e.,

$$\kappa^{(\xi)} = \frac{\kappa_y}{\sqrt{d}} + \kappa_s^{(\xi)}. \tag{4.6}$$

In Equation (4.6), κ_y is the Hall-Petch slope, d is the mean slip distance in the α-phase, and $\kappa_s^{(\xi)}$ is a softening parameter. The evolution of the threshold stress is governed solely by the softening term, which follows a dynamic recovery law and takes the form

$$\dot{\kappa}^{(\xi)} = \dot{\kappa_s}^{(\xi)} = -\mu\kappa_s \left|\dot{\gamma}^{(\xi)}\right| \tag{4.7}$$

where μ is the softening rate coefficient. The drag stress is the difference between the

CRSS (τ_{CRSS}) and the initial threshold stress [140], i.e.

$$D^{(\xi)} = \tau^{(\xi)}_{CRSS} - \kappa^{(\xi)}\big|_{t=0}\,. \tag{4.8}$$

The drag stress does not evolve (i.e., $\dot{D}^{(\xi)} = 0$), while the back stress is initially set to zero and evolves according to a direct hardening/dynamic recovery relation of the form

$$\dot{\chi}^{(\xi)} = h\dot{\gamma}^{(\xi)} - h_D\chi^{(\xi)}\left|\dot{\gamma}^{(\xi)}\right|, \tag{4.9}$$

where h is the direct hardening coefficient and h_D is the dynamic recovery coefficient. The parameter values for the crystal plasticity framework described in this section are included below in Table 4.1 [6].

Table 4.1: Elastic and inelastic crystal plasticity model parameters for α-titanium.

Parameter	Value	Parameter	Value	Parameter	Value
c_{11}	172.8 GPa	τ^{basal}_{CRSS}	350 MPa	h	50 MPa
c_{12}	97.9 GPa	τ^{prism}_{CRSS}	275 MPa	h_D	50 MPa
c_{13}	73.4 GPa	$\tau^{pyr\langle a\rangle}_{CRSS}$	470 MPa	d	146 μm
c_{33}	192.3 GPa	$\tau^{pyr\langle a+c\rangle}_{CRSS}$	570 MPa	μ	2
c_{44}	49.7 GPa	κ_s	50 MPa		

4.3.2 Materials Knowledge System

In recent years, a computationally efficient localization framework for hierarchical material microstructure called the Materials Knowledge System (MKS) has been developed [13, 14, 17, 19, 21, 23, 26]. The MKS is an algebraic series capable of predicting response fields on the mesoscale given the corresponding macroscale averaged loading or boundary conditions. The details of the MKS framework relevant to its application in the present study are briefly described next.

The response of hierarchical materials systems has been addressed using generalized composite theories [31, 33, 40, 55, 56, 114, 115, 117], wherein a localization tensor

relates the material response at the mesoscale to the macroscale averaged values. In the case of linear-elastic response, the fourth-order localization tensor $\boldsymbol{A}(\boldsymbol{x})$ relates the elastic strain at a location in the microstructure, $\boldsymbol{x}$, to the average macroscopic strain imposed on the microstructure:

$$\boldsymbol{\epsilon}(\boldsymbol{x}) = \boldsymbol{A}(\boldsymbol{x}) : \langle \boldsymbol{\epsilon}(\boldsymbol{x}) \rangle \tag{4.10a}$$

$$\boldsymbol{A}(\boldsymbol{x}) = \boldsymbol{I} - \langle \boldsymbol{\Gamma}(\boldsymbol{x}, \boldsymbol{x}') : \boldsymbol{C}'(\boldsymbol{x}') \rangle + \langle \boldsymbol{\Gamma}(\boldsymbol{x}, \boldsymbol{x}') : \boldsymbol{C}'(\boldsymbol{x}') : \boldsymbol{\Gamma}(\boldsymbol{x}', \boldsymbol{x}'') : \boldsymbol{C}'(\boldsymbol{x}'') \rangle - \dots \tag{4.10b}$$

In Equation (4.10b), $\boldsymbol{I}$ is the fourth-rank identity tensor, $\boldsymbol{C}'(\boldsymbol{x})$ is the deviation in elastic stiffness from some arbitrary reference medium at a location $\boldsymbol{x}$, $\boldsymbol{\Gamma}$ is a symmetrized derivative of the Green's function defined with the elastic properties of the reference medium and $\langle f \rangle$ signifies the ensemble average of a variable f over all spatial locations in the microstructure.

Equation (4.10b) can be transformed to a more convenient form through the introduction of the microstructure function, $m(\boldsymbol{x}, h)$ [36], which captures the probability density of finding local state h at the spatial location $\boldsymbol{x}$. The local state descriptors are selected in such a manner that allows one to define the local mesoscale properties at the spatial location $\boldsymbol{x}$ (these may include phase identifiers, crystal orientation, etc.). Through the introduction of $m(\boldsymbol{x}, h)$, substitution of $\boldsymbol{r} = \boldsymbol{x} - \boldsymbol{x}'$ and invocation of the ergodic hypothesis, Equations (4.10a) and (4.10b) can be rewritten as

$$\boldsymbol{\epsilon}(\boldsymbol{x}) = \Big(\boldsymbol{I} - \int_{\boldsymbol{R}} \int_{H} \boldsymbol{a}(\boldsymbol{r}, h)\, m(\boldsymbol{x} + \boldsymbol{r}, h)\, dh d\boldsymbol{r} + \int_{\boldsymbol{R}} \int_{\boldsymbol{R}} \int_{H} \int_{H} \tilde{\boldsymbol{a}}(\boldsymbol{r}, \boldsymbol{r}', h, h')\, m(\boldsymbol{x} + \boldsymbol{r}, h)\, m(\boldsymbol{x} + \boldsymbol{r} + \boldsymbol{r}', h')\, dh dh' d\boldsymbol{r} d\boldsymbol{r}' - \dots \Big) : \langle \boldsymbol{\epsilon}(\boldsymbol{x}) \rangle \tag{4.11}$$

where $\boldsymbol{a}(\boldsymbol{r}, h)$ and $\tilde{\boldsymbol{a}}(\boldsymbol{r}, \boldsymbol{r}', h, h')$ are the first- and second-order influence functions [14], respectively, H is the set of all possible distinct local states ($h \in H$) and $\boldsymbol{R}$ is

the set of all vectors ($\boldsymbol{r} \in \boldsymbol{R}$). The first-order influence functions $\boldsymbol{a}(\boldsymbol{r}, h)$ quantify the contribution to the local response in the current spatial location due to the presence of local state h at a vector $\boldsymbol{r}$ away. Note that the influence functions are fourth-rank tensors and satisfy the mapping established in Equation (4.10). The influence functions are computationally advantageous as they are completely independent of microstructure. Equation (4.11) is an infinite series where each successive term captures the influence of the local topology for higher levels of interactions between the local states [23]. It is worth noting that when the variation of local properties (or contrast) throughout the range of H is low, the series can be truncated to the first-order terms with minimal loss of accuracy [13, 14, 21, 23].

Unfortunately, $\boldsymbol{\Gamma}(\boldsymbol{r})$ has a singularity as $\boldsymbol{r}$ approaches zero, and the convergence of the series is highly sensitive to the selection of the reference medium. The MKS avoids these computational issues through a calibration of the influence functions using results from numerical simulations (e.g., based on finite element simulations) that include a variety of microstructures and their local response fields. Once the influence functions are calibrated, the resulting linkages can be used to predict the response field of any new microstructure in the materials system at a far lower computational cost than using existing numerical frameworks.

Next, a generalized MKS framework is presented which extends Equation (4.11) to complex microstructures (e.g., polycrystalline microstructures studied in this work). First, $m(\boldsymbol{x}, h)$ and $\boldsymbol{a}(\boldsymbol{x}, h)$ are expressed as Fourier series using products of orthonormal basis over both the local state space and the spatial domain of the microstructure [21, 23]:

$$m(\boldsymbol{x}, h) = \sum_{L} \sum_{\boldsymbol{s}} M_{\boldsymbol{s}}^{L} Q_L(h) \chi_{\boldsymbol{s}}(\boldsymbol{x}), \tag{4.12}$$

$$\mathbf{a}(\boldsymbol{r}, h) = \sum_{L} \sum_{\boldsymbol{t}} \boldsymbol{A}_{\boldsymbol{t}}^{L} Q_L(h) \chi_{\boldsymbol{t}}(\boldsymbol{r}), \tag{4.13}$$

where $Q_L(h)$ and $\chi_{\boldsymbol{s}}(\boldsymbol{x})$ denote the basis indexed by L and s, respectively. $\chi_{\boldsymbol{s}}(\boldsymbol{x})$ are

referred as the indicator basis and return one for all values of $\boldsymbol{x}$ within the spatial bin indexed by $\boldsymbol{s}$, and zero elsewhere. This uniform discretization of the spatial domain allows for the application of the FFT algorithm in the evaluation of Equations (4.12) and (4.13). If the same indicator basis is chosen for $Q_L(h)$, the local state space will be binned discretely (e.g., a two phase composite material). If the desired local state space is crystal lattice orientation, this binning strategy proves computationally inefficient as the number of bins required to accurately represent the orientation space is very large (1,944,000 bins for 1° spacing in each of the three Bunge-Euler [41] angles, ϕ_1, Φ and ϕ_2, used to describe the lattice orientation in a hexagonal crystal). It is far more efficient in this case to use the generalized spherical harmonics (GSH) [41]; a continuous, periodic, and orthonormal basis for functions on the orientation space defined using the Bunge-Euler angles.

Through the utilization of the orthogonality of the bases, expressions for $M_{\boldsymbol{s}}^L$ and $\boldsymbol{A}_{\boldsymbol{t}}^L$ can be derived from Equation (4.12) and Equation (4.13) [23]. Introducing these definitions, the MKS can be expressed as

$$\begin{aligned}\boldsymbol{\epsilon}_{\boldsymbol{s}} = \Bigg(& \sum_{L} \sum_{\boldsymbol{t}} \frac{\Delta}{N_L} \boldsymbol{A}_{\boldsymbol{t}}^L M_{\boldsymbol{s}+\boldsymbol{t}}^L + \\ & \sum_{L} \sum_{L'} \sum_{\boldsymbol{t}} \sum_{\boldsymbol{t}'} \frac{\Delta^2}{N_L N_{L'}} \boldsymbol{A}_{\boldsymbol{t}}^{LL'} M_{\boldsymbol{s}+\boldsymbol{t}}^L M_{\boldsymbol{s}+\boldsymbol{t}+\boldsymbol{t}'}^{L'} + \ldots \Bigg) : \langle \boldsymbol{\epsilon} \rangle.\end{aligned} \tag{4.14}$$

where Δ is the volume of a spatial bin and N_L is a constant that may depend on L.

4.3.3 Fatigue Indicator Parameters

The driving force for growth of long cracks in metals is adequately described by the stress intensity factor in the context of LEFM [59]. In particular, a variety of stress-, strain-, and energy-based relations have been employed to predict fatigue crack growth at the macroscopic length scale [60]. The driving force for small fatigue crack formation and early growth, however, is strongly dependent on the local driving

force, which in turn is directly linked to the microstructure of the material and local cyclic slip conditions [141]. Fatigue indicator parameters (FIPs) have been used in macroscale and mesoscale data analysis to serve as surrogate measures of the driving force for fatigue crack nucleation and early growth [63, 142].

The HCF regime typically requires more than 100,000 cycles to failure and is characterized by heterogeneous plastic deformation among grains, with the majority of grains undergoing elastic deformation throughout the specimen. The majority of cycles to failure for HCF involve processes of crack nucleation and early growth through the first few grains. Additionally, the fatigue crack formation process is strongly affected by the spatial variation of microstructure features (e.g., grain size, orientation, disorientation) that give rise to heterogeneous stress and plastic strain states. These local elevated states of cyclic plastic shear strain can lead to localized damage and, ultimately, the formation of a single dominant crack that eventually propagates to failure [61]. For example, for Ti-6Al-4V tested at room temperature with R=0.1, more than 85% of the high-cycle fatigue life (strain amplitude not reported) was spent initiating and propagating small cracks up to 0.5 mm in length [143].

Distinct FIPs were introduced [58] to explicitly account for cyclic (reversed) slip per cycle as well as cumulative directional slip and have since been used in conjunction with macroscopic experimental [64, 144–148] and computational [149] data of titanium alloys. FIPs have also been combined with finite element simulations to make life estimates [65, 150] and compare the relative fatigue resistance of multiple microstructures or materials [67]. In these cases, the selection of a specific FIP is important to reflect the deformation mechanisms that contribute to fatigue crack formation and early growth. For example, the Fatemi-Socie [63, 151] shear-based FIP has been shown to correlate well in the LCF and HCF regimes for multiaxial fatigue

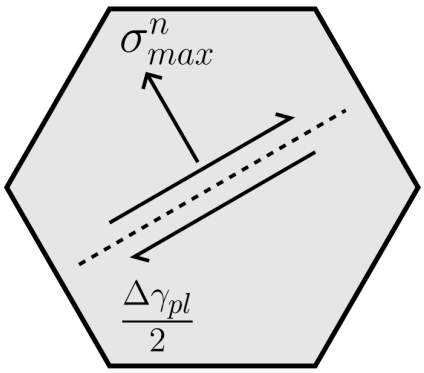

Figure 4.2: Illustration of the two parameters computed to assess the Fatemi-Socie Fatigue Indicator Parameter (FIP_{FS}).

crack initiation [62] and is defined by [67]

$$FIP_{FS} = \frac{\Delta\bar{\gamma}^p_{max}}{2}\left[1 + k\frac{\bar{\sigma}^n_{max}}{\sigma_y}\right], \tag{4.15}$$

where $\Delta\gamma^p_{max}$ is the maximum cyclic plastic shear strain range, σ^n_{max} is the maximum stress normal to the maximum cyclic plastic shear strain, σ_y is the macroscopic yield strength of the material and k is a constant with typical values between 0.5 and 1. The overbar ($\Delta\bar{\gamma}^p_{max}$, $\bar{\sigma}^n_{max}$) indicates that volumetric averaging should be performed [67]. The Fatemi-Socie FIP correlates well with fatigue crack formation and early growth for metals that exhibit planar slip [140]; a graphical representation is shown in Figure 4.2. Additionally, FIP values can be extended to assist in the calculation of life estimates [65, 150, 152]. The FIP_{FS} in Equation (4.15) serves as an effective grain-level surrogate measure for the cyclic crack tip displacement range of small crystallographic fatigue cracks [65].

4.3.4 Extreme Value Statistics

Microstructure locations with the lowest resistance to fatigue crack formation are associated with the largest FIP values identified through Equation (4.15). A single FIP value, however, is not sufficient to evaluate a microstructure's resistance to HCF.

Instead, the distribution of the most extreme FIP values for a sufficient volume of material gives some indication of the relative presence of HCF susceptible locations in the microstructure. In previous work [67, 69], a statistical approach was taken where multiple instantiations of each microstructure were simulated using CPFEM and the maximum FIP values in each were used to perform an EVD analysis. The FIP distributions were fit to a Gumbel distribution [153], i.e.,

$$F_{Y_n}(y_n) = \exp\left[-e^{\alpha_n(y_n - u_n)}\right], \tag{4.16}$$

where $F_{Y_n}(y_n)$ is the probability that Y_n will be equal to or less than y_n, u_n is the characteristic largest value of the sampled population, and α_n is an inverse measure of dispersion of the largest values of the population. The Gumbel distribution is unbounded and the shape of the probability density function is the same regardless of the fitting parameters. The maximum FIP values are arranged in increasing magnitude and their probability estimated by

$$F_{Y_j}(y_j) = \frac{j - 0.3}{n + 0.4}, \tag{4.17}$$

where n is the total number of simulations and j is the rank-order of each maximum FIP value. For plotting and regression purposes, the Gumbel distribution is reformulated as a linear function of y with expressions for slope (α_n) and y-intercept ($\alpha_n u_n$), i.e.,

$$\ln\left[\frac{1}{\ln\left[F_{Y_n}(y_n)\right]}\right] = \alpha_n y_n - \alpha_n u_n. \tag{4.18}$$

These resultant distributions are the basis for comparing fatigue resistance among different microstructures in this work.

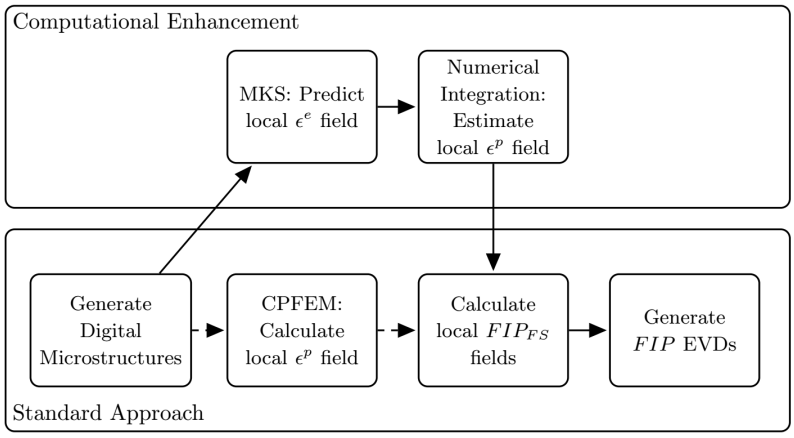

Figure 4.3: Flowchart for the insertion of MKS into the traditional workflow for producing extreme value distributions of the extreme FIP responses.

4.4 Proposed Methodology

The main purpose of this work is to explore a novel, computationally-efficient method for rank-ordering the HCF resistance of polycrystalline microstructures. The conventional approach, shown in the bottom row of Figure 4.3, adheres to the following steps: (i) digital microstructures are obtained, (ii) CPFEM is used to determine the local cyclic plastic strain tensors, (iii) FIP fields are computed for each microstructure, and (iv) extreme value distributions of FIPs are constructed to rank-order the microstructures in terms of their HCF resistance. The new approach explored in this study (also displayed in Figure 4.3) utilizes the MKS method to determine the local total strain fields and calculate the local plastic strain tensors through a decoupled integration scheme that employs the relevant constitutive relations described in Section 4.3.1. The remainder of this section describes this new approach in detail.

First, a diverse set of microstructures of interest are identified for a given composition as a function of thermo-mechanical process path. Traditionally, a representative volume element (RVE) is established to capture the microstructure for subsequent computational evaluations. RVEs are intended to approximate the response of the overall material microstructure by encompassing a volume that is large enough to con-

tain a sufficient number of microstructure-specific features for statistical homogeneity [154]. Additionally, RVEs must have measurable properties (e.g., elastic modulus, thermal conductivity) that are in agreement with the properties of an extremely large volume of the true material microstructure. Unfortunately, this typically requires performing simulations on prohibitively large volumes of material, especially to describe extreme value phenomena such as HCF. Instead, the microstructures may be represented by an ensemble of smaller statistical volume elements (SVEs), which are constructed such that their size is sufficient to sample microstructure-specific features (e.g., grains), but whose individual responses might differ from that of an RVE. In this framework, a large enough set of SVEs is selected for each microstructure to demonstrate the convergence of a representative property.

Next, if they have not been previously computed for the specific material system being studied, the MKS influence functions are calibrated with an ensemble of calibration SVEs and their responses as computed using linear-elastic FE simulations. These simulations are performed using appropriate periodic boundary conditions for the applied loading of interest and the elastic model parameters given in Table 4.1. The use of an MKS calibrated with linear-elastic simulations is justified as the cyclic plastic strains in the HCF regime are expected to be orders of magnitude smaller than the elastic strains; therefore the total strains are approximately equal to the elastic strains. Once the Fourier coefficients of the influence function (herein called influence coefficients) are calibrated for each set of boundary conditions and for all unique components of the strain tensor, Equation (4.14) is employed to efficiently predict the elastic strain fields in each SVE at the minimum and maximum applied strains in strain-controlled cyclic loading. The stress tensor is calculated from the strain tensor in each voxel for the local fourth-order elastic stiffness tensor (see Equation (4.1)). Assuming a linear relationship between the initial and final stress tensors, each loading segment is discretized into a number of increments. The stress tensor

is then used to determine the resolved shear stress in each slip system ($\tau^{(\xi)}$) for each time increment, according to

$$\tau^{(\xi)} = \boldsymbol{\sigma} : \left(\mathbf{s}^{(\xi)} \otimes \mathbf{n}^{(\xi)}\right), \tag{4.19}$$

where $\mathbf{s}^{(\xi)}$ and $\mathbf{n}^{(\xi)}$ are the slip direction and slip plane normal, respectively. The resolved shear stress is then used to solve for the slip system shearing rate (Equation (4.5)) and evolution equations (Equations (4.7) and (4.9)) in each time increment. A forward Euler routine, commonly used in explicit CPFEM simulations [155], is employed to obtain the cumulative plastic strains on the slip systems. Finally, the plastic strain tensor at a time indexed by i may be approximated as

$$\boldsymbol{\epsilon}_i^p = \sum_{\xi} \gamma_i^{(\xi)} \left(\mathbf{s}^{(\xi)} \otimes \mathbf{n}^{(\xi)}\right)_{sym}. \tag{4.20}$$

from the associated cumulative plastic shear strains.

A graphical representation of this procedure is shown in Figure 4.4. The back stress and plastic shear strain are initialized at zero for each slip system. The plastic strain quantities are orders of magnitude smaller than the total strain quantities in the HCF regime, and therefore their impact on redistribution of the stress and total strain tensors relative to the elastic solution are minimal. Accordingly, phenomena of cyclic stress redistribution and relaxation are neglected in this work, as well as local lattice rotation.

Finally, FIP fields are computed in all SVEs using Equation (4.15), and the extreme value distributions are extracted following the procedures of Section 4.3.4. Through the FIP EVDs, microstructures may be rank-ordered by their resistance to HCF.

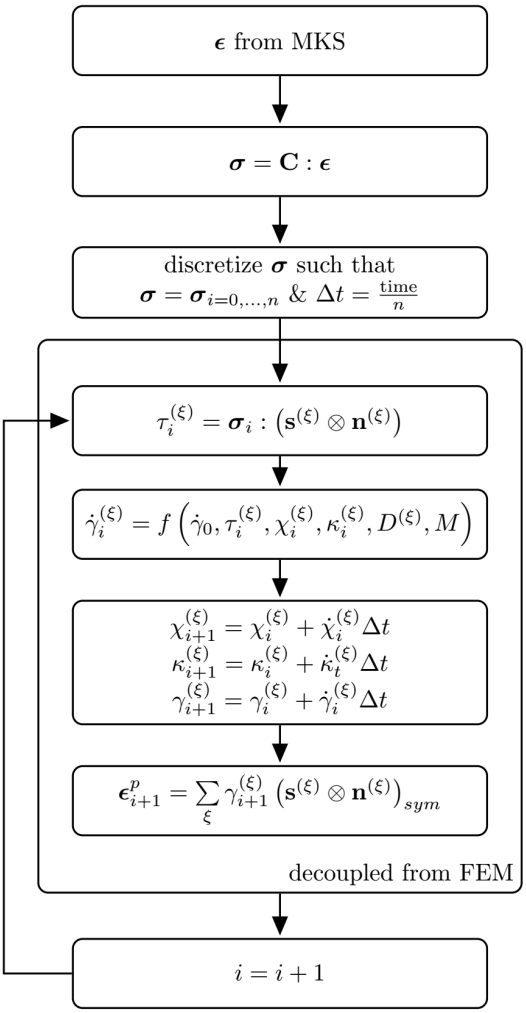

Figure 4.4: Flowchart for the forward Euler integration scheme used to estimate the local plastic strain tensor ($\boldsymbol{\epsilon}^p$) from the local total strain tensor ($\boldsymbol{\epsilon}$) provided by MKS.

4.5 Case Study

To demonstrate the protocols described in Section 4.4, four different α-titanium microstructures in three separate loading directions are rank-ordered by their HCF resistance. Synthetic microstructure volumes are first generated using the open-source DREAM.3D software. The MKS is then calibrated with linear-elastic FE simulations and employed to predict elastic strain fields in the volumes. Stresses are calculated from the elastic strain fields and the integration scheme is used to compute the cyclic plastic strains. These quantities are used to calculate the FIP fields in each SVE. The microstructures and loading directions are rank-ordered by their HCF resistance through a comparison of the FIP EVDs. The details of this case study are provided in the remainder of this section.

4.5.1 Digital Microstructures

Four crystallographic textures are selected for analysis in this work: (a) random, (b) β-annealed, (c) transverse, and (d) basal/transverse. The β-annealed texture is taken from previous work [6] while the other textures are extracted from the literature [70–72, 136]. All three-dimensional digital microstructures are generated using the open source DREAM.3D software [46] with inputs of desired grain-size, orientation, and misorientation distributions. The grain-size distribution for all microstructures is modeled as a log-normal distribution with a mean and standard deviation of $30\mu m$ and $15\mu m$, respectively. The instantiated microstructures contain 9,261 hexahedron elements, each with 8 integration points (i.e., C3D8-type in ABAQUS 6.10-1[77]) and an individual side length of $10\mu m$. Each digital SVE has a total side-length of $210\mu m$ in the x-, y-, and z-directions. A total of 500 SVEs are instantiated for each of the four microstructures and their statistics are compared to the desired statistics. Representative pole figures for each microstructure analyzed in this work are shown

in Figure 4.5. DREAM.3D is used to generate the fully periodic microstructures employed in this work.

To determine how many SVEs are adequate to approximate an RVE, the mean and standard deviation of a particular value of interest (elastic stiffness in this instance) are compared with tolerance values [156]. The details of these calculations are provided in the Appendix. As shown in Figure 4.6, the mean of the elastic stiffness converges extremely quickly (in fewer than 50 simulations) for loading in each direction while the standard deviation requires approximately 250 simulations for each loading direction. Similar results are found for the other textures.

4.5.2 MKS Model Calibration

The MKS framework described in Section 4.3.2 was successfully employed in prior work for the prediction of elastic strain fields in polycrstalline HCP microstructures [21, 23]. In this study, however, the influence coefficients of Equation (4.13) are recalibrated for the set of elastic parameters in Table 4.1. Truncation to the first term of Equation (4.14) is justified as α-titanium single crystals exhibit low contrast (e.g., the ratio of the highest modulus to the lowest modulus is approximately 1.40); prior work has shown that this truncation provides excellent results for composite systems with low to moderate contrasts [13, 14, 17, 21, 23]. Furthermore, only fifteen GSH basis functions are employed in Equation (4.12) and Equation (4.13), as it has been previously demonstrated that this is sufficient for the prediction of the elastic response of hexagonal polycrystals [21]. The influence coefficients are calibrated for all unique components of the strain tensor for three different loading directions.

The influence coefficients are calibrated using the linear-elastic FE responses (using ABAQUS) of uniform-textured SVEs (generated via DREAM.3D). For each loading direction (x, y and z), periodic, displacement-controlled boundary-conditions are employed such that the macroscopic strain tensor only has only one non-zero compo-

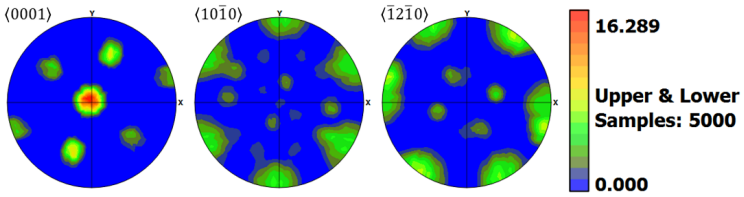

(a)

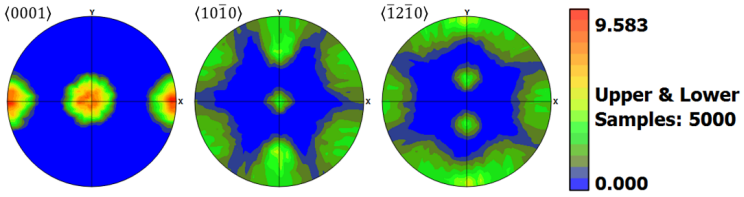

(b)

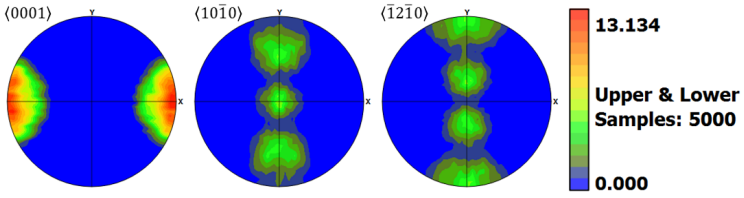

(c)

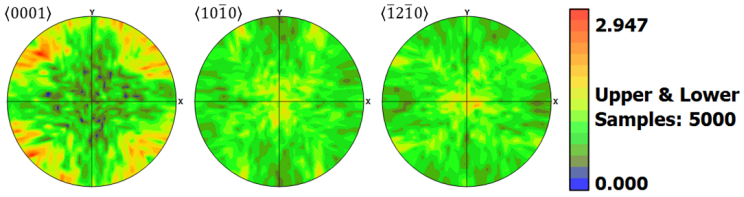

(d)

Figure 4.5: Representative pole figures for (a) β-annealed, (b) basal/transverse, (c) transverse, and (d) random texture inputs to DREAM.3D.

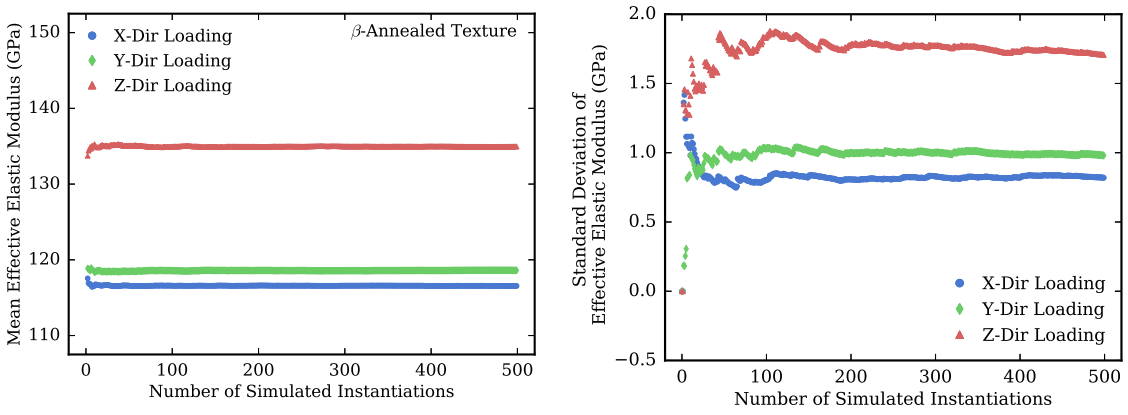

(a) (b)

Figure 4.6: The (a) mean and (b) standard deviation of the effective elastic modulus values for N number of MKS simulations of the β-annealed microstructure and for each loading direction.

nent (in the direction of loading). It is noted that the MKS influence coefficients may be calibrated for any desired macroscopic strain tensor; uniaxial strain is selected in this work because it has been successfully employed in many previous studies [13, 14, 17, 21, 23]. The number of SVEs used in calibration of the MKS is determined through examining the mean and maximum error metrics in the strain field predictions for different sets of validation SVEs. From this analysis, it was seen that an ensemble of 400 SVEs is sufficient to calibrate the influence coefficients. When elastic strain fields are compared for 100 SVEs not included in the calibration set, the mean voxel-to-voxel difference between MKS and linear-elastic FEM responses is 0.28% and the maximum error per microstructure averages to only 1.50% for the ϵ_{11} component. Furthermore, the MKS evaluation requires only 0.7 seconds on a single processor compared to the 10 minutes on four processors required for the linear-elastic FE simulation of a single SVE. The local stress fields are also predicted with high accuracy. The mean and average maximum error per microstructure are 1.00% and 2.37%, respectively, for the σ_{11} fields from 100 instantiations of the β-annealed microstructure simulated with CPFEM (subject to the cyclic loading described in Section 4.5.3) and

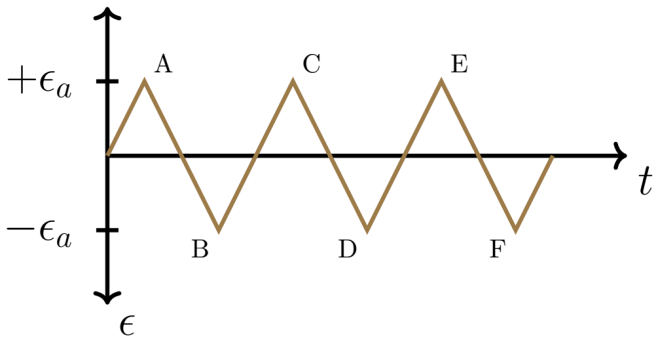

Figure 4.7: Schematic of the imposed strain versus time curve used in the work.

the MKS computed fields. These results indicate that stress relaxation or redistribution are minimal in the CPFEM simulations, which is an expected result for the HCF regime.

4.5.3 Auxiliary Decoupled Estimation of Plastic Strains

In this study, cyclic plastic strain fields are computed from the stress fields in each SVE using the decoupled numerical integration scheme described in Section 4.4. Three cycles of fully reversed ($R = -1$) cyclic loading are performed (see Figure (4.7)) to ensure that cyclic plastic strains saturate before FIPs are computed. Furthermore, loading is performed to 0.5% strain amplitude so that $|\boldsymbol{\epsilon}^p| \ll |\boldsymbol{\epsilon}^e|$ and stress redistribution is minimal. This roughly corresponds to 60-67% of the applied strain to yield, depending on the specific microstructure and loading direction. As a consequence, the stress and elastic strain fields are identical at points A, C, and E for any selected microstructure (this is not the case for the corresponding plastic strain fields). This is due to the evolution of the plasticity-related fields computed using the crystal plasticity framework presented earlier. In this decoupled numerical integration algorithm, the stress tensor is discretized into 50 increments for each loading segment (e.g., A-B, B-C, etc.).

To check the accuracy of the predicted plastic strain fields, CPFEM simulations are performed for 100 SVEs belonging to the β-annealed microstructure. The crystal

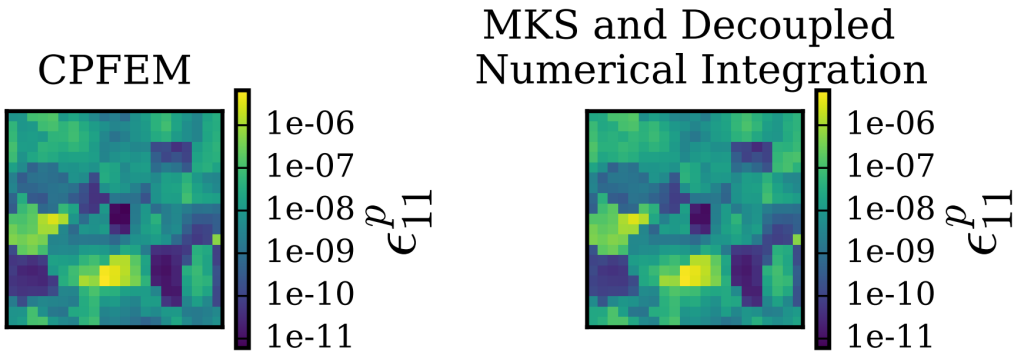

Figure 4.8: A two-dimensional cross-section comparison of the ϵ_{11}^p values from CPFEM (left) and MKS plus decoupled numerical integration (right).

plasticity formulation described in Section 4.3.1 is employed in Abaqus/Standard [77] through a User MATerial subroutine (UMAT) [157]. Three cycles of fully reversed loading are applied to the volumes using the same displacement-controlled, uniaxial-strain boundary-conditions described in Section 4.5.2. Figure 4.8 displays the plastic strain fields obtained using the novel protocols and CPFEM for a slice of an example SVE.

Figure 4.8 demonstrates that the plastic strain fields computed using the two approaches are indeed very similar. Note that the magnitudes of the plastic strains are several orders smaller than the elastic strain fields (the average ϵ_{11} strain is 0.5%). In this example SVE, the mean and maximum relative errors (of the novel approach versus CPFEM) do not exceed 0.39% and 0.84%, respectively, for any component of the plastic strain tensor. This error is defined as the local difference in plastic strains normalized by the maximum plastic strain obtained via CPFEM. This definition ensures that relative error is well characterized for locations in the volume exhibiting high levels of plastic strain. Later results will demonstrate that this level of agreement is sufficient to reliably rank-order the HCF performance of the microstructures studied in this work. The main benefit of the proposed approach continues to be the dramatic savings in computational cost. The CPFEM simulation requires approximately 45 minutes to complete on four processors (and a total of 8 ABAQUS licenses) per SVE,

while the decoupled numerical integration scheme requires 70 seconds on a single processor.

4.5.4 High Cycle Fatigue Analysis

Given the results of Section 4.5.3, FIP fields are computed for all SVEs in each loading direction using Equation (4.15). FIP EVDs are then calculated by compiling the maximum FIP value in each SVE. At this stage, it would be desirable to compare the FIP EVDs resulting from the novel protocols described in this work and the traditional CPFEM approach. Therefore, FIP EVDs are obtained from the CPFEM predicted plastic strain fields computed in the previous section for 100 β-annealed SVEs. In general, the FIP EVDs from the new protocol closely match the CPFEM results, as demonstrated in Figure 4.9. The two approaches indicate identical rank-ordering of HCF resistance based on a specified loading direction at a selected high probability of failure. At a low probability of failure, however, the rank-ordering is different between the two methods. This discrepancy can be traced back to the difference in the local plastic strain tensors, and that both methods approximate the local plastic strain tensors via Equation (4.20).

Due to the high computational costs of the conventional approach (which provide the main motivation for this work), comparisons between the two approaches were not be performed for all microstructures studied here. Consequently, the FIP EVDs were constructed using the novel protocols presented in this work for all four microstructure classes, each with a full ensemble of 500 SVEs (note that comparison presented in Figure 4.9 used only 100 SVEs). Figure 4.10 compares the resultant FIP EVDs for all four microstructures and three loading directions. As expected, the FIP EVDs of the random textured microstructure are nearly coincident for all loading directions. The basal/transverse and β-annealed textured microstructures exhibit similar FIP EVD responses, with the lowest fatigue resistance for loading in the z-direction.

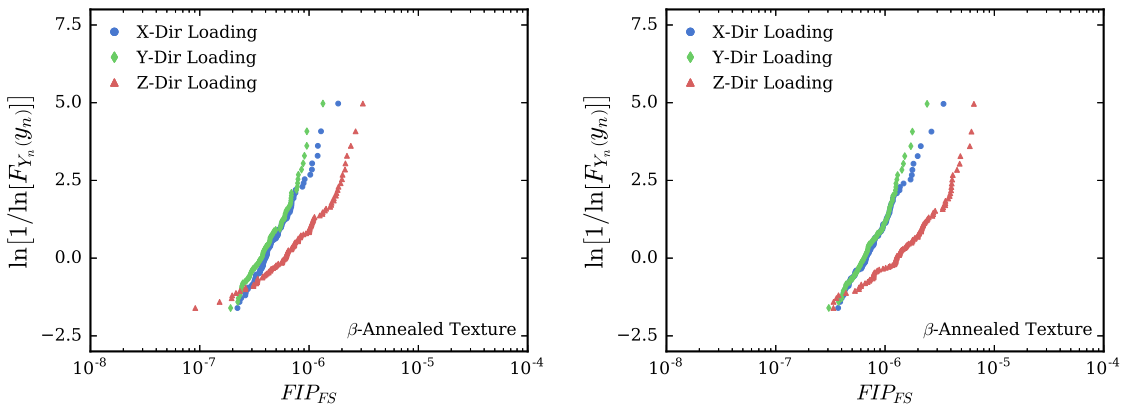

(a) (b)

Figure 4.9: Comparison of the β-annealed microstructure extreme value distribution Fatemi-Socie FIP plot with 100 SVEs obtained via (a) MKS plus decoupled numerical integration and (b) CPFEM.

Finally, the HCF resistance of the transverse textured microstructure is distinctly different from the other microstructures, exhibiting a significant positive correlation with the effective modulus in the direction of loading. This microstructure is distinct as compared to the other three due to a strong c-axis fiber texture component parallel to the sample x-axis. This particular texture feature essentially dominates this microstructure. As a result, when this sample is loaded along the x-axis, we should expect a minimum amount of interactions between neighboring grains, especially in the elastic regime due to the transverse isotropy of the elastic response in each crystal in the plane normal to the c-axis. It is therefore not surprising that x-axis loading produces the best HCF response for this microstructure with most of the FIP values being lower compared to the loading in the other directions. Note that this is the case despite the higher stiffness of the material along the x-axis (i.e., stresses are higher because the same strain amplitude is imposed in all cases) as compared to the other directions. It is also interesting to note that there are a few high FIP values in the x-axis loaded microstructure that are comparable to the values obtained in the other two loading directions on the same microstructure. This is because the high

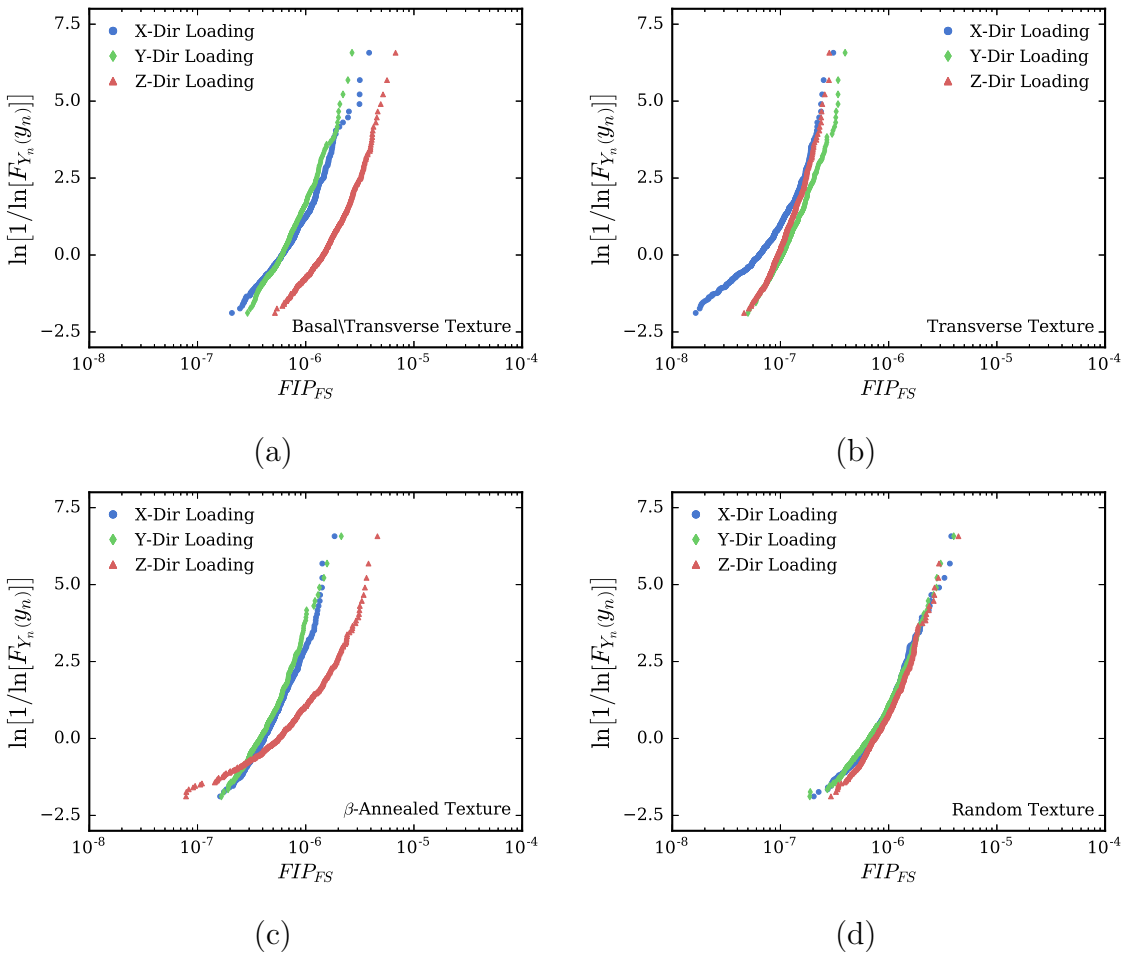

Figure 4.10: The extreme value distribution Fatemi-Socie FIP plot generated from the MKS and the decoupled numerical integration scheme with 500 SVEs for microstructures with the following textures: (a) basal/transverse, (b) transverse, (c) β-annealed and (d) random.

FIP values would correspond to locations of high local plastic strains. In the case of x-axis loading, once plastic deformation initiates, transverse isotropy in the local response of the c-axis grains is completely lost (note that only the elastic response is transversely isotropic in the HCP crystals) and the degree of interactions between neighboring grains dramatically increases. As a result of these strong interactions, the local plastic strains can be high in this microstructure. Overall, it should be noted that this microstructure provides the best HCF response out of all of the microstructures studied. This improved performance is largely attributed to lower levels of interactions between the neighboring grains (in the HCF loading regime dominated by elasticity).

4.6 Conclusions

A new methodology that employs MKS and a decoupled numerical integration scheme is presented to reliably predict cyclic plastic strain fields in hexagonal, α-titanium, polycrystalline aggregates under low-amplitude loading conditions. These quantities inform the computation of FIP distributions which are used to rank-order the HCF resistance of polycrystalline microstructures. This analysis is specifically designed to support rapid microstructure selection and optimization, assuming the proper material and application have been identified. These new protocols are demonstrated on an ensemble comprising over 6000 individual SVEs; the same task would demand major computational resources when using traditional CPFEM-based approaches. In fact, the low computational cost allows for the consideration of such a large ensemble of microstructures in the present work. The approximate speed-up of the new protocols is approximately 40x versus traditional CPFEM. The study also identifies the critical role of grain interactions in the HCF performance through a consideration of twelve different conditions (four microstructures, each loaded in three directions). While this study has established the feasibility of the new protocols, much additional work is

needed to extract new insights into the HCF response of polycrystalline microstructures. These will be targeted in future studies where the new protocols developed in this work will be employed on a much larger ensemble of microstructures.

Acknowledgments

This work was supported by the National Science Foundation under Grant No. CMMI-1333083. Any opinions, findings, and conclusions or recommendations expressed in this material are those of the authors and do not necessarily reflect the views of the National Science Foundation. MWP would like to thank Mr. Benjamin Smith for experimental characterizations of the β-annealed microstructure.

4.7 Appendix

In this work, the number of SVEs required to approximate the RVE for a microstructure of interest is selected by examining the convergence of the mean and standard deviation of the effective elastic modulus in each loading direction. In this section, protocols are set forth to calculate these moduli values for the boundary conditions employed in this work.

HCP crystal structures have a transversely isotropic elastic response, meaning that the elastic properties exhibit rotational symmetry around the HCP crystal c-axis. For α-titanium, the elastic modulus can vary between 104 and 146 GPa, the shear modulus between 40 and 47 GPa, and Poisson's ratio between 0.265 and 0.337. This degree of anisotropy for the elastic modulus (40%) and the shear modulus (18%) is much higher than that of other HCP metals [73] and can have a pronounced effect on the material deformation response.

Mechanical properties (such as elastic stiffness) can be determined from datasets generated in this study. Since the boundary conditions used in this work result

in non-zero normal stress components in all normal directions, additional steps are taken to determine directional effective elastic modulus values. The MKS determines local quantities, therefore the stress and strain components are volume-averaged to obtain the macroscopic quantities (e.g., $\langle \sigma_{ij} \rangle = \sum_{k=1}^{N} \sigma_{ij}^{k}/N$ where N is the total number of centroidal averaged values for uniform voxel size). The averaged stress and strain quantities are then used to determine the effective stiffness components. The effective stiffness tensor can then be inverted to recover the effective compliance tensor. Subsequently, the effective elastic modulus values for each loading direction are extracted from the diagonal components of the compliance tensor. The mean and standard deviation of the effective elastic modulus values for each loading direction and microstructure are presented in Table 4.2.

Table 4.2: Mean directional effective elastic modulus ($\pm$ std. dev.) for each microstructure.

Texture	$\mathbf{E}_x$ (GPa)	$\mathbf{E}_y$ (GPa)	$\mathbf{E}_z$ (GPa)
Random	123.4 $\pm$ 1.2	123.4 $\pm$ 1.2	120.0 $\pm$ 1.0
β-Annealed	116.5 $\pm$ 0.8	118.6 $\pm$ 1.0	135.0 $\pm$ 1.7
Basal/Transverse	122.8 $\pm$ 2.0	114.1 $\pm$ 0.2	135.6 $\pm$ 1.8
Transverse	144.8 $\pm$ 0.6	112.7 $\pm$ 0.2	112.8 $\pm$ 0.2

CHAPTER 5

MKS HOMOGENIZATION PROTOCOLS TO RANK-ORDER THE HIGH CYCLE FATIGUE RESISTANCE OF POLYCRYSTALLINE MICROSTRUCTURES

This work was under review for publication by a peer-reviewed journal as of April 20, 2017. The title of the paper is *Data-driven reduced-order models for rank-ordering the high cycle fatigue performance of polycrystalline microstructures*. The order of authorship is as follows: Noah H. Paulson, Matthew W. Priddy, David L. McDowell and Surya R. Kalidindi.

5.1 Abstract

Computationally efficient estimation of the fatigue response of polycrystalline materials is critical for the development of next generation materials in application domains such as transportation, health, security, and energy industries. This goal is non-trivial for fatigue of polycrystalline metals since the initiation and growth of fatigue cracks depends strongly on various attributes of the material microstructure, such as the sizes, shapes, orientations, and neighbors of individual grains. Furthermore, regions of microstructure most likely to initiate cracks correspond to the tails of the distributions of the microstructural features. This requires the execution of large numbers of experiments or simulations to capture the response of the material in a statistically

meaningful manner. In this work, a novel framework is described to rank-order the high cycle fatigue (HCF) resistance of various polycrystalline material microstructures through novel protocols that quantify these microstructures using 2-pt spatial correlations and represent them in a reduced-dimensional space using principal component analysis (PCA). Reduced-order linkages are then constructed to link microstructures to performance characteristics related to their HCF responses. These protocols are demonstrated for α-titanium, which exhibits heterogeneous microstructural features along with significant elastic and inelastic anisotropies at both the microscale and the macroscale.

5.2 Introduction

The estimation of fatigue resistance is a formidable barrier to the introduction of new polycrystalline materials in many advanced technology applications [58, 61, 62]. This is in large part due to the high cost of assessing the fatigue performance of these materials, which in turn depends on their heterogeneous microstructures. By nature, fatigue crack formation under high cycle fatigue (HCF) conditions is a rare event phenomenon, arising in local microstructure regions where a specific combination of shape, orientation and size of the constituent grains promotes the localization of stress and plastic strain [62]. The rarity of these critical features requires that large volumes of material be evaluated (via experiments or microstructure-sensitive computational models) to ensure the statistical robustness of the results [67, 80, 158, 159]. Validated protocols do not yet exist to identify these critical features in a systematic and reliable manner, and to quantify the relevant statistics of their rare occurrences in the material microstructure.

In the literature, attempts have been made to identify novel connections between fatigue properties and a variety of material parameters. Machine learning techniques have been utilized to predict fatigue crack growth rates in Nickel-base superalloys [160]

as well as the fatigue lives [161] and fatigue strengths [162] of a variety of steels. In these studies, the HCF property of interest (evaluated through experiments) is related to a set of material characteristics which generally includes composition, process path, and simple microstructure descriptors (e.g., grain size). While the process path used to create a material is indeed correlated to its properties, the connection is indirect and non-unique, since multiple process paths may lead to similar material microstructures. In reality, the material's hierarchical structure offers a much more direct path to correlate with properties, provided that the important structural features can be identified and reliably quantified. In other words, there is a clear incentive to move from process-property linkages to process-structure-property linkages. However, it is important to recognize that simple structural descriptors such as the average grain size and orientation distribution function (ODF) are unlikely to suffice in correlating to the HCF related properties of the material. It is therefore highly desirable to develop and demonstrate protocols that aim to explore the structure-property (S-P) linkages for HCF related properties of polycrystalline microstructures in a comprehensive and systematic manner. It is also desirable to express these S-P linkages in terms of reduced-order frameworks that are easily accessible to materials designers.

Computational approaches are well suited for the exploration of microstructure-sensitive S-P linkages for fatigue properties, as they reveal the local fields affecting the fatigue responses of detailed digital microstructures. In recent years, Pryzbyla and McDowell have developed a framework to investigate the fatigue performance of materials microstructures through the comparison of extremal distributions of local fatigue responses [66, 67]. In one recent study, this framework was employed to rank-order the HCF resistance of polycrystalline titanium microstructures [69]. Crystal plasticity finite element method (CPFEM) simulations were performed to extract tensorial stress and plastic strain fields, which were in turn used to evaluate fatigue indicator parameters (FIPs) defined to serve as surrogate measures for driving local

fatigue crack formation and growth. The HCF resistance of the microstructures could be rank-ordered by comparing the probability of a given FIP value being exceeded. From these analyses, the fatigue response was related to characteristics such as the feature size, crystallographic texture, and radial correlation of selected microstructure features. In another study, the HCF response of Ti-6242 was examined using an accelerated CPFEM framework [163]. In this work, the number of cycles until crack initiation was related to a parameter describing the surface area fraction of soft grains surrounding each hard grain (SAFSSG). Although it is generally expected that the HCF response of a structural alloy should correlate with the relevant statistics of occurrence of certain critical features in its polycrystalline microstructure, we are still in the early stages of establishing a rigorous framework for exploring and capturing such microstructure-HCF property linkages in practically useful forms that support materials design.

Over the past decade, Kalidindi and co-workers have developed a new framework for expressing process-structure-property (PSP) linkages of hierarchical materials in practically-useful, reduced-order forms [25]. Called the materials knowledge system (MKS), this framework leverages the comprehensive description of microstructure based on n-point spatial correlations [15, 19, 20, 22, 24, 34–37, 40, 54–56, 76, 119, 125–127] together with emerging data science toolsets. In previous work, the viability and advantages of the MKS framework were demonstrated in the prediction of the elastic and inelastic bulk properties of titanium polycrystals [76], transport properties of porous microstructures used in fuel cell applications [22], and the elastic strain fields in cubic and hexagonal polycrystals [21, 23]. In a recent publication [74], an MKS model was utilized successfully to speed-up the CPFEM simulations needed for the efficient rank-ordering of the HCF resistance of α-titanium microstructures. More specifically, instead of directly performing computationally expensive parametric sets of CPFEM simulations, an MKS localization model was calibrated and used

to predict the local elastic strain fields of polycrystalline microstructures. Using these elastic strain fields, the associated plastic strains were computed using crystal plasticity models and employed in evaluating the FIP distributions. The predicted FIP distributions matched well with CPFEM results, while providing a substantial reduction by a factor of 40 in computation time. Building further on this demonstration, it would be desirable to develop a framework that enables the evaluation of the performance of polycrystalline materials in microstructure-sensitive, extreme value problems (such as fatigue and fracture). To address this gap, it is necessary to seek objective, reduced-dimensional representations for both the microstructure and performance characteristics. Such low-dimensional representations of the inputs and outputs of the S-P linkages related to HCF are critical to facilitate dramatically accelerated forward and inverse protocols in materials selection and design.

The overarching goal of this work is to develop a data-driven, reduced-order structure-property linkage for the analysis of the microstructure-sensitive HCF performance of polycrystalline alloys. Success in advancing towards this goal requires two significant extensions to the MKS framework. The first challenge comes from the fact that the property of interest in these problems is the distribution of the local computed surrogate driving forces for fatigue crack initiation and early growth (i.e., the extreme value FIP distributions). In prior work using the MKS framework, the property of interest was generally defined as a suitably averaged quantity over a statistically representative material microstructural volume (such as effective modulus or yield strength). In this work, we critically explore if the fatigue response of the material can be captured by an appropriately parameterized functional form of the FIP distributions, with the parameters then serving as surrogate measures of HCF performance of the material (i.e., as properties in the S-P linkages). For computational efficiency, each microstructure is represented by a set or ensemble of statistical volume elements (SVEs) instead of a single, large representative volume element (RVE)

[80]. In other words, the HCF response of a microstructure is characterized by the performance characteristics of the entire set of SVEs associated with the selected material system. The second challenge therefore lies in selecting the size of the SVE set to support ensemble numerical simulations to evaluate the microstructure-sensitive response of each distinct material condition (nominal microstructure). To ensure reliable predictions, it is essential to establish a systematic approach to the characterization of the variability of predicted values for properties of the selected SVE sets. In this work, we demonstrate a computationally efficient strategy for addressing this gap. The effectiveness and computational benefits of the overall approach (addressing both challenges identified above) developed in this work will be demonstrated through the rank-ordering of the HCF responses of twelve distinct α-titanium microstructures.

5.3 New Framework for HCF related S-P Linkages

The main goal of this study is to develop and demonstrate a novel framework to link polycrystalline microstructures to their fatigue responses in reduced-order forms that are of high value to materials designers. As mentioned earlier, the success of this approach depends on our ability to identify suitable reduced-order descriptors for both the material microstructure as well as the HCF performance indicators (i.e., FIP distributions). These are discussed in detail next.

5.3.1 Microstructure Descriptors

The first critical task in the development of the framework is to select microstructures for the calibration (and later validation) of the S-P linkage. It is necessary to select a sufficient number of diverse microstructures to ensure that the linkage is robust and capable of predicting the properties of new microstructures. Furthermore, an adequate volume of material must be included to capture a statistically representative set of local fatigue responses. In theory, an RVE could be selected such that the

fatigue property would not be sensitive to the specific sample or a small increase in its size. Unfortunately, the computational analysis for HCF performance of such a large volume of material would be unfeasible using existing simulation methods and computational resources. Instead, it is common practice to select a sufficient number of smaller SVEs such that the quantity of interest relating to fatigue resistance converges [80]. Each SVE must be large enough to enclose the key correlation length-scales of interaction between various features in the microstructure [76].

The next task is to statistically quantify each of the selected microstructures. In previous work, spatial statistics were employed in the quantification of microstructures for S-P linkages [15, 20, 22, 24, 76]. Typically, each microstructure volume was assumed to be large enough to capture the bulk property of interest. In this work, however, microstructures are represented by ensembles of SVEs; therefore, it is expected that an ensemble of spatial statistics will be required to capture this inherent structural variability (which is critical to the local fatigue property) [25]. To construct this ensemble, the 2-point spatial correlations are computed for each individual SVE and represented in a reduced-dimensional space.

In previous work, 2-point spatial correlations were mainly evaluated for microstructures with distinct phases [15, 20, 22, 24, 37, 40, 54, 125, 126] where the local state in each cell is discretized into a limited number of bins. However, for polycrystalline materials, the local state is described by the crystal lattice orientation, g. Although it is possible to discretize the orientation space, a prohibitively large number of bins would be required. To address this conundrum, a spatial statistics framework for polycrystalline materials was developed [76]. In this framework, the 2-point spatial correlation, $f\left(g, g' | \boldsymbol{r}\right)$, describes the conditional probability density of finding orientations g and g' at the head and tail, respectively, of a vector $\boldsymbol{r}$ randomly placed in the microstructure. The spatial correlations may be expanded as a generalized Fourier

series as described in recent work [25, 76] in the form

$$f(g, g'|\boldsymbol{r})dgdg' \approx \sum_{K}\sum_{L}\sum_{\boldsymbol{t}} F_{\boldsymbol{t}}^{LK} T_L(g) T_K(g') \chi_{\boldsymbol{t}}(\boldsymbol{r}) dgdg' \tag{5.1}$$

where $F_{\boldsymbol{t}}^{LK}$ are the Fourier coefficients, $T_L(g)$ are the generalized spherical harmonic (GSH) functions which describe the functional dependence of spatial statistics on the local state and $\chi_{\boldsymbol{t}}(\boldsymbol{r})$ are the indicator basis functions used to bin the vector space corresponding to $\boldsymbol{r}$. The implementation of the GSH functions in the description of the local state (local crystalline lattice orientation) greatly facilitates the computation of the spatial correlations in polycrystalline microstructures. Further details of Equation (5.1) and the calculation of $F_{\boldsymbol{t}}^{LK}$ have already been described in detail in prior work [76].

While each SVE may be statistically represented with high fidelity using $F_{\boldsymbol{t}}^{LK}$, this Fourier coefficient set typically contains a large number of elements. Reduced-order representations of the structure in each SVE may be achieved using dimensionality-reduction techniques, most notably PCA. PCA is a linear, distance-preserving transformation which finds a new set of orthonormal feature vectors that are linear combinations of the existing feature vectors and are ordered in terms of the variance of the data [38]. In the remainder of this section, the spatial correlations for each SVE (indexed by $j = 1, 2, ..., J$) are portrayed in vectorized form $\{F_t^{(j)} | t = 1, 2, ..., R\}$ where the set of indices, $(\boldsymbol{t}, L, K)$, is replaced by the linear index t. Furthermore, J and R denote the total number of SVEs and the total number of features in the set of spatial correlations, respectively. With this terminology in place, the spatial correlations for a given SVE are expressed as

$$F_t^{(j)} = \sum_{i=1}^{\min((J-1),(R))} \alpha_i^{(j)} \varphi_{it} + \overline{F}_t \tag{5.2}$$

where $\overline{F}_t$ is the average of the spatial correlations (expressed as GSH Fourier coefficients) for all SVEs, $\alpha_i^{(j)}$ are the coordinates of each SVE in principal component space (herein called PC scores) and φ_{it} are the new PCA feature vectors (referred to as PC vectors). While the maximum number of PC vectors in Equation (5.2) is limited by the lesser of $(J-1)$ and R, in previous work far fewer were used to construct reliable S-P linkages [20, 22, 24, 54, 76]. This truncation in the PC representation of each set of spatial correlations may be denoted as $\{\alpha_i^{(j)} | i = 1, 2, ..., \tilde{R}\}$, where the truncation level, $\tilde{R}$, is a hyper-parameter which may be selected based on the desired representation fidelity. Note that many existing PCA algorithms will not accept the complex-valued $F_{\boldsymbol{t}}^{LK}$ coefficients. In such a scenario, it would be necessary to split the coefficients into real and complex features prior to the application of the PCA algorithm to conduct an equivalent analysis.

Finally, the reduced dimensionality of the representations of each SVE in the microstructure ensemble may be leveraged to represent the SVE sets (ensemble of SVEs used to represent each microstructure). To properly represent the microstructure, measures of both the typical structure and deviation from that structure must be obtained. It is natural to represent the typical microstructure as the mean of all the PC scores in the ensemble (or the central location in PC space). Likewise, the structural variability may be captured by the variance in the ensemble of PC scores. In this work, this quantity is captured by the total variance, in which the variance of the SVE ensemble is summed for all PC dimensions [15]

$$VAR_{tot} = \sum_{i}^{\tilde{R}} var(\alpha_i^{(j)}) \tag{5.3}$$

5.3.2 Representation of HCF Resistance

The selection of effective surrogate quantities of interest for HCF performance demands attention. The aim of this work is to rank-order the HCF resistance of poly-

crystalline microstructures. It is anticipated that the different SVE members of an SVE set used to represent a given microstructure are likely to exhibit distinctly different FIP distributions. Consequently, a single SVE cannot possibly represent the fatigue property for the entire sample. Practically speaking, the probability distribution of FIPs must be estimated from a large enough set of SVEs. Furthermore, the homogenization framework is statistical in nature and therefore not well suited to predict the field response in a single microstructure region (such as the location of the maximum FIP). In this work, the fatigue property is instead taken as the distribution of FIPs for all SVEs associated with a microstructure, with focus on the extreme values (large values). There are three main advantages to this approach. First, FIPs computed from a large volume of microstructure may be included; this ensures that a statistically meaningful extreme value distribution (EVD) may be achieved. Second, the fatigue property is connected to statistical trends in the microstructure picked up by the 2-point spatial correlations instead of hyper-specific regions in each microstructure. Last, a suitable functional form may be selected for the distribution of FIPs, and henceforth the HCF property of interest may be simply represented by the parameters (performance characteristics) of the surrogate FIP distribution.

In the literature, the Fatemi-Socie (F-S) FIP [60, 62–64] has been shown to be an effective surrogate measure for fatigue crack formation and growth in metals with planar slip (such as α-titanium) [51]. The F-S FIP is given by

$$FIP_{FS} = \frac{\Delta\bar{\gamma}^p_{max}}{2}\left[1 + k\frac{\bar{\sigma}^n_{max}}{\sigma_y}\right], \tag{5.4}$$

where $\Delta\bar{\gamma}^p_{max}$ is the maximum cyclic plastic shear strain range, $\bar{\sigma}^n_{max}$ is the maximum stress normal to the plastic shear, σ_y is the macroscopic yield strength of the material and k describes the impact of normal stress on the fatigue driving force. The over-bar indicates that a quantity is volume averaged, typically over the volume of a single

grain in the polycrystal [65]. This FIP is employed in the remainder of this work to characterize the local HCF response in each polycrystalline volume.

Previous studies in the literature have employed a variety of distributions in the description of extreme value phenomena [66, 67, 164]. The gamma distribution is chosen for this work as it was successfully used for the characterization of the extreme value FIP response of polycrystalline materials in previous studies [68]. The probability density function (PDF, Equation (5.5a)) and cumulative distribution function (CDF, Equation (5.5b)) of the gamma distribution are given by

$$f\left(z|\,\alpha\right) = \frac{1}{\Gamma\left(\alpha,0\right)} z^{\alpha-1} e^{-z} \tag{5.5a}$$

$$F\left(z|\,\alpha\right) = \frac{\Gamma\left(\alpha,z\right)}{\Gamma\left(\alpha,0\right)} \tag{5.5b}$$

$$\Gamma\left(\alpha,z^*\right) = \int_{z^*}^{\infty} z^{\alpha-1} e^{-z} dz, \qquad z = \frac{x-\mu}{\sigma}, \qquad \alpha > 0 \tag{5.5c}$$

where x is the continuous random variable of interest and α, μ and σ control the shape, location and spread of the distribution, respectively [68, 81]. Of these three parameters, the effect of α is most complex. For $\alpha > 0$ the distribution resembles the log-normal distribution, for $\alpha = 0$ the PDF becomes the exponential distribution, and for $\alpha < 0$ the distribution behaves like the reciprocal function. Note that for the expected range of α, the effects of α and σ on the CDF are similar. Consequently, depending on the fitting algorithm used, different combinations of α and σ may be selected. This ambiguity is undesirable as the parameters of the gamma distribution are expected to characterize the performance of the material. Therefore, in this framework, a reasonable value of α is selected and held constant so that the distributions of FIPs may be fit using only μ and σ. Furthermore, a threshold on the FIP responses is typically selected before fitting the gamma distribution [68, 164]. Only the largest FIP values are of interest, and thresholding improves the achieved fitting quality. Procedures for selecting the threshold will be discussed in a later section.

Note that the identification of the performance characteristics provides a sensible way to evaluate the number of SVEs required to represent the fatigue response of the microstructure of interest. The convergence of each performance characteristic with increasing numbers of SVEs for a particular microstructure may be taken as evidence of convergence of the fatigue response.

5.3.3 Formulation of the S-P Linkage

Given low-dimensional representations of both the microstructures and their associated HCF FIP distributions (as computed using existing physics-based models), the desired S-P linkage may be established. In previous studies where each microstructure volume was simply represented by a limited number of PC scores, multivariate polynomial expressions were particularly successful in the connection to effective properties [22, 24]. A similar approach is proposed in this work, where each microstructure is represented by the mean and variance of the PC scores of the ensemble of SVEs. Consequently, the S-P linkage takes the form

$$\mu^k, \sigma^k \approx \boldsymbol{A}_0 + \sum_i \boldsymbol{A}_i \tilde{\alpha}_i^k \tag{5.6}$$

where $\boldsymbol{A}_i$ are *physics-capturing* coefficients for each performance characteristic and $\tilde{\alpha}_i^k$ are the features which describe the microstructure indexed by k. More specifically, $\tilde{\alpha}_i^k$ are multiplicative combinations of elements of the mean vector and total variance, which may be expanded as follows,

$$\tilde{\alpha}_i^k = \overline{PC}_1{}^a \cdot \overline{PC}_2{}^b \cdot ... \cdot \overline{PC}_{\tilde{R}}{}^c \cdot VAR_{tot}{}^d \tag{5.7}$$

where $\overline{PC}_i{}^j$ is a mean PC score raised to the jth power, and $VAR_{tot}{}^d$ is the total variance raised to the dth power. Once the physics-capturing coefficients have been calibrated, the FIP distribution for a new microstructure may be predicted with

Equation (5.5), Equation (5.6) and Equation (5.7) at low computational expense.

5.4 Dataset Compilation

In this study, the framework described in Section 5.3 is employed to rank-order the HCF resistance of α-titanium microstructures. The first step in achieving this goal is to obtain ensembles of SVEs and their associated FIP responses. A set of twelve titanium microstructures were selected for this study. Eleven of these are used to calibrate the physics-capturing coefficients of Equation (5.6), and one is retained to demonstrate the effectiveness of the linkage in the prediction of the HCF response of previously unseen microstructures. Although one might consider this as a very limited set of microstructures, our goal here is to establish a novel framework and demonstrate its applicability to the very complex problem of extracting re-usable structure-property linkages related to HCF. Therefore, instead of focusing our efforts on generating a large dataset that would have practical significance to a specific application, we decided to aggregate available data from prior work (suitably supplemented where needed) [74–76] and focus more on the development of the data-centric framework described earlier. A total of 6000 SVEs and their HCF responses (via previous MKS studies [74, 75]) were obtained for the twelve microstructures. The remainder of this section describes the details of the procedures employed in obtaining these datasets.

5.4.1 Synthetic Microstructures

In this work, microstructures are represented by sets of synthetically generated SVEs. Each SVE must be of sufficient size to enclose the maximum correlation length-scale to capture key interactions between microstructure features. In previous work on the construction of localization linkages, it was observed that the magnitude of the Green's function based influence coefficients quickly decayed for both elastic and

inelastic response of materials with low- to moderate-contrast in the respective properties of the local microstructural constituents [13, 14, 17, 21, 23, 74]. In a recent MKS localization study for α-titanium microstructures, the influence functions decayed close to zero well within a 21x21x21 voxel region [74, 75]. Therefore, SVEs with the same voxel dimensions and $210\mu m$ side lengths are employed here.

The synthetic SVEs employed in this work are generated using the open source DREAM.3D software [46], using a log-normal grain size distribution with a mean grain size of $30\mu m$ and a $15\mu m$ standard deviation. Each SVE is assigned a distribution of crystal lattice orientations through a small set of texture components identified by Bunge Euler angles as well as intensities and spreads. A diverse set of textures employed in prior work [69, 132] are selected for this study. This set of textures exhibits both significant and subtle differences among the members, and are selected mainly to validate the framework presented in this work. DREAM.3D generates individual polycrystalline volumes through an ellipsoidal packing algorithm, and crystal lattice orientations are assigned to achieve the target texture. In theory, the synthetic SVEs generated for a selected set of target microstructure statistics should be statistically similar. In practice, this is not the case due to the practical difficulties associated with matching target microstructure statistics in a volume with a limited number of voxels. This structural variation within the ensemble of synthetic SVEs is in fact desirable as it mimics the variation of randomly sampled regions of experimentally characterized microstructures. These concepts will be further explored through the low-dimensional, statistical representations of each SVE in Section 5.5.1. In prior studies [74–76], 500 SVEs were generated using DREAM.3D for each of the 12 target microstructures used in this work. Figure 5.1 presents an example 3-D SVE colored by grain ID for each texture (shown as a (0002) pole figure). Microstructure J was reserved for the validation of this framework as it was expected to be an interpolation between the other microstructures in terms of its 2-point spatial statistics [76]. The

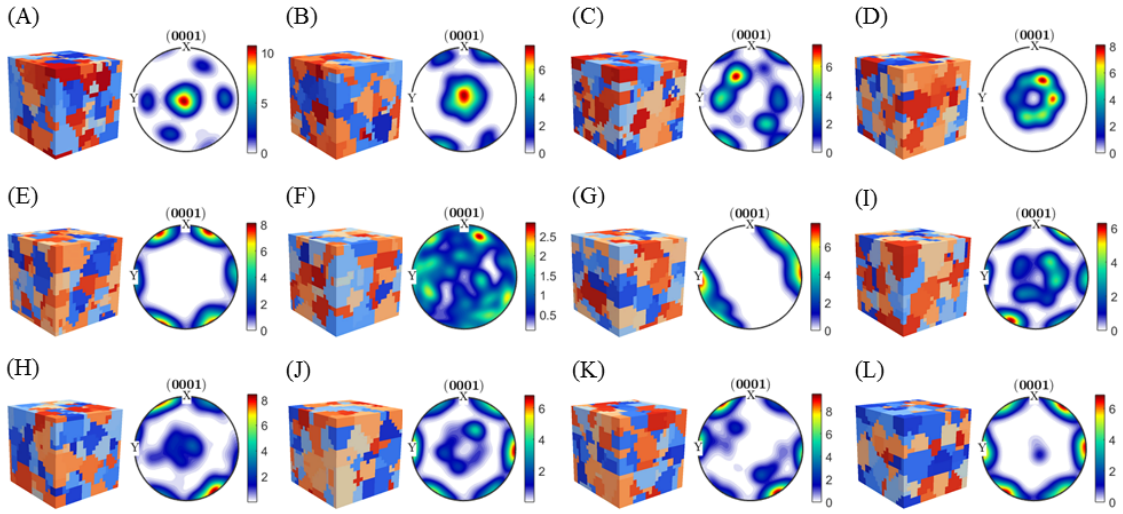

Figure 5.1: Grain ID maps and (0002) pole figures of sample SVEs for microstructures A through L.

remaining eleven microstructures are used for the calibration of the physics-capturing coefficients of Equation (5.6).

5.4.2 HCF Property Evaluation

In this framework, the computation of the FIP response requires that physics-based simulation methods be used to evaluate the stress and plastic strain fields in each SVE. Performance characteristics are extracted by fitting the EVD of FIP responses for a chosen ensemble of SVEs to the gamma distribution of Equation (5.5). These performance characteristics serve as reduced-order HCF property representations in the calibration of the physics-capturing coefficients of Equation (5.6). Typically, CPFEM cyclic simulation approaches [69, 163] are used to evaluate the response fields of the SVEs. In this case, however, response fields are evaluated using the MKS localization approach described in the introduction section. This decision significantly reduces the cost of obtaining the data set for this study [74, 75].

The details of the MKS localization approach have been described in numerous prior publications [21, 23, 74]. The framework is based on expressing the microscale

field as a series-sum of terms that represent the convolution of the microstructure fields with kernels derived from Green's functions (approximated here as influence functions) that are calibrated to results from numerical simulations. The MKS framework was used in a recent study [74, 75] to accelerate the rank-ordering of the HCF resistance of titanium microstructures. In that work, the MKS localization model was employed to predict the full tensorial elastic strain fields in the polycrystalline microstructures. At macroscopic strain levels far less than the bulk yield point, the local plastic strains are expected to be orders of magnitude smaller than the elastic strains. Consequently, in HCF evaluations, it is reasonable to assume that the stress fields are the same as those obtained in purely elastic simulations. In this prior work, it was shown that the elastic stress fields obtained from the MKS localization linkages can be used to reliably compute the local plastic strain fields and the associated FIP fields. This same strategy is employed to compute the FIP fields for all 6000 SVEs used in this work. The imposed loading condition corresponds to fully reversed loading cycles under imposed uniaxial-strain, with periodic boundary conditions.

5.5 Model Calibration

Given a sufficiently comprehensive dataset of microstructures and associated HCF responses, it becomes possible to develop a reduced-order S-P linkage. This task involves several steps. First, the SVEs representing the microstructures must be quantified through 2-point spatial statistics. Next, the spatial statistics representing each SVE are transformed into a reduced-dimensional space obtained through PCA. Finally, the physics-capturing coefficients may be calibrated through linear regression. The optimal linkage is systematically identified through a cross-validation procedure in which the quality of fit for linkages with different parameterizations are compared. In this section, each of these steps are presented in detail for the dataset identified in Section 5.4.

5.5.1 Quantification of Statistical Volume Elements

The first step in developing a reduced-dimensional representation of the microstructure is to quantify the SVEs using spatial statistics and PCA. Several details require further attention in the application of Equation (5.1) to compute the spatial statistics of each SVE. First, the truncation level of the GSH basis functions, $\tilde{L}$, used to represent the dependence of the spatial statistics on crystal lattice orientation must be selected. Due to the properties of the Fourier series, increasing $\tilde{L}$ also increases the fidelity of the representation of the spatial statistics, the dimensionality of the Fourier coefficients and the cost to compute them. For certain properties, only limited fidelity representations of microstructure are required to construct successful S-P linkages. For example, in previous work [19, 21, 52, 76, 78, 79], it was shown that only 15 GSH basis functions contribute to the efficacy of S-P linkages developed to predict elastic properties in hexagonally symmetric materials. Unfortunately, no such limit is known for inelastic properties, and many more basis functions may be required. No more than 41 basis functions are employed in this work to limit the cost of computing the spatial statistics; however, there is a possibility that the inclusion of more basis function may further improve the S-P linkage.

Additionally, $F_{\boldsymbol{t}}^{LK}$ is typically computed only for certain selected combinations of L and K. This practice stems from the realization that many redundancies exist in the Fourier coefficients of the spatial statistics [76, 126]. While PCA recognizes the linear redundancies, it cannot do so for the nonlinear ones. The final decision on which coefficients to compute requires balancing the fidelity of representation of the 2-point statistics and the dimensionality of the Fourier coefficients. In prior work [76], the quality of simple S-P linkages for the prediction of elastic stiffness and yield strength in α-titanium polycrystals was evaluated using different sets of $F_{\boldsymbol{t}}^{LK}$. Through this study, the optimal set of Fourier coefficients was identified as follows: $\{F_t^{L1} | L = 1, 2, ..., \tilde{L}\} \cup \{F_t^{L2} | L = 2, 3, ..., \tilde{L}\}$ for a total of $2\tilde{L} - 1$ combinations of L

and K. This same set is used in this work, as it was shown to be efficient and effective for the prediction of both elastic and inelastic properties.

Even after paring down the Fourier coefficients of the spatial statistics, $F_{\boldsymbol{t}}^{LK}$ is still a large set. It would be desirable to represent the spatial statistics of each SVE with a handful of numbers instead. To achieve this reduction in dimensionality, the PCA is applied on the SVEs associated with the calibration microstructures to identify the directions of maximum variance. SVEs associated with the validation microstructure are purposefully not included in this set to avoid biasing the eventual evaluation of the success of the S-P linkage in predicting the HCF response of new microstructures. From the results of the PCA algorithm, all SVEs may be transformed into the reduced-dimensional space. Depending on the choice of $\tilde{L}$, different levels of compaction are achieved. These trends are most clearly identified by examining the cumulative structural variance explained by increasing numbers of PCs (where the explained variance in one PC dimension is the variance of the PC scores of the SVEs in that dimension). Figure 5.2 shows that for each truncation level, $\tilde{L}$, the PCA cumulative explained variance asymptotically approaches 100% as the number of included PC dimensions increases. Furthermore, this rate of approach is slower for higher $\tilde{L}$. This result is intuitive, as spatial statistics defined with more GSH basis functions have higher fidelity, and therefore contain more nuanced information than spatial statistics defined with fewer GSH basis functions.

It is also informative to visualize the SVE ensembles to obtain a qualitative picture of the differences between microstructures. This is particularly convenient in PC space, where approximately 85% of the structural variation for $\tilde{L} = 15$ is captured in the first two PCs. Figure 5.3 simply plots each SVE by its PC scores in the first two components, color-coded by its associated microstructure. First, it is important to note that SVEs are well clustered by microstructure even in only two dimensions. This is a testament to the effectiveness of PCA in reducing the dimensionality of

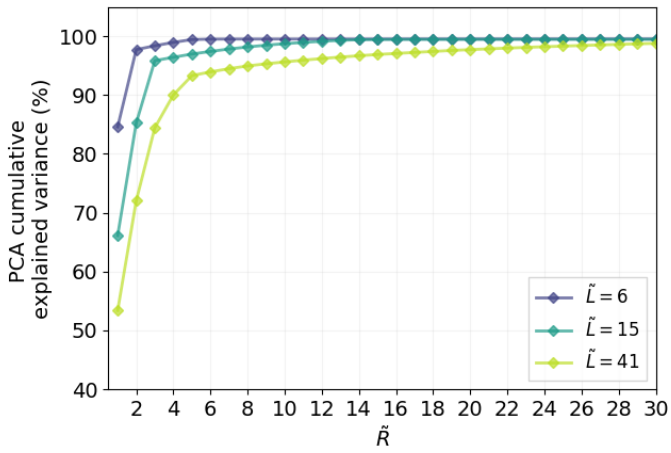

Figure 5.2: PCA cumulative explained variance as a function of $\tilde{R}$ and $\tilde{L}$.

the spatial statistics. Second, microstructures which are nearby in PC space are also qualitatively similar in terms of their texture. For example, microstructures J and K, which are neighbors in Figure 5.3, have very similar textures, as seen in the pole figures in Figure 5.1. In contrast, microstructures K and D, which are far apart in PC space, have distinctly different textures. While some simple texture trends can be identified by examining Figure 5.1 and Figure 5.3, more robust relationships would only become clear using more PC dimensions. Also, notice that the SVE ensembles for each microstructure do indeed have significant variance as was discussed in Section 5.4.1. Last, notice that the direction of maximum variance within each microstructure does not necessarily align with the overall direction of maximum variance for all SVEs (Microstructure E for example). This is just one demonstration of the statistical complexity of each ensemble of SVEs.

5.5.2 Microstructure Subdivision to Expand Available Calibration Data

Observant readers perhaps will anticipate a troubling feature of the calibration dataset; namely, the number of available microstructures is not sufficient to robustly calibrate the physics-capturing coefficients of Equation (5.6) for all but the simplest linkages. Furthermore, identifying and evaluating the properties of ideally hundreds or thou-

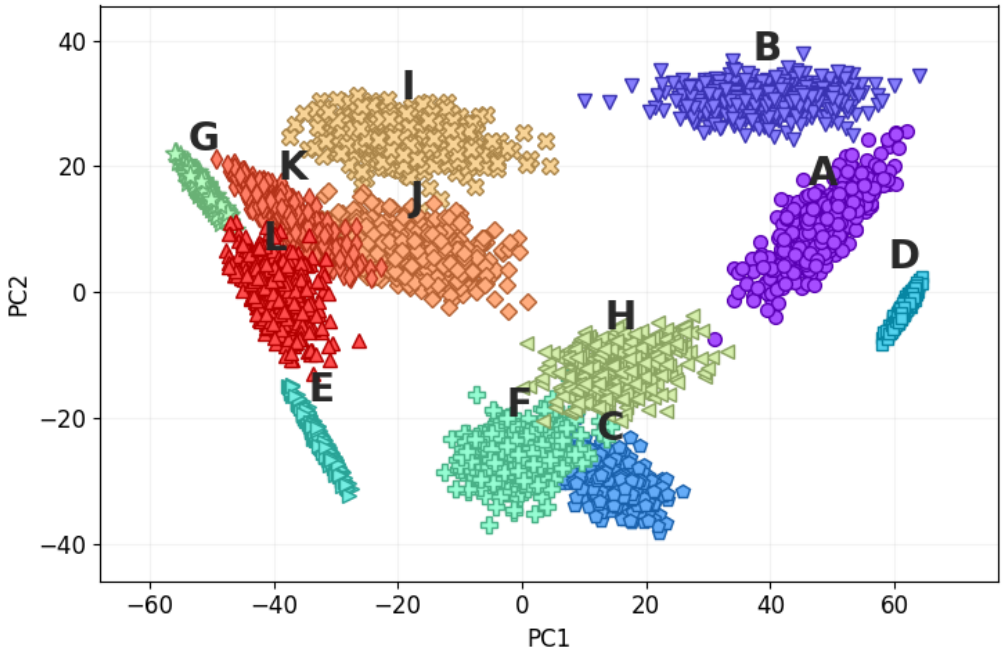

Figure 5.3: All 6000 SVEs are plotted by their coordinates in the first two principal components. The SVEs are color- and shape-coded by their associated microstructure type.

sands of microstructures would prove to be prohibitively expensive and time consuming. Clearly, it is desirable to extend the usefulness of a limited set of characterized microstructures. One opportunity is to sample a subset of SVEs from the greater ensemble of a particular microstructure. This subset of SVEs would have a different mean and total variance as well as different values for the performance characteristics than the original microstructure; therefore it would serve as a distinct "data point" from the perspective of Equation (5.6). Each microstructure could be sub-sampled in this manner many times to generate as many unique data points as required. Note that an individual SVE may be simultaneously included in multiple subsets so long as each subset has a unique statistical description and set of performance characteristics. Diminishing returns are expected for very large numbers of subsets as each subset is limited by the extents of the SVE ensemble of the parent microstructure in PC space. Consequently, 20 subsets will be selected from each original SVE ensemble. Prior to

the development of such an algorithm, certain details must be addressed, including the identification of the minimum number of SVEs required per subset and the desired spatial distribution of the SVEs themselves.

5.5.2.1 Identification of the Minimum SVE Set

One of the critical details in the implementation of such an algorithm is the identification of the minimum number of SVEs required per subset for a given size of SVE. This lower limit must be selected such that each subset approximates an RVE for the HCF property of interest. In this work, the convergence of the performance characteristics is closely tied to the threshold selected on the FIP distribution. If a low percentile threshold is selected, then each SVE in the ensemble will have many voxels with FIP responses exceeding the threshold, and relatively few SVEs will be required to achieve convergence of the performance characteristics. Unfortunately, the gamma distribution is not expected to closely fit such a broad-spectrum FIP response, especially in the tail of the distribution containing the largest FIP values that control the HCF resistance. Choosing a larger threshold may improve the quality of the gamma distribution fit for the extreme FIP values; however, this will also increase the number of SVEs required for convergence. This interplay is presented in Figure 5.4 for the microstructure labeled I, helping to guide the selection of both the FIP threshold and the minimum number of SVEs. Figure 5.4a shows the Gamma distribution fit to the FIP distribution for three different threshold levels. This plot provides the probability that a randomly selected voxel from any of the 500 SVEs in the ensemble will exceed the selected FIP value. The logarithmic scale on the vertical axis emphasizes the most extreme FIP responses (which would be obscured in a typical CDF plot). As evident in Figure 5.4, increasing the threshold on the FIP distribution brings the fit of the gamma distribution closer to the true FIP response. Figures 5.4b, 5.4c and 5.4d show the convergence of the performance characteristics for the 90th, 99th, and

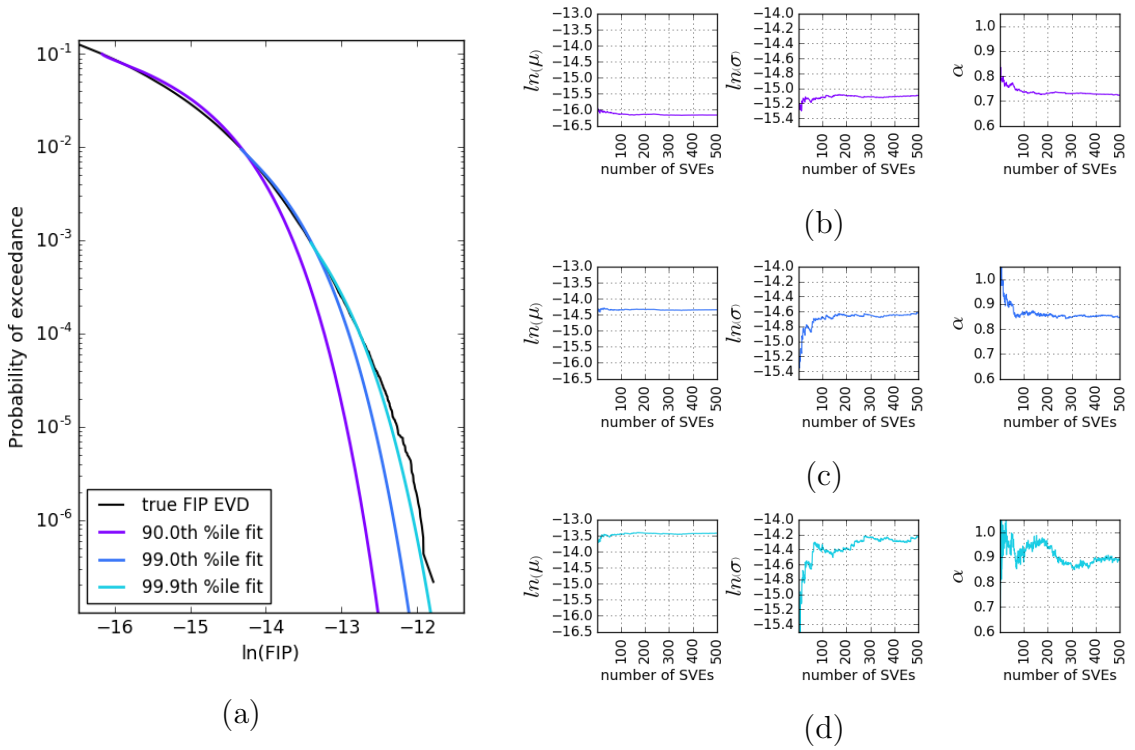

Figure 5.4: (a) The FIP probability of exceedance is plotted for the original FIP values for microstructure I alongside the gamma distribution fits with 90th, 99th and 99.9th percentile thresholds on the FIPs. The convergence of the performance characteristics is plotted for increasing numbers of included SVEs for the (b) 90th, (c) 99th, and (d) 99.9th percentile thresholds for microstructure I.

99.9th percentile thresholds on the FIP distribution, respectively. While convergence is achieved for subsets of fewer than 100 SVEs for the 90th and 99th percentile FIP thresholds, more than 500 SVEs may be required for the 99.9th percentile threshold (based on σ and α). From this analysis, it appears that the best compromise between convergence and accuracy-of-fit is achieved for a 99th percentile FIP threshold and a minimum of 100 SVEs. Lastly, Figure 5.4c indicates that it is most suitable to hold α constant at a value of 0.85.

It is sometimes useful to characterize the extreme value distribution of FIP responses through a comparison of the mean and thresholded FIP responses. Consequently, the mean and standard deviation of the full FIP distributions (including all 500 SVEs) are computed for each microstructure. This allows for comparison of

the mean and 99th percentile FIP responses. For the twelve microstructures under consideration, the 99th percentile FIP is between 3.19 (for microstructure K) and 4.32 (for microstructure I) standard deviations greater than the mean FIP. This reinforces the fact that the extreme value distributions considered here are 3-5 standard deviations from the mean of the overall probability distribution of FIPs, consistent with industry practice regarding low probability of failure of design of fatigue critical components.

5.5.2.2 Subset Selection Algorithm

At this point, it is appropriate to devise a strategy to select which SVEs to assign to each subset. To retain the predictive capabilities of the resultant linkage, it would be desirable to select subsets such that the distribution of PC scores of the SVEs are reminiscent of the characteristic distributions of the original ensembles. Conveniently, the estimated PDF of each original SVE ensemble clearly resembles a multivariate Gaussian distribution. Accordingly, SVEs should be selected such that each subset approximates some desired multivariate Gaussian. Furthermore, these subsets must be selected to exhibit a wide range of mean locations and total variances to enhance the richness of the calibration set. Lastly, each subset is restricted to sample only from one SVE ensemble to reduce the complexity of the calculation.

The next step is to develop an algorithm to identify reasonable target distributions for the selection of a subset. First, it is useful to isolate the SVE set of the microstructure of interest and transform it to a frame aligned with its directions of maximum variance. This task is easily achieved through another local application of PCA. Next, it is conditioned that the target multivariate Gaussian distribution has zero co-variance with respect to the frame aligned with the principal directions of the original SVE set. The following relationships may be defined to randomly generate

suitable target parameterizations of the multivariate Gaussian distribution, i.e.,

$$m_t = s_o\, x, \quad x \sim U([-1, 1]) \tag{5.8a}$$

$$s_t = s_o\, log_{1000}(y), \quad y \sim U\left(\left[1000^{0.5}, 1000^{0.5}\right]\right) \tag{5.8b}$$

where s_o is the sample standard deviation of the original SVE set, and m_t and s_t are the sample means and standard deviations of the desired subset, respectively. From Equation (5.8b), m_t is no more than one standard deviation distance from the center of the original SVE set in each dimension. Equation (5.8b) ensures that s_t ranges between $s_o/2$ and s_o in each dimension, yet is heavily weighted towards s_o. Equation (5.8) is formulated so that the subsets are similar in size to the original SVE ensembles, yet vary significantly in terms of their mean location and shape.

Finally, an algorithm is developed to select the optimal set of SVEs to match the target multivariate Gaussian distribution. Although there are many potential ways to achieve this task, in this work the difference between the target PDF and the PDF of the selected points is iteratively minimized. To start, the subset is initialized to contain every SVE from the original ensemble. In each iteration, kernel density estimation (KDE) [165] is used to estimate the multidimensional PDF of all SVEs in the subset. KDE is an alternative approach to traditional histograms for the estimation of the PDF of discrete data points through the summation of Gaussian distributions assigned to each data point (although other kernels shapes may be employed) [165]. Once the PDF of the subset is estimated, the error is computed against the target multivariate Gaussian PDF. Based on the error, the point with the maximum positive error is removed from the subset, and the iterations are continued until the subset retains a desired number of points. Unfortunately, the algorithm tends to select points clustered by the characteristic length-scale of the Gaussian kernel in KDE, called the bandwidth. To avoid the formation of these patterns, the

bandwidth is randomized each iteration per the following relationship, i.e.,

$$\text{bandwidth} = U([0.6, 0.8]) * w, \qquad w = \sigma\left(\frac{N(D+2)}{4}\right)^{\frac{-1}{D+4}} \tag{5.9}$$

where ω is the bandwidth according Silverman's rule of thumb, σ is the standard deviation of the data-points in each dimension, N is the number of data points, and D is the number of dimensions [166]. Note that in each iteration the selected bandwidth is smaller than what Silverman's rule of thumb suggests; this results in a slightly noisier PDF with higher fidelity in local regions. Three-dimensional Gaussians were matched to ensure a good quality of fit for each target statistic.

5.5.3 S-P Linkage Selection

With a sufficiently large number of SVE subsets and associated performance characteristics, it becomes possible to obtain an S-P linkage for the prediction of FIP EVDs. Specifically, the physics-capturing coefficients of Equation (5.6) may be calibrated for any selected subset of features (from the set identified in Equation (5.7)) using a variety of regression techniques. The selection of the feature set, however, is non-trivial, as Equation (5.7) can describe an infinite variety of features. Even if one limits the numbers of principal components and the polynomial order employed, the number of features is still prohibitively large. Consequently, it is necessary to employ feature selection techniques to reduce the feature set. Finally, cross-validation techniques are used to identify the specific form of the S-P linkage with the best predictive capability while not resulting in over-fits. The remainder of this section discusses each of these steps in detail.

First, bounds on the set of features defined by Equation (5.7) are delineated based on previous experience and common sense. Figure 5.2 provides some guidance with regard to the selection of $\tilde{R}$; for the three GSH truncation levels explored in this work,

it appears that the first 25 principal components capture over 98% of the structural variance, therefore this will serve as a reasonable cutoff in this work. As mentioned in Section 5.5.1, it is difficult to know what truncation level in the GSH basis functions is sufficient to capture the inelastic response of a microstructure. Therefore, the maximum set of 41 GSH basis functions are employed in this work. In prior studies where polynomial terms were also used, it was observed that higher order terms have the potential to reduce the stability of the linkage [22, 24]. Furthermore, as the polynomial degree increases, the number of features explodes. From a starting set of 26 features, 352 second-order features can be generated, and 3276 third-order features can be generated. In recognition of these two issues, in this study only first- and second-order terms are used.

At this stage, there are still 378 unique features to contend with, so it is helpful to employ techniques to identify which features are expected to contribute the most to the final linkage. The simplest of such techniques are univariate filtering algorithms, which independently evaluate the strength of relationship between each individual feature and the response variable of interest. In this work, the Pearson correlation [82] of each feature versus the response variable (μ or σ) is evaluated, and features are rank-ordered based on the absolute value of the correlation (the Pearson correlation measures the positive or negative linear dependence between two variables and provides an output between -1 and 1). A ranking of the top ten features and their associated Pearson correlation scores versus μ and σ is shown in Table 5.1. The top ranked features contain combinations of the mean subset locations in each dimension and the total variance in unpredictable combinations. Also, note that individual first-order features are present repeatedly in higher order features; for example, VAR_{tot} is present in four of the top ten features for μ. Furthermore, seven of the features are common between the top ten sets for μ and σ. This is likely due to the high correlation ($R = 0.941$) between μ and σ for the calibration SVE subsets.

Table 5.1: The top ten features ranked by the Pearson correlation are presented for both performance characteristics.

Feature Ranking	μ	Pearson Correlation	σ	Pearson Correlation
1	$\overline{PC}_1 \cdot \overline{PC}_7$	-0.654	$\overline{PC}_1 \cdot \overline{PC}_7$	-0.730
2	$\overline{PC}_1 \cdot \overline{PC}_5$	0.647	$\overline{PC}_1 \cdot \overline{PC}_5$	0.639
3	$\overline{PC}_7$	0.586	$\overline{PC}_6$	0.590
4	$\overline{PC}_6$	0.574	$\overline{PC}_7$	0.588
5	$\overline{PC}_7 \cdot VAR_{tot}$	0.547	$\overline{PC}_6 \cdot VAR_{tot}$	0.529
6	$\overline{PC}_5 \cdot \overline{PC}_6$	0.535	$\overline{PC}_7 \cdot VAR_{tot}$	0.518
7	VAR_{tot}	0.519	$\overline{PC}_3 \cdot \overline{PC}_5$	0.517
8	$\overline{PC}_6 \cdot VAR_{tot}$	0.515	$\overline{PC}_1 \cdot \overline{PC}_{25}$	0.514
9	${VAR_{tot}}^2$	0.495	${\overline{PC}_1}^2$	-0.506
10	$\overline{PC}_1 \cdot \overline{PC}_{25}$	0.491	$\overline{PC}_5$	-0.472

Once the top features have been identified, training and cross-validation errors are used to select the final form of the S-P linkage. Training error refers to the error in the linkage's prediction of the responses of the calibration data-points. In cross-validation, data-points are removed from the calibration set and reserved before the linkage is calibrated. The error in the model's prediction of the reserved data points can be used as a measure by which to compare differently parametrized models. This is typically done a number of times for each model to ensure the statistical robustness of the measure. In this work, the collection of subsets associated with each original microstructure are split into two, for a total of 22 groups of 10 subsets. Cross-validation is then performed for each of these groups. This approach is less computationally expensive than Leave-One-Out cross-validation [22, 24, 76] and encourages the selection of a simple linkage with strong predictive capability for new microstructures. Cross-validation is performed for linkages that include increasing numbers of the previously-identified, highly-correlated features. The results of this procedure are presented in Figures 5.5a and 5.5b for μ and σ, respectively. Notice that the cross-validation error first decreases along with the training error as more features are included, but eventually diverges as the number of features become too

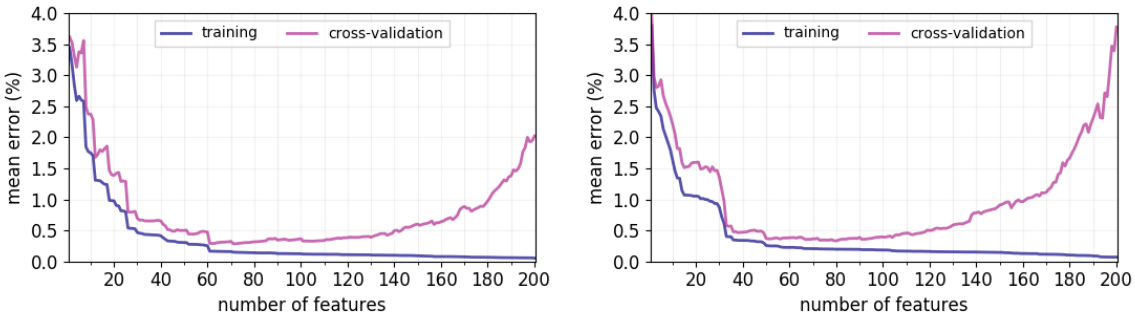

(a) (b)

Figure 5.5: The training and cross-validation errors are plotted versus the number of top-ranking features included in the linkage for (a) μ, and (b) σ.

large for the number of data-points. The ideal number of features is selected by identifying where the training and cross-validation errors begin to diverge. From these plots, the top 61 and 50 features are selected for μ and σ, respectively, both at a GSH truncation level of $\tilde{L} = 41$.

5.6 Model Validation

In the previous section, the specific form of Equation (5.6) expected to be most successful in the prediction of the performance characteristics was selected. It is now desirable to evaluate the efficacy of the selected linkage in rank-ordering the HCF resistance of titanium microstructures. First, the accuracy of the prediction of μ and σ is evaluated for all 240 SVE subsets (used for both calibration and validation). The success of the linkage in this regard is clearly demonstrated in Figure 5.6, where μ and σ as obtained via simulation and S-P linkage methods are compared for each SVE subset. Notice that μ and σ are presented on a log scale as they differ by orders of magnitude between subsets. The mean relative error (normalized by the mean log-scaled value of the performance characteristic) is 0.2% for both μ and σ and does not exceed 1.3% in any individual subset. Furthermore, the predicted performance characteristics for subsets associated with the validation microstructure (labeled J)

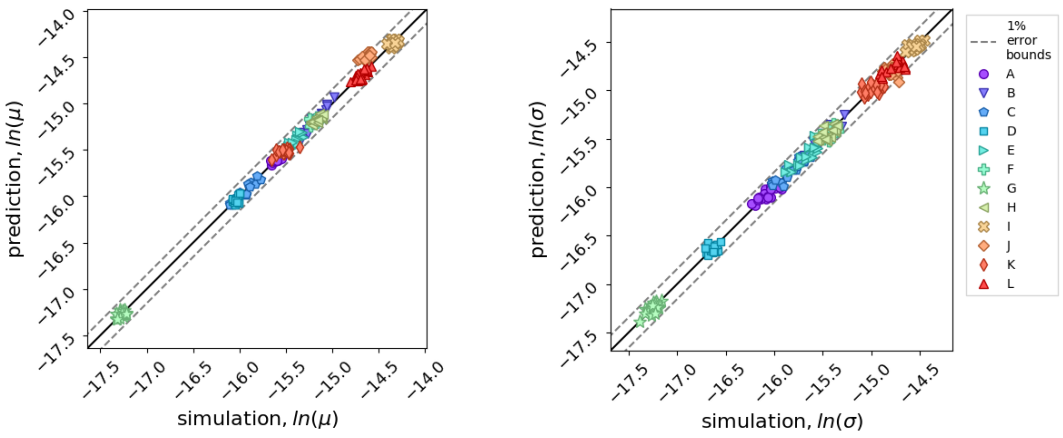

(a) (b)

Figure 5.6: The simulated versus predicted performance characteristics for each SVE subset are plotted for (a) $ln(\mu)$ and (b) $ln(\sigma)$.

exhibit low error.

Evaluating the error in the predicted performance characteristics of the SVE subsets is informative, but it is important to demonstrate the prediction of the EVDs of the original twelve microstructures, each represented by 500 SVEs. To this end, Equation (5.6) is used to predict μ and σ for each original SVE set. Along with the preset shape parameter, α, this set of performance characteristics can be used to predict the FIP EVD for each microstructure. The results of this evaluation are presented in Figure 5.7, where the true simulated FIP EVDs (on the left) are compared against the EVDs predicted using the reduced-order model developed in this study (on the right). Clearly, the general rank-ordering of the microstructures in terms of HCF resistance is preserved in the MKS prediction, with microstructures G and I exhibiting the most and least resistance to HCF, respectively. Furthermore, note that the EVD of the validation microstructure J is nearly coincident with microstructure L in the results of both approaches. Small differences can be identified between the simulations and MKS in terms of the probability-of-exceedance at which two EVDs intersect. This is most clear when examining the EVDs of microstructures A and C, where the crossover point is at a lower probability-of-exceedance level for

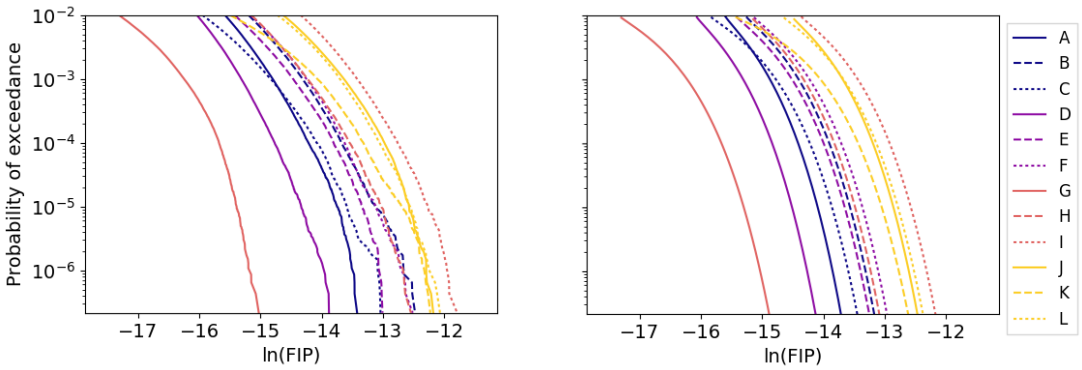

(a) (b)

Figure 5.7: FIP EVDs are plotted for each of the twelve microstructures (labeled A through L) extracted from (a) the original simulations and (b) the novel MKS protocols.

the MKS prediction than for the simulation. Note that the probability of exceedance is plotted on a log scale, and tends to emphasize the features of the FIP EVD at extremely low probabilities. Consequently, certain features of the simulated EVDs below 10^{-5} probability are not mirrored in the predicted EVDs. These deviations are not large enough, however, to significantly change the rank-ordering of the HCF resistance. These results indicate that the MKS protocols can reliably rank-order the HCF resistance of a diverse set of polycrystalline microstructures.

It is also important to emphasize the computational benefits of these new MKS protocols. If traditional CPFEM simulations were employed to evaluate the HCF resistance of these twelve microstructures (as represented by 6000 SVEs), roughly 18,000 hours of CPU time on a supercomputer would be required. Furthermore, this evaluation would potentially require numerous software licenses, especially if simulations were performed in parallel. Once the physics-capturing coefficients are calibrated, the MKS protocols can complete the same task in fewer than 6 hours (this includes the time required to compute the spatial statistics, transform to PC space and evaluate Equation (5.6)). This represents more than a 3000 times speed-up in CPU time versus traditional approaches to conduct this evaluation of extreme value

FIP distributions for the SVEs of interest.

5.7 Conclusions

In this work, novel protocols are developed to connect reduced-order representations of polycrystalline microstructures and their associated fatigue responses. This approach combines several recent advancements in the computational analysis of fatigue and the development of microstructure-sensitive models for polycrystalline materials, resulting in robust and efficient protocols well suited for next-generation materials development efforts. The methodology is successfully demonstrated in the rank-ordering of the HCF resistance of twelve diverse α-titanium microstructures. Not only are the extreme value fatigue responses accurately predicted, but the computational cost of the analysis is dramatically reduced; the measured speed-up in CPU time versus traditional approaches is over 3000 times.

Acknowledgments

This work was supported by the National Science Foundation under Grant No. CMMI-1333083. Any opinions, findings, and conclusions or recommendations expressed in this material are those of the authors and do not necessarily reflect the views of the National Science Foundation.

CHAPTER 6

MKS HOMOGENIZATION PROTOCOLS TO RANK-ORDER THE TRANSITION FATIGUE RESISTANCE OF POLYCRYSTALLINE MICROSTRUCTURES

This work was being prepared for submission to a peer-reviewed journal as of April 20, 2017. The title of the paper is *Reduced-order microstructure-sensitive protocols to rank-order the transition fatigue resistance of polycrystalline microstructures*. The order of authorship is as follows: Noah H. Paulson, Matthew W. Priddy, David L. McDowell and Surya R. Kalidindi.

6.1 Abstract

The transition fatigue regime between low cycle fatigue (LCF) and high cycle fatigue (HCF) is often addressed in the design and performance evaluation of load-bearing components used in many structural applications. Transition fatigue is characterized by elevated levels of local inelastic deformation in significant regions of the microstructure as compared to HCF. Typically, crystal plasticity finite element method (CPFEM) simulations are performed to model this phenomenon and to rank-order microstructures by their resistance to crack formation and early growth in the regime of transition fatigue. Unfortunately, these approaches require significant computational resources, inhibiting their use to explore novel materials for transition fatigue

resistance. Reduced-order, microstructure-sensitive models are needed to accelerate the search for next-generation, fatigue-resistant materials. In a recent study, Paulson et al. [167] extended the materials knowledge system (MKS) framework for rank-ordering the HCF resistance of polycrystalline microstructures. The efficacy of this approach lies in the reduced-dimensional representation of microstructures through 2-point spatial correlations and principal component analysis (PCA), in addition to the characterization of the HCF response with a small set of performance measures. In this work, these same protocols are critically evaluated for their applicability to rank-order the transition fatigue resistance of the same class of polycrystalline microstructures subjected to increased strain amplitudes. Success in this endeavor requires the formation of homogenization linkages that account for the significantly higher levels of local inelastic deformation and stress redistribution in transition fatigue as compared to HCF. A set of 12 α-titanium microstructures generated using the open access DREAM.3D software [46] are employed for this evaluation.

6.2 Introduction

In high-performance applications, components may be subject to repeated loads that bring large volumes of material close to macroscopic plastic yield. Crack growth in the transition regime between HCF and LCF is a life-limiting phenomenon for components in aerospace, security and motorsport industries. The regime of transition fatigue is physically complex, with zones of cyclic plastic strain spreading beyond stress concentrations across grains and other microstructure features [58, 62, 83]. Furthermore, nearest-neighbor interactions in the material become prevalent, exhibited through phenomena such as stress- and strain-redistribution [74]. Consequently, enhancements to the transition fatigue life require simulations of microscale stress and strain distributions. Generally, such simulations demand significant investments of computational resources and time. It is desirable to develop and employ suitable

low-computational cost, reduced-order models that can reliably account for the influence of the microstructure and cyclic stress and plastic strain redistribution on the drivers for transition fatigue life in materials design efforts.

In recent years, McDowell and co-workers have developed a computational framework that employs CPFEM simulations to rank-order the fatigue resistance of microstructures under different loading conditions [66, 67, 69]. Specifically, cyclic CPFEM simulations are performed on sets of statistical volume elements (SVEs) for each microstructure of interest. Then, from the resultant stress and cyclic plastic strains, surrogate measures of the driving force for fatigue crack initiation and growth, called fatigue indicator parameters (FIPs), are evaluated at all spatial locations in the SVEs. The fatigue performance of different microstructures for a selected loading condition is compared through extreme value distributions (EVDs) of the FIP responses. Unfortunately, these protocols require significant numbers of computationally expensive CPFEM simulations, which limits progress towards high throughput exploration protocols for the assessment of candidate materials.

Reduced-order computational and analytical approaches provide an opportunity to efficiently explore fatigue responses in the regime between HCF and LCF for various materials. Stress- and strain-based methods have been used for decades to quickly estimate the fatigue lives of materials at different strain amplitudes [168]. While efficient, these empirical approaches heavily rely on experimentally determined parameters and do not account for the huge variability exhibited in microstructures caused by variations in the processing path. Indeed, quantitative accounting of the influence of microstructure on the transition fatigue life has been a major challenge because of the very complex interactions that occur naturally between the heterogeneous constituents present in the material internal structure at multiple hierarchical length scales. Although a number of composite theories account for some of the simpler details of the material microstructure [9–12], they have not been successful in

accounting for the rich and complex interactions of individual grains in a polycrystalline microstructure, especially for loading conditions leading to elevated levels of local inelastic strains in the transition fatigue regime. High fidelity, reduced-order representations of the microstructure are therefore central to the formulation of high-value structure-property linkages for transition fatigue performance that can be used effectively in high throughput explorations of large materials design spaces.

The materials knowledge system (MKS) framework has been developed over the past decade by Kalidindi and co-workers for the mining of microstructure-sensitive homogenization and localization linkages [13–30, 74, 76, 169]. The MKS homogenization framework [15, 18, 20, 22, 24, 27–30, 76] is particularly promising because the reduced-order representations of microstructure it employs are well suited to rapid materials exploration efforts. Specifically, microstructure volumes are quantified using n-point spatial correlations and are transformed into a reduced-dimensional space using PCA. The homogenization relationship may then be calibrated using an ensemble of microstructure volumes and their associated effective properties (obtained via experiments or existing physics-based models) or processing parameters. This framework has been extensively demonstrated in the prediction of the transport properties of porous fuel cell materials [22], the inelastic properties of dual-phase steels [24] and the bulk mechanical properties of polycrystalline α-titanium microstructures. It has also been successfully extended to the prediction of structure evolution of mechanically strained polymers [28], additive manufacturing [29], and ternary eutectic alloys [30] in addition to the development of process-structure-properties linkages in dual-phase steels from experimental assays [27].

In prior work, the MKS homogenization framework was extended to rank-order polycrystalline microstructures according to their resistance to the formation of cracks under HCF [167]. As a case study, 12 α-titanium microstructures were rank-ordered, with each microstructure corresponding to a distinct crystallographic texture. First,

the ensembles of synthetically-generated SVEs (which represent each microstructure) were quantified using a formulation of the 2-point spatial statistics specialized for polycrystalline materials [76]. PCA was then performed to reduce the dimensionality of the spatial-statistics, and each microstructure was represented by the mean location and variance of the ensemble of spatial statistics in principal-component (PC) space. Simultaneously, the gamma distribution was fit to the EVD of FIP responses representing the performance of each microstructure (as computed using a physics-based model). The extracted fitting parameters (called performance characteristics) then served as the effective properties in the MKS homogenization linkage. The S-P linkage was then calibrated using the reduced-order representations of 11 of the 12 microstructures and their associated performance characteristics. The success of the resultant S-P linkage was demonstrated through the comparison of the rank-ordering of all 12 microstructures (according to their resistance to HCF) to the results of brute force CPFEM, while providing a 3000 times speed-up in CPU time versus the traditional CPFEM approach.

This study builds on the prior work described above and specifically evaluates the efficacy of the recently developed MKS homogenization protocols for rank-ordering polycrystalline microstructures based on their transition fatigue performance. This performance is assessed via surrogate measures for the driving force to form fatigue cracks. The same 12 α-titanium microstructures from the prior study [167] are employed here. Due to the significant phenomenological differences between HCF and transition fatigue, the MKS protocols must overcome a new set of challenges in the transition fatigue regime. First, the cyclic plastic strains are expected to be several orders of magnitude larger than those in HCF, with comparable magnitudes to the elastic strains (and even total strains) in certain microstructure locations. Furthermore, due to these larger cyclic plastic strain ranges, redistribution of both cyclic stress and plastic strain is expected to be significant. To effectively rank-order poly-

crystalline microstructures based on their resistance to transition fatigue, the MKS must capture the sophisticated physics underpinning these phenomena. There are reasons to believe that this approach has merit; in prior work [76], the MKS framework was employed to construct a structure-property (S-P) linkage for yield strength in α-titanium, where the degree of plastic deformation was also significant. The flexibility of the MKS framework in representing both linear and non-linear phenomena stems from the use of n-point spatial statistics to capture microstructure interactions as suggested by statistical continuum theories [19, 31–33].

6.3 Description of Protocols

The protocols developed by Paulson et al. [167] to rank-order the fatigue resistance of polycrystalline microstructures rely on reduced-order representations of both the microstructure and the fatigue performance. This is challenging because each microstructure must be represented by a set of SVEs, constituting a massive quantity of salient information. The following strategy is enacted to confront this challenge; first, all SVEs representing the microstructure are quantified using 2-point spatial statistics and transformed into a reduced-dimensional space using PCA. Then, each microstructure may be represented by the mean location of the SVE spatial statistics in PC space along with a measure of the structural variance. Similarly, the local responses (i.e., computed surrogate measures of driving force to form fatigue cracks, based on FIPs) of all SVEs in the ensemble contribute to the overall transition fatigue performance of the microstructure. In this framework, this performance is characterized by the EVD of FIP responses in all SVEs. This large set of discrete data points may be represented by three parameters after fitting the raw FIP EVD to the gamma distribution, as described next. Figure 6.1 presents a general outline of the steps involved in the calibration of the homogenization linkage. These steps with be discussed further throughout the remainder of this work.

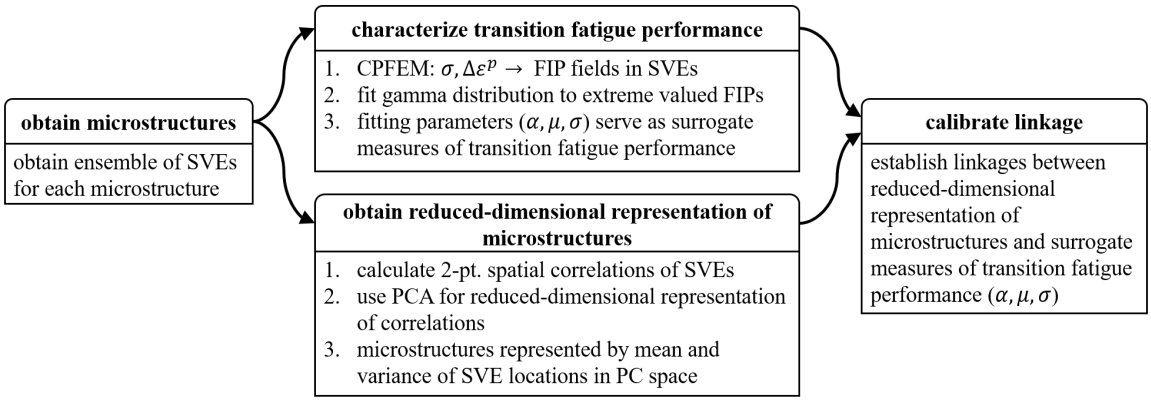

Figure 6.1: Schematic summary of the protocols employed to calibrate an MKS homogenization linkage for the characterization of transition fatigue performance in polycrystalline microstructures.

The extreme value distribution of FIPs is obtained by applying a threshold to the raw distribution of FIP responses in the SVE ensemble. The threshold level is generally selected to achieve a high-quality fit of the gamma distribution to the data. Generally, the extreme FIP values are of most interest and 99% or more of the lower values are discarded. The probability density function (PDF) and cumulative distribution function (CDF) of the gamma distribution are given by Equation (6.1a) and Equation (6.1b), respectively [68, 81], as follows

$$f\left(z|\,\alpha\right) = \frac{1}{\Gamma\left(\alpha, 0\right)} z^{\alpha-1} e^{-z} \tag{6.1a}$$

$$F\left(z|\,\alpha\right) = \frac{\Gamma\left(\alpha, z\right)}{\Gamma\left(\alpha, 0\right)} \tag{6.1b}$$

$$\Gamma\left(\alpha, z^*\right) = \int_{z^*}^{\infty} z^{\alpha-1} e^{-z} dz, \qquad z = \frac{x-\mu}{\sigma}, \qquad \alpha > 0 \tag{6.1c}$$

In Equation (6.1), α, μ and σ are parameters which control the shape, location and scaling of the gamma distribution, respectively, and are further described in the preceding study [167]. These parameters are collectively referred to as "performance characteristics" and are employed as surrogate measures for the transition fatigue performance in the remainder of this work. The convergence of the performance

characteristics with the inclusion of increasing numbers of SVEs is used to identify a sufficient minimum number of SVEs needed to represent the microstructure. The effects of α and σ on the shape of the CDF of the gamma distribution are similar in their typical ranges for fitting the EVD of FIP responses, so to improve the consistency of the fitted parameters, a reasonable α is typically selected and held constant before obtaining μ and σ.

The first step in the reduced-order representation of the ensemble of SVEs associated with each microstructure is to quantify individual SVEs using spatial statistics. The 2-point spatial correlations for polycrystals, denoted $f(g, g'|\boldsymbol{r})$, describe the conditional probability density of finding crystal lattice orientations g and g' at the head and tail, respectively, of a vector $\boldsymbol{r}$ randomly placed in the microstructure. The spatial correlations are represented using a Generalized Fourier series (GFS), allowing for the efficient description of their dependence on crystal lattice orientation using generalized spherical harmonics (GSH) [41]. In previous work, only 15 GSH basis functions were required to construct S-P linkages for the prediction of elastic properties [21, 23, 76]. The GFS representation of the 2-point spatial correlations for orientation is given by

$$f(g, g'|\boldsymbol{r})dgdg' \approx \sum_{K}^{\tilde{L}} \sum_{L}^{\tilde{L}} \sum_{\boldsymbol{t}} F_{\boldsymbol{t}}^{LK} T_L(g) T_K(g') \chi_{\boldsymbol{t}}(\boldsymbol{r}) dgdg' \tag{6.2}$$

where $F_{\boldsymbol{t}}^{LK}$ are the GFS coefficients, $T_I(g)$ are the GSH basis functions which describe the functional dependence on the crystal lattice orientation, $\chi_{\boldsymbol{t}}(\boldsymbol{r})$ are the indicator basis functions which describe the functional dependence on $\boldsymbol{r}$ and $\tilde{L}$ refers to the truncation in the number of GSH basis functions employed in the GFS.

$F_{\boldsymbol{t}}^{LK}$ may consist of a very large set of coefficients, especially for the high-fidelity representation of polycrystalline microstructures. Consequently, PCA is employed to obtain a reduced-dimensional representation of the spatial statistics. The PCA algorithm finds directions of maximum variance in the original data so that the re-

sultant PC vectors are orthogonal and ordered from highest to lowest variance [38]. PCA is performed on all J SVEs in the calibration ensemble, each indexed by j. To prepare the GFS coefficients for PCA, a new linear index, t, is defined for unique sets of $\{\boldsymbol{t}, L, K\}$. The total number of sets indexed by t is denoted R. Finally, the PCA representation of the GFS coefficients is given by

$$F_t^{(j)} = \sum_{i=1}^{\min((J-1),(R))} \alpha_i^{(j)} \varphi_{it} + \overline{F}_t \tag{6.3}$$

where ϕ_{it} is the PC direction indexed by i, $\alpha_i^{(j)}$ is the coordinate of the SVE indexed by j in the ith PC direction (referred to as a PC score) and $\overline{F}_t$ is the average of the GFS coefficients for the J SVEs along the feature index, t. To fully represent the spatial statistics of an SVE in the calibration set, all available PC directions must be employed; however, due to the qualities of PCA, high-fidelity representations may be obtained with only a handful of PC directions [15, 18, 20, 22, 24, 76]. When truncation is employed, the total number of PC directions is denoted by $\tilde{R}$.

After obtaining reduced-dimensional representations of the SVEs, each microstructure is represented by the mean structure and variance of its associated ensemble of SVEs. The mean structure is simply computed as the average of the PC scores for all SVEs in the ensemble. There are numerous options for representing the spread of the structures in the ensemble (the variance in each PC dimension, hyper-volume of the convex hull, etc.); however, in this framework, the scalar-valued total variance measure is employed to retain the reduced-dimensional representation of each microstructure. The total variance is simply given by

$$VAR_{tot} = \sum_{i}^{\tilde{R}} var(\alpha_i^{(j)}) \tag{6.4}$$

where the variance of the ensemble in each PC direction is summed.

Finally, the reduced-order representations of the microstructures and their performance characteristics (as computed from the response fields simulated via existing physics-based models) are employed to calibrate the S-P linkage. The form of this linkage is given by

$$\mu^k, \sigma^k \approx \boldsymbol{A}_0 + \sum_l \boldsymbol{A}_l \tilde{\alpha}_l^k \tag{6.5}$$

where $\tilde{\alpha}_l^k$ is feature l of the microstructure indexed by k which may consist of multiplicative combinations of mean PC scores (for a particular PC direction) and the total variance and $\boldsymbol{A}_l$ is the physics-capturing coefficient associated with feature l. Once these coefficients are calibrated, Equation (6.1) and Equation (6.5) can be employed in concert to estimate the EVD of FIPs for a new microstructure at very low computational cost.

The number of data-points available for the calibration of the physics-capturing coefficients of Equation (6.5) is equal to the number of available microstructures. This limitation is likely to curb the maximum complexity and sophistication of the final homogenization linkage, because models with large numbers of features (and more complex features) tend to require numerous data-points for their calibration. Thankfully, it is often easier to obtain large numbers of SVEs for a small number of target microstructures than the reverse. Consequently, a boot-strapping strategy was employed in the preceding study [167]. In this approach, the number of available data-points for calibration is expanded by repeatedly sub-sampling the SVE ensembles such that each SVE subset has enough members to approximate an RVE for the property of interest. To ensure the richness of the calibration dataset, SVE subsets should be selected such that they have a wide variety of mean locations and shapes.

6.4 Case Study

In this work, the protocols discussed in Section 6.3 are employed to rank-order the transition fatigue resistance of 12 unique α-titanium microstructures. The HCP α-titanium single-crystals exhibit significant anisotropy in their elastic and inelastic responses, making the prediction of microstructure-sensitive phenomena difficult. Furthermore, the transition fatigue resistance of titanium alloys is of great interest in the aerospace industry and in other high-performance applications. The remainder of this section describes each step of the development of the homogenization linkage in detail. This includes obtaining microstructure volumes, performing CPFEM simulations, calculating surrogate measures for the fatigue performance, quantifying microstructures using 2-point spatial statistics and PCA, calibrating the homogenization linkage, validating the linkage and discussing the results.

6.4.1 Microstructure SVE Ensembles

The α-titanium microstructures employed in this work are the same 12 used in previous studies [74–76, 167]. Each microstructure is assigned a distinct target texture inspired by those seen in the literature [69–73]. Texture is expected to have a significant impact on the transition fatigue performance due to the local elastic and inelastic anisotropy exhibited by α-titanium polycrystals [6, 73]. Each microstructure is assigned a log-normal grain size distribution with a $30\mu m$ mean and $15\mu m$ standard deviation.

In previous studies [74–76], 500 SVEs were generated for each of the 12 target microstructures using DREAM.3D [46] (for a total of 6000 SVEs). Only 3800 SVEs are used in this study to reduce the computational expense of running CPFEM simulations for the calibration and validation of the linkage (the reasons for this particular selection of SVEs are presented in later sections). The SVEs have dimensions of

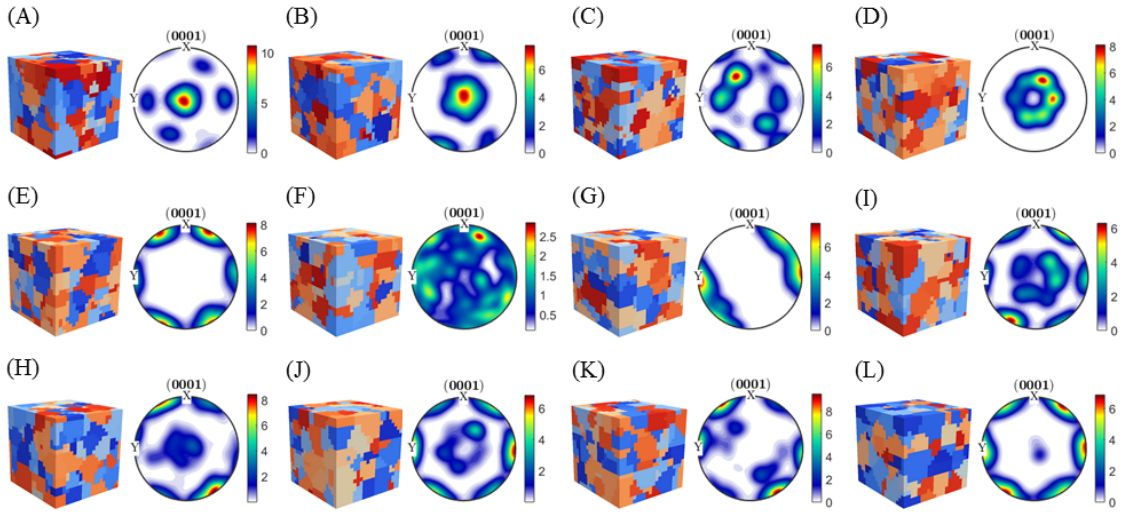

Figure 6.2: Example SVEs and (0001) pole figures are presented for each microstructure [167].

21x21x21 voxels (the voxels have side lengths of $10\mu m$). This results in approximately 215 grains per SVE. This SVE size has been previously demonstrated to capture the maximum length-scale of interaction between microstructure features in materials systems with similar contrasts in both elastic and inelastic properties [13, 14, 17, 21, 23]. In the generation of synthetic microstructure volumes, DREAM.3D first matches the target grain-size distribution using an ellipsoidal packing algorithm. The texture is subsequently matched to the target texture (in this case represented though the orientation distribution function of individual crystallites). For each microstructure, Figure 6.2 presents an example SVE colored by grain-id and the associated (0001) pole figure; 11 of the 12 microstructures are used to calibrate the physics-capturing coefficients of Equation (6.5) and the remaining microstructure (labeled J) is reserved to validate the predictive capability of the resultant linkage. This same strategy was employed in the preceding study [167].

6.4.2 Crystal Plasticity Simulations

In this study, CPFEM simulations are employed to model the transition fatigue responses of the microstructures. Specifically, the stress and cyclic plastic strain outputs are required to compute the EVD of FIPs for each α-titanium microstructure. These are subsequently used to calibrate the physics-capturing coefficients of Equation (6.5). The crystal-plasticity framework that underlies the CPFEM was developed by McDowell and co-workers for Ti-6Al-4V [6, 47–51]. Most recently, Smith and McDowell calibrated the model parameters with both monotonic and cyclic experimental results [6].

In the CPFEM simulations, SVEs are loaded to a maximum strain amplitude of 0.75%, or roughly 90-99% of the strain at yielding, depending on the specific microstructure. This level of inelastic deformation ensures that the material is loaded in the transition fatigue regime. Three cycles of fully-reversed loading (R=-1) are performed before evaluating the FIPs so that the cyclic plastic strains have the chance to saturate. Displacement-controlled, fully-periodic boundary conditions are utilized to implement uniaxial loading, resulting in a SVE-level stress tensor with non-zero component σ_{11}. CPFEM simulations are performed for all 500 SVEs associated with microstructure I. These results are employed to study the convergence of the surrogate measures for transition fatigue performance and therefore to determine how many CPFEM simulations should be performed for each remaining microstructure. The results of this analysis as presented in Section 6.4.3 dictate that 300 CPFEM simulations be performed for each microstructure.

Figure 6.3 displays the grain-ID map for an example SVE along with its associated total strain and plastic strain magnitudes (note that total strains and plastic strains use the same color-bar). These results are obtained from a CPFEM simulation after three loading cycles. Generally, the plastic strains are smaller than the total strains; however, in certain locations the plastic strain magnitude may be comparable to or

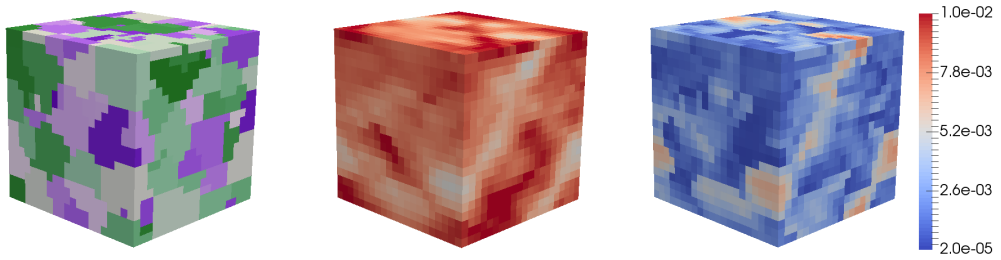

(a) (b) (c)

Figure 6.3: (a) grain ID, (b) total strain magnitude and (c) plastic strain magnitude fields for example SVE from microstructure A.

exceed the total strain magnitude. This phenomenon is observed predominantly in locations where the total strain is small. Furthermore, notice that the plastic strains are not limited to isolated grains with high stress concentration (as in HCF); areas of high plastic strain magnitude span groups of multiple contiguous grains in the polycrystalline SVE.

6.4.3 Surrogate Measures for Transition Fatigue Performance

After the stress and cyclic plastic strain fields are computed though CPFEM simulations, the Fatemi-Socie (F-S) FIP [60, 62–64, 74] is computed in all voxel locations. The F-S FIP is given by

$$FIP_{FS} = \frac{\Delta\bar{\gamma}^p_{max}}{2}\left[1 + k\frac{\bar{\sigma}^n_{max}}{\sigma_y}\right], \tag{6.6}$$

where $\Delta\overline{\gamma}^p_{max}$ is the maximum cyclic plastic shear strain range, $\overline{\sigma}^n_{max}$ is the maximum stress normal to that shear strain, σ_y is the macroscopic yield strength and k is a constant controlling the contribution of normal stress to the driving force for fatigue crack formation and early growth. The over-line indicates that a quantity is volume averaged. In this study, volume averaging is performed over a 2x2x2 block of voxels including the spatial location of interest.

The transition fatigue performance is then characterized by the fitting parameters

of the gamma distribution to the set of extreme-valued FIP responses. These fitting parameters, referred to as performance characteristics, serve as surrogate measures of the transition fatigue performance. Once the physics-capturing coefficients of Equation (6.5) are calibrated, the homogenization linkage can be used to predict these performance characteristics for previously unseen microstructures at low computational cost. Additionally, FIP EVDs for the microstructures can be reconstructed from the predicted performance characteristics using Equation (6.1), enabling the rank-ordering of microstructures by their resistance to transition fatigue.

Characterization of the transition fatigue performance requires the careful selection of several hyper-parameters. The choice of the threshold on the FIP distribution and the number of SVEs required to approximate the transition fatigue performance of an RVE are coupled. In short, if a high threshold is selected (where fewer FIP values are contributed by each SVE to the final FIP EVD) the gamma distribution fit improves and the minimum number of SVEs required increases. Alternately, a low threshold results in a worse fit to the gamma distribution, but generally requires fewer SVEs to approximate the RVE. These trends are evident in Figure 6.4 where the gamma distribution fit and convergence of the performance characteristics are examined using a set of CPFEM results from 500 SVEs associated with microstructure I.

In Figure 6.4a the gamma distribution fits for 99th, 99.9th and 99.99th percentile thresholds of the FIPs are plotted on top of the raw FIP distribution. For any selected value of the abscissa, the ordinate indicates the probability that a randomly selected voxel in the SVE set will have a higher FIP value. Note that the log scale emphasizes discrepancies in the distributions at very low probabilities of exceedance. Clearly, the 99th percentile threshold results in a low-quality fit while the 99.9th and 99.99th percentile fits are acceptable. Figures 6.4b, 6.4c and 6.4d show the convergence of the three performance characteristics for increasing numbers of SVEs and different FIP

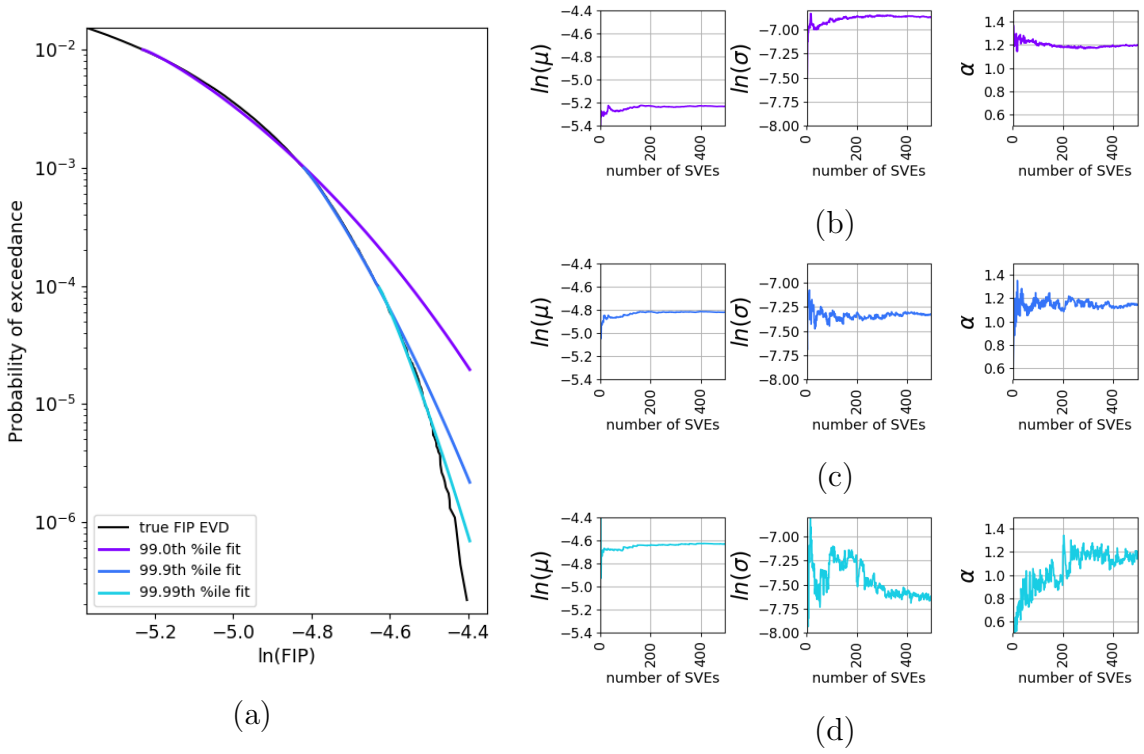

Figure 6.4: The FIP threshold and SVE convergence are studied for microstructure I with 500 SVEs: (a) The probability of exceedance is plotted for the true FIP EVD and for fits of the gamma distribution with three different thresholds. The convergence of the performance characteristics is plotted for (a) 99th, (b) 99.9th and (c) 99.99th percentile thresholds on the raw FIP response used to fit to the gamma distribution.

thresholds. For the 99th and 99.9th percentile thresholds the performance characteristics converge with the inclusion of at least 150 SVEs. For the 99.99th percentile fit, however, the performance characteristics do not converge until the inclusion of at least 400 SVEs. This analysis indicates that 150 SVEs and a 99.9th percentile threshold on the FIP distribution are most appropriate to represent the transition fatigue performance. Lastly, as α converges to around 1.15 in Figure 6.4c, this value will be held constant in the determination of μ and σ for future SVE ensembles. These results contrast with those of the HCF study, where 100 SVEs, a 99th percentile threshold and $\alpha = 0.85$ were selected using the same procedures [167]. Interestingly, the FIP threshold in this study exceeds that of the HCF study. This indicates that while FIP values are orders of magnitude greater in transition fatigue than in HCF, high quality fits to the gamma distribution still require extreme FIP values; in other words, fitting the tail of the overall PDF of FIPs is equally demanding in transition fatigue as in HCF. This was not fully expected prior to this study.

The minimum number of SVEs required to approximate the RVE (as identified from microstructure I) guides the number of CPFEM simulations that must be performed for the remaining microstructures. As discussed in Section 6.3, SVE subsets are identified from the original microstructure SVE ensembles to expand the number of data-points in the calibration of the linkage. If each subset contains 150 SVEs, the original microstructure SVE ensemble should contain significantly greater numbers to allow for diversity in the mean locations and variances of the subsets. Consequently, CPFEM simulations are performed for 300 SVEs for each of the remaining 11 microstructures.

6.4.4 Reduced-Dimensional Representation of Microstructures and Microstructure Subsets

Construction of a homogenization linkage to predict surrogate measures of transition fatigue performance requires the representation of microstructures by a small number of parameters. The first step in obtaining reduced-dimensional representations of the 12 α-titanium microstructures is the quantification of individual SVEs using 2-point spatial correlations (computed using Equation (6.2)). As in the preceding study [167], 41 GSH basis functions represent the functional dependence of the spatial correlations on crystal lattice orientation. This natural level of truncation in the GFS contains more than the 15 basis functions required to capture the functional dependence of elastic properties on orientation. While it may be desirable to explore representations with higher truncation levels, in this study it was decided that the improvements in representation fidelity would not outweigh the additional computational cost of computing the spatial statistics. Further details of the spatial statistics framework for polycrystals are presented in a prior study by Paulson et al. [76].

The GFS coefficients of Equation (6.2) are defined by 750,141 individual coefficients. Consequently, the application of PCA is an important step to obtain a tractable representation of the spatial statistics of each SVE. The PC directions are computed by performing PCA on all SVEs in the calibration ensemble (excluding SVEs associated with microstructure J). Once the PC directions are obtained, the PC scores of the SVEs may be computed. As the number of PC directions included in the representation of the spatial statistics increases, so does the cumulative explained variance (where the explained variance in one PC direction is the variance of the PC scores in the SVE ensemble along that direction). The cumulative explained variance succinctly demonstrates the compaction achieved by PCA; 72% and 98% of the variance is explained by the first 2 and 25 PC dimensions, respectively. This feature of PCA makes the visualization of data-points in two or three dimensions convenient. In

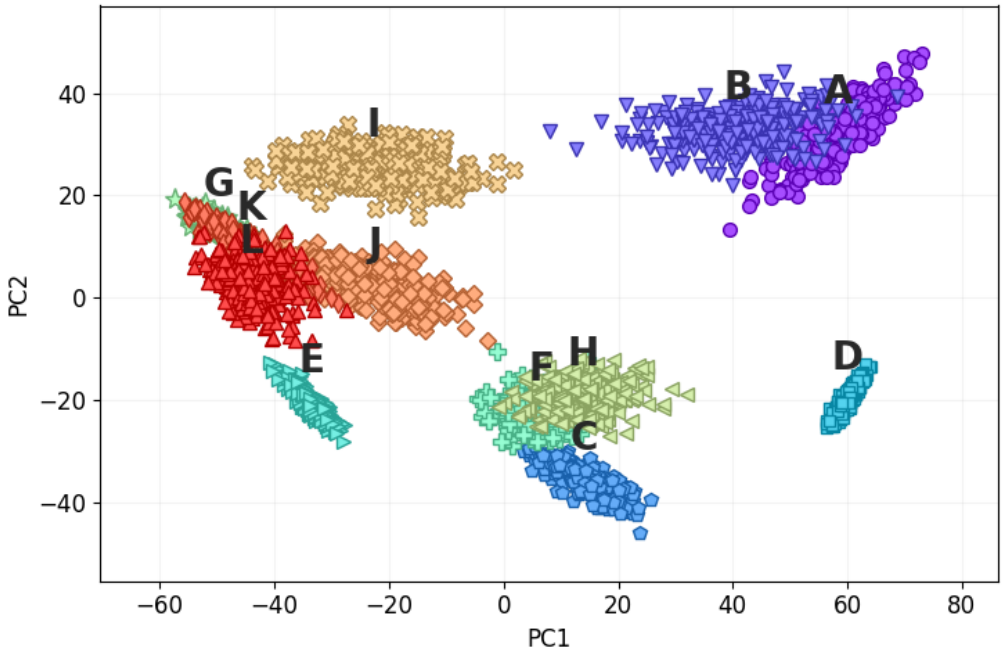

Figure 6.5: SVEs are plotted as points by their first two PC scores. The shape and color of each point indicates its associated microstructure.

Figure 6.5 all SVEs are plotted by their first two PC scores. In this figure, SVEs are well clustered by their associated microstructure. Significant spread is observed in the PC scores of SVEs associated with some microstructures. This variance is likely due to randomness inherent in the DREAM.3D algorithms. Furthermore, SVEs belonging to microstructures with similar texture features are nearby in PC space (for example microstructures A and B). The opposite is true for SVEs belonging to microstructures with very different textures (for example microstructures A and E). Readers who have examined the preceding work on HCF will notice significant differences in the PC maps. This is mainly due to the use of additional GSH basis functions in the representation of the spatial statistics with the GFS in this work (for the purposes of visualization).

At this stage, subsets are selected from the original SVE ensembles to expand the data available for calibration of the final linkage. First, the desired mean and variance (along the first three PC directions) of the target subset of SVEs are randomly

selected. These target statistics are generated so that there is a reasonable chance that the subset selected from an original SVE ensemble (representing 1 of the 12 microstructures) matches the statistics. Next, an iterative algorithm is employed to identify the best set of SVEs to match the target statistics. In the initialization stage, all SVEs associated with the microstructure under consideration are included in the subset. Each iteration, the multivariate PDF of the current subset of SVEs (as computed using kernel density estimation [165, 166]) is compared against the PDF of the multivariate Gaussian distribution defined by the target mean location and variances. The SVE in the subset where the actual probability density most exceeds the target probability density is removed. Iterations are continued until only 150 SVEs remain in the subset (this was identified in Section 6.4.3 as the number of SVEs needed to obtain a robust quantification of the FIP distribution for each microstructure). A total of 20 subsets are selected from each calibration microstructure for a total of 220 subsets. Further details of this approach were provided in a prior study [167].

Finally, each SVE ensemble (representing a microstructure or microstructure subset) may be characterized by the mean and total variance its members' PC scores. Twenty-five PC dimensions are considered in the calculation of the mean location. This truncation is justified because over 98% of the cumulative explained variance is captured by this set of PC dimensions. The total variance is calculated with all available PC dimensions because it always results in a scalar value (the use of more PC dimensions does not increase the dimensionality of the measure).

6.4.5 Calibration of the S-P Linkage

Given the reduced-dimensional representations of 220 SVE subsets and their associated performance characteristics, the physics-capturing coefficients of Equation (6.5) may be obtained through a calibration procedure. First, the set of features of interest (each denoted $\tilde{\alpha}_l^k$) are identified. This set may include multiplicative combinations of

the mean PC locations and total variance, resulting in a huge set of potential features. As described in Section 6.4.4, only 25 PC dimensions are employed to represent the mean location of the SVE ensemble. Furthermore, only 2nd order polynomial features are allowed, as it was shown in the preceding work that such features provide good descriptive capability with lower risk of overfitting the calibration data [167]. To further reduce this set, Pearson correlations [82] are employed to identify which specific features are most likely to contribute to the predictive capability of the resultant linkage.

Table 6.1 presents the top ten features and their Pearson correlation scores for μ and σ. Note that certain features are highly correlated with both performance characteristics (specifically $\overline{PC}_1$ and $\overline{PC}_1 \cdot VAR_{tot}$), although the number of common features is fewer than in the preceding work, where four of the top ten features were common [167]. In that study, more features were common, as was reflected in the high Pearson correlation between μ and σ ($R = 0.941$). Fewer highly correlated features are common in the current study on transition fatigue, because the performance characteristics are only weakly correlated ($R = 0.465$). Also, note that none of the top-ranked features are common between the transition fatigue and the HCF studies. This is likely due to the different physics governing HCF and transition fatigue, as well as the different boundary conditions used in the two studies. That said, $\overline{PC}_1$, $\overline{PC}_6$, $\overline{PC}_7$ and VAR_{tot} show prominently in the top features in both studies. Most importantly, similarly complex features are prominent in both studies, indicating that both require sophisticated functions to fit to the fatigue performance measures.

Ranking features by their Pearson correlations enables us to precisely select a small subset likely to provide good predictive capability. The number of features included in the final linkage is identified through a comparison of training and cross-validation errors. Training error is computed for linkages calibrated with the whole set of SVE ensembles (associated with the calibration set). Cross-validation describes

Table 6.1: The top ten features for performance characteristics μ and σ are ranked by their Pearson correlations. The overbar indicates that the mean is taken over the specified PC dimension for each SVE ensemble.

Feature Ranking	μ	Pearson Correlation	σ	Pearson Correlation
1	$\overline{PC}_1$	-0.892	$\overline{PC}_1 \cdot \overline{PC}_8$	-0.762
2	$\overline{PC}_1 \cdot VAR_{tot}$	-0.890	$\overline{PC}_2 \cdot \overline{PC}_3$	-0.648
3	$\overline{PC}_6 \cdot \overline{PC}_8$	0.810	$\overline{PC}_1$	-0.630
4	$\overline{PC}_8^{\,2}$	-0.727	$\overline{PC}_1 \cdot \overline{PC}_6$	0.614
5	$\overline{PC}_3 \cdot \overline{PC}_4$	-0.621	$\overline{PC}_1 \cdot VAR_{tot}$	-0.588
6	$\overline{PC}_2^{\,2}$	-0.584	$\overline{PC}_4^{\,2}$	-0.541
7	$\overline{PC}_2 \cdot \overline{PC}_3$	-0.566	$\overline{PC}_3 \cdot \overline{PC}_4$	-0.508
8	$\overline{PC}_6 \cdot \overline{PC}_{10}$	0.541	$\overline{PC}_1 \cdot \overline{PC}_{10}$	-0.503
9	$\overline{PC}_8 \cdot \overline{PC}_{15}$	-0.540	$\overline{PC}_2$	0.494
10	$\overline{PC}_7 \cdot \overline{PC}_8$	-0.529	$\overline{PC}_{20}^{\,2}$	-0.492

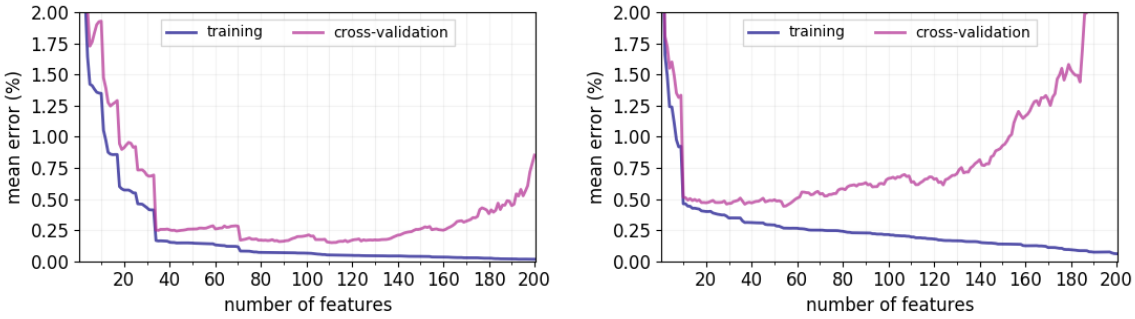

(a) (b)

Figure 6.6: Training and cross-validation errors are plotted for increasing numbers of features for (a) μ and (b) σ.

the technique of removing data-points from the calibration set and reserving them for evaluating the resultant linkage. The cross-validation strategy of the preceding study is directly employed in this work [167]. Cross-validation is performed on 22 sets of 10 SVE subsets, where each set contains half of the subsets associated with each of the 11 original microstructures. Both errors are computed by evaluating the difference between the predicted and simulated performance characteristics for the SVE ensembles of interest.

Figure 6.6 presents training and cross-validation errors for linkages constructed

with increasing numbers of features. While the training error continuously decreases with increasing numbers of features, the cross-validation error first decreases and then increases. The divergence of the cross-validation error from the training error indicates sensitivity of the linkage to the specific data-points included in the calibration set for the linkage. Consequently, linkages should be selected with the number of features at the point where this divergence becomes evident. Note that the presented training and cross-validation error curves are similar in shape and magnitude to the errors from previous linkages that characterized the HCF performance [167]. This indicates that the MKS framework has successfully captured the physics of the transition fatigue regime where plastic strains are on the same order of magnitude as elastic strains and where stress redistribution is significant. In this study, the top 34 and 10 features are employed in the final linkages for μ and σ, respectively.

6.4.6 Validation of Protocols

After the calibration of the physics-capturing coefficients with the full set of 220 SVE subsets, Equation (6.5) may be used to predict the performance characteristics of the SVE ensembles associated with the original 12 microstructures (including microstructure J). Then, employing Equation (6.1), the FIP EVDs for these microstructures can be constructed. The results of this effort are presented in Figure 6.7, where the FIP EVDs resulting from CPFEM simulations and the MKS homogenization protocols are compared for microstructures A through L. It is acknowledged that the predicted FIP EVDs are different from the CPFEM derived ones in some regards. Most notably, the predicted EVDs display a less pronounced curvature in the probability of exceedance plot. This results in slight differences in the rank-ordering at low probabilities of exceedance (see microstructures A and B). Even so, this comparison demonstrates the success of these protocols in rank-ordering the transition fatigue resistance of a diverse set of polycrystalline microstructures (including the validation microstructure

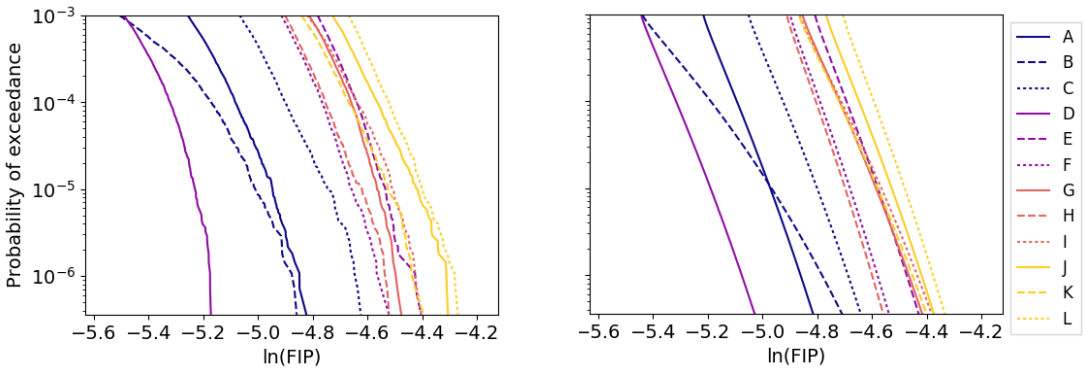

(a) (b)

Figure 6.7: FIP EVDs as obtained via (a) CPFEM simulations and (b) the MKS approach for the 12 α-titanium microstructures (labeled A through L).

whose SVEs were not included in the calibration sets).

The error levels for the transition fatigue linkages developed here are observed to be very comparable to those from the HCF linkages obtained in the earlier study [167]. Indeed, this is somewhat surprising because we anticipated that the higher levels of inelastic deformation and stress redistribution in transition fatigue (as compared to HCF) would demand more complex linkages (with more terms and higher powers of the polynomials). The present study provides a strong testament to the power of GSH in capturing the 2-point statistics and the PCA in providing a high-value, low-dimensional representation of these correlations. We attribute the success of the protocols in delivering high-value, low-dimensional structure-property linkages in transition fatigue to these two key ingredients of our protocol.

Furthermore, the computational advantages of the MKS protocols versus CPFEM in rank-ordering fatigue resistance is even more dramatic for transition fatigue than for HCF. Once the one time cost of calibrating the homogenization relationship was performed (utilizing CPFEM results for 300 SVEs from each of the 11 calibration microstructures), evaluation of the FIP EVD for the validation microstructure was performed in less than nine minutes on a single processor (including the computation of the spatial statistics for 300 SVEs and the evaluation of Equation (6.5)). In

contrast, a direct application of the traditional brute force CPFEM approach for the validation microstructure would require over 3000 hours (or roughly 5 months) of CPU time. This represents more than a 22,000 times reduction in CPU time versus the traditional approach. A similar speed-up is expected for any other microstructure (e.g., texture variant for the same material composition) in the materials system that does not represent a dramatic extrapolation beyond the microstructures employed to calibrate the linkage. Furthermore, the computational speed-up is greater than the 3000 times reduction seen in the preceding study [167]. This apparent improvement is due to the increased computational cost of modeling the larger cyclic plastic strains through CPFEM simulations. In this work, each CPFEM simulation required 3 hours on four processors, as compared to the 45 minutes required in the HCF regime. Comparing the computational expense between the two studies further emphasizes the benefits of reduced-order protocols for the exploration of the transition fatigue performance of polycrystalline microstructures.

6.5 Conclusions

In this study, an MKS homogenization linkage is developed to rank-order the transition fatigue performance of 12 distinct α-titanium microstructures. The success of these protocols (originally developed for the HCF regime) in transition fatigue underscore their efficacy and versatility in addressing many failure-related microscale phenomena important in materials design. In particular, it is seen that the GSH representation of the 2-point statistics and their low-dimensional representation using PCA are the main keys to success of such efforts. More specifically, simulations in the transition fatigue regime are computationally expensive due to significant levels of heterogenous plastic strains in addition to stress- and strain-redistribution. Once calibrated with the results of CPFEM simulations for a set of calibration microstructures, the linkages developed in this work provide more than a 22,000 times computational

speed-up versus traditional CPFEM approaches in the evaluation of the transition fatigue performance of new microstructures with the same material composition. Furthermore, these linkages take reduced-order forms well suited to materials exploration efforts. This study demonstrates the flexibility of the MKS framework for modeling microstructure-sensitive, extreme-value phenomena such as fatigue.

Acknowledgments

This work was supported by the National Science Foundation under Grant No. CMMI-1333083. Any opinions, findings, and conclusions or recommendations expressed in this material are those of the authors and do not necessarily reflect the views of the National Science Foundation.

REFERENCES

[1] *Materials Genome Initiative for Global Competitiveness*. Tech. rep. National Science and Technology Council, 2011.

[2] H Moulinec and P Suquet. "A fast numerical method for computing the linear and nonlinear mechanical properties of composites". In: *Comptes rendus l'Académie des Sci. Série II, Mécanique, Phys. Chim. Astron.* 318.11 (1994), pp. 1417–1423.

[3] R A Lebensohn, A K Kanjarla, and P Eisenlohr. "An elasto-viscoplastic formulation based on fast Fourier transforms for the prediction of micromechanical fields in polycrystalline materials". In: *Int J Plast* 32 (2012), pp. 59–69. DOI: 10.1016/j.ijplas.2011.12.005. URL: http://dx.doi.org/10.1016/j.ijplas.2011.12.005.

[4] S.R. Kalidindi, C.A. Bronkhorst, and L. Anand. "Crystallographic texture evolution in bulk deformation processing of FCC metals". In: *J. Mech. Phys. Solids* 40.3 (Jan. 1992), pp. 537–569. ISSN: 00225096. DOI: 10.1016/0022-5096(92)80003-9. URL: http://linkinghub.elsevier.com/retrieve/pii/0022509692800039.

[5] Franz Roters, Philip Eisenlohr, Thomas R Bieler, and Dierk Raabe. *Crystal plasticity finite element methods: in materials science and engineering*. John Wiley & Sons, 2011.

[6] B.D. Smith, D. Shih, and D.L. McDowell. "Cyclic Plasticity Experiments and Polycrystal Plasticity Modeling of Three Distinct Ti Alloy Microstructures". In: *Int. J. Plast.* (2013). ISSN: 07496419. DOI: 10.1016/j.ijplas.2013.10.004.

[7] E O Hall. "The Deformation and Ageing of Mild Steel: III Discussion of Results". In: *Proc. Phys. Soc. Sect. B* 64.9 (1951), p. 747.

[8] N.J. Petch. "The cleavage strength of polycrystals". In: *J. Iron Steel Inst.* 174 (1953), pp. 25–28.

[9] J.D. Eshelby. "The Determination of Elastic Field of an Ellipsoidal Inclusion, and Related Problems". In: *Proc. R. Soc. Lond. A. Math. Phys. Sci.* A241 (1957), pp. 376–396.

[10] Ekkehart Kröner. "Berechnung der elastischen Konstanten des Vielkristalls aus den Konstanten des Einkristalls". In: *Zeitschrift für Phys.* 151.4 (1958), pp. 504–518. ISSN: 0044-3328. DOI: 10.1007/BF01337948. URL: http://dx.doi.org/10.1007/BF01337948.

[11] R.A. Lebensohn and C.N. Tomé. "A self-consistent anisotropic approach for the simulation of plastic deformation and texture development of polycrystals: Application to zirconium alloys". In: *Acta Metall. Mater.* 41.9 (1993), pp. 2611–2624. ISSN: 09567151. DOI: 10.1016/0956-7151(93)90130-K.

[12] H. Wang, P.D. Wu, C.N. Tomé, and Y. Huang. "A finite strain elastic–viscoplastic self-consistent model for polycrystalline materials". In: *J. Mech. Phys. Solids* 58.4 (2010), pp. 594–612. ISSN: 00225096. DOI: 10.1016/j.jmps.2010.01.004.

[13] Surya R Kalidindi, Stephen R Niezgoda, Giacomo Landi, Shraddha Vachhani, and Tony Fast. "A novel framework for building materials knowledge systems". In: *Comput. Mater. Contin.* 17.2 (2010), pp. 103–125.

[14] Giacomo Landi, Stephen R. Niezgoda, and Surya R. Kalidindi. "Multi-scale modeling of elastic response of three-dimensional voxel-based microstructure datasets using novel DFT-based knowledge systems". In: *Acta Mater.* 58.7 (2010), pp. 2716–2725. ISSN: 13596454. DOI: 10.1016/j.actamat.2010.01.007.

[15] Stephen R. Niezgoda, Yuksel C. Yabansu, and Surya R. Kalidindi. "Understanding and visualizing microstructure and microstructure variance as a stochastic process". In: *Acta Mater.* 59.16 (2011), pp. 6387–6400. ISSN: 13596454. DOI: 10.1016/j.actamat.2011.06.051.

[16] Tony Fast, Stephen R Niezgoda, and Surya R Kalidindi. "A new framework for computationally efficient structure–structure evolution linkages to facilitate high-fidelity scale bridging in multi-scale materials models". In: *Acta Mater.* 59.2 (2011), pp. 699–707. ISSN: 1359-6454. DOI: http://dx.doi.org/10.1016/j.actamat.2010.10.008. URL: http://www.sciencedirect.com/science/article/pii/S1359645410006701.

[17] T. Fast and S.R. Kalidindi. "Formulation and calibration of higher-order elastic localization relationships using the MKS approach". In: *Acta Mater.* 59.11 (2011), pp. 4595–4605. DOI: 10.1016/j.actamat.2011.04.005. URL: https://www.scopus.com/inward/record.uri?eid=2-s2.0-79956011479%7B%5C&%7DpartnerID=40%7B%5C&%7Dmd5=.

[18] Surya R Kalidindi, Stephen R Niezgoda, and Ayman A Salem. "Microstructure informatics using higher-order statistics and efficient data-mining protocols". In: *JOM* 63.4 (2011), pp. 34–41. ISSN: 1543-1851. DOI: 10.1007/s11837-011-0057-7. URL: http://dx.doi.org/10.1007/s11837-011-0057-7.

[19] Brent L. Adams, Surya R. Kalidindi, and David T. Fullwood. *Microstructure Sensitive Design for Performance Optimization*. Butterworth-Heinemann, 2012, p. 425. ISBN: 9780123969897.

[20] Stephen R Niezgoda, Anand K Kanjarla, and Surya R Kalidindi. "Novel microstructure quantification framework for databasing, visualization, and analysis of microstructure data". In: *Integr. Mater. Manuf. Innov.* 2.3 (2013), pp. 1–27. ISSN: 2193-9772. DOI: 10.1186/2193-9772-2-3. URL: http://dx.doi.org/10.1186/2193-9772-2-3.

[21] Yuksel C. Yabansu, Dipen K. Patel, and Surya R. Kalidindi. "Calibrated localization relationships for elastic response of polycrystalline aggregates". In: *Acta Mater.* 81 (2014), pp. 151–160. ISSN: 13596454. DOI: 10.1016/j.actamat.2014.08.022.

[22] A. Çeçen, T. Fast, E.C. Kumbur, and S.R. Kalidindi. "A data-driven approach to establishing microstructure–property relationships in porous transport layers of polymer electrolyte fuel cells". In: *J. Power Sources* 245.1 (2014), pp. 144–153. ISSN: 03787753. DOI: 10.1016/j.jpowsour.2013.06.100.

[23] Yuksel C. Yabansu and Surya R. Kalidindi. "Representation and calibration of elastic localization kernels for a broad class of cubic polycrystals". In: *Acta Mater.* 94 (2015), pp. 26–35. DOI: 10.1016/j.actamat.2015.04.049.

[24] Akash Gupta, Ahmet Cecen, Sharad Goyal, Amarendra K. Singh, and Surya R. Kalidindi. "Structure-property linkages using a data science approach: Application to a non-metallic inclusion/steel composite system". In: *Acta Mater.* 91 (2015), pp. 239–254. ISSN: 13596454. DOI: 10.1016/j.actamat.2015.02.045.

[25] Surya R. Kalidindi. *Hierarchical Materials Informatics: Novel Analytics for Materials Data*. Butterworth-Heinemann, 2015, p. 230. ISBN: 9780124103948.

[26] David B Brough, Daniel Wheeler, James A Warren, and Surya R Kalidindi. "Microstructure-based knowledge systems for capturing process-structure evolution linkages". In: *Curr. Opin. Solid State Mater. Sci.* (2016). ISSN: 1359-0286. DOI: http://dx.doi.org/10.1016/j.cossms.2016.05.002. URL: http://www.sciencedirect.com/science/article/pii/S1359028616300298.

[27] Ali Khosravani, Ahmet Cecen, and Surya R Kalidindi. "Development of high throughput assays for establishing process-structure-property linkages in multiphase polycrystalline metals: Application to dual-phase steels". In: *Acta Mater.* 123 (2017), pp. 55–69. ISSN: 1359-6454. DOI: http://dx.doi.org/10.1016/j.actamat.2016.10.033. URL: http://www.sciencedirect.com/science/article/pii/S135964541630800X.

[28] David B Brough, Abhiram Kannan, Benjamin Haaland, David G Bucknall, and Surya R Kalidindi. "Extraction of Process-Structure Evolution Linkages from X-ray Scattering Measurements Using Dimensionality Reduction and Time Series Analysis". In: *Integr. Mater. Manuf. Innov.* (2017), pp. 1–13. ISSN: 2193-9772. DOI: 10.1007/s40192-017-0093-4. URL: http://dx.doi.org/10.1007/s40192-017-0093-4.

[29] Evdokia Popova, Theron M. Rodgers, Xinyi Gong, Ahmet Cecen, Jonathan D. Madison, and Surya R. Kalidindi. "Process-Structure Linkages Using a Data Science Approach: Application to Simulated Additive Manufacturing Data". In: *Integr. Mater. Manuf. Innov.* 6.1 (2017), pp. 54–68. ISSN: 2193-9772. DOI: 10.1007/s40192-017-0088-1. URL: http://dx.doi.org/10.1007/s40192-017-0088-1.

[30] Yuksel C Yabansu, Philipp Steinmetz, Johannes Hötzer, Surya R Kalidindi, and Britta Nestler. "Extraction of reduced-order process-structure linkages from phase-field simulations". In: *Acta Mater.* 124 (2017), pp. 182–194. ISSN: 1359-6454. DOI: http://dx.doi.org/10.1016/j.actamat.2016.10.071. URL: http://www.sciencedirect.com/science/article/pii/S1359645416308485.

[31] William Fuller Brown. "Solid Mixture Permittivities". In: *J. Chem. Phys.* 23.8 (1955), p. 1514. ISSN: 00219606. DOI: 10.1063/1.1742339. URL: http://scitation.aip.org/content/aip/journal/jcp/23/8/10.1063/1.1742339.

[32] Mark J. Beran. *Statistical Continuum Theories*. 1968, p. 424.

[33] E. Kröner. "Bounds for effective elastic moduli of disordered materials". In: *J. Mech. Phys. Solids* 25.2 (1977), pp. 137–155. ISSN: 00225096. DOI: 10.1016/0022-5096(77)90009-6.

[34] S. Torquato and G. Stell. "Microstructure of two-phase random media. I. The n-point probability functions". In: *J. Chem. Phys.* 77.4 (1982), p. 2071.

[35] Brent L. Adams, Gilles R. Canova, and Alain Molinari. "A statistical formulation of viscoplastic behavior in heterogeneous polycrystals". In: *Textures Microstruct.* 11 (1989), pp. 57–71.

[36] Brent L. Adams, Xiang (Carl) Gao, and Surya R. Kalidindi. "Finite approximations to the second-order properties closure in single phase polycrystals". In: *Acta Mater.* 53.13 (2005), pp. 3563–3577. ISSN: 13596454. DOI: 10.1016/j.actamat.2005.03.052.

[37] David T. Fullwood, Stephen R. Niezgoda, and Surya R. Kalidindi. "Microstructure reconstructions from 2-point statistics using phase-recovery algorithms". In: *Acta Mater.* 56.5 (2008), pp. 942–948. ISSN: 13596454. DOI: 10.1016/j.actamat.2007.10.044.

[38] Karl Pearson. "On lines and planes of closest fit to systems of points in space". In: *Philos. Mag.* 2 (1901), pp. 559–572.

[39] X. Gao, C. P. Przybyla, and B. L. Adams. "Methodology for recovering and analyzing two-point pair correlation functions in polycrystalline materials". In: *Metall. Mater. Trans. A Phys. Metall. Mater. Sci.* 37.8 (2006), pp. 2379–2387. ISSN: 10735623. DOI: 10.1007/BF02586212. URL: http://dx.doi.org/10.1007/BF02586212.

[40] David T. Fullwood, Brent L. Adams, and Surya R. Kalidindi. "A strong contrast homogenization formulation for multi-phase anisotropic materials". In: *J. Mech. Phys. Solids* 56.6 (2008), pp. 2287–2297. ISSN: 00225096. DOI: 10.1016/j.jmps.2008.01.003.

[41] H.-J. Bunge. *Texture Analysis in Materials Science*. London, Boston, Sydney, Wellington, Durban, Toronto: Butterworths, 1982, p. 592. ISBN: 0-408-10642-5.

[42] B.L. Adams, A. Henrie, B. Henrie, M. Lyon, S.R. Kalidindi, and H. Garmestani. "Microstructure-sensitive design of a compliant beam". In: *J. Mech. Phys. Solids* 49.8 (2001), pp. 1639–1663. ISSN: 00225096. DOI: 10.1016/S0022-5096(01)00016-3.

[43] Gwénaëlle Proust and Surya R. Kalidindi. "Procedures for construction of anisotropic elastic–plastic property closures for face-centered cubic polycrystals using first-order bounding relations". In: *J. Mech. Phys. Solids* 54.8 (2006), pp. 1744–1762. ISSN: 00225096. DOI: 10.1016/j.jmps.2006.01.010.

[44] Marko Knezevic and Surya R. Kalidindi. "Fast computation of first-order elastic–plastic closures for polycrystalline cubic-orthorhombic microstructures". In: *Comput. Mater. Sci.* 39.3 (2007), pp. 643–648. ISSN: 09270256. DOI: 10.1016/j.commatsci.2006.08.025.

[45] Akhtar S Khan, Rehan Kazmi, and Babak Farrokh. "Multiaxial and nonproportional loading responses, anisotropy and modeling of Ti–6Al–4V titanium alloy over wide ranges of strain rates and temperatures". In: *Int. J. Plast.* 23.6 (2007), pp. 931–950. ISSN: 0749-6419. DOI: http://dx.doi.org/10.1016/j.ijplas.2006.08.006. URL: http://www.sciencedirect.com/science/article/pii/S0749641906001264.

[46] Michael A. Groeber and Michael A. Jackson. "DREAM.3D: A Digital Representation Environment for the Analysis of Microstructure in 3D". In: *Integr. Mater. Manuf. Innov.* 3.1 (2014), p. 5. ISSN: 2193-9772. DOI: 10.1186/2193-9772-3-5. URL: http://www.immijournal.com/content/3/1/5.

[47] C.-H. Goh, J.M. Wallace, R.W. Neu, and D.L. McDowell. "Polycrystal plasticity simulations of fretting fatigue". In: *Int. J. Fatigue* 23 (2001), pp. 423–435. ISSN: 01421123. DOI: 10.1016/S0142-1123(01)00150-5.

[48] J. R. Mayeur and D. L. McDowell. "A three-dimensional crystal plasticity model for duplex Ti-6Al-4V". In: *Int. J. Plast.* 23.9 (2007), pp. 1457–1485. ISSN: 07496419. DOI: 10.1016/j.ijplas.2006.11.006.

[49] M. Zhang, J. Zhang, and D.L. McDowell. "Microstructure-based crystal plasticity modeling of cyclic deformation of Ti–6Al–4V". In: *Int. J. Plast.* 23.8 (2007), pp. 1328–1348. ISSN: 07496419. DOI: 10.1016/j.ijplas.2006.11.009.

[50] Jason R. Mayeur, David L. McDowell, and Richard W. Neu. "Crystal plasticity simulations of fretting of Ti-6Al-4V in partial slip regime considering effects of texture". In: *Comput. Mater. Sci.* 41.3 (2008), pp. 356–365. ISSN: 09270256. DOI: 10.1016/j.commatsci.2007.04.020.

[51] F. Bridier, P. Villechaise, and J. Mendez. "Slip and fatigue crack formation processes in an α/β titanium alloy in relation to crystallographic texture on different scales". In: *Acta Mater.* 56.15 (2008), pp. 3951–3962. ISSN: 13596454. DOI: 10.1016/j.actamat.2008.04.036.

[52] David T. Fullwood, Stephen R. Niezgoda, Brent L. Adams, and Surya R. Kalidindi. "Microstructure sensitive design for performance optimization". In: *Prog. Mater. Sci.* 55.6 (2010), pp. 477–562. ISSN: 00796425. DOI: 10.1016/j.pmatsci.2009.08.002.

[53] Toshio Mura. *Micromechanics of defects in solids*. Martinus Nijhoff Publishers, 1982. ISBN: 978-94-011-9306-1. DOI: 10.1007/978-94-011-9306-1.

[54] Ahmet Çeçen, Tony Fast, and Surya R Kalidindi. "Versatile algorithms for the computation of 2-point spatial correlations in quantifying material structure". In: *Integr. Mater. Manuf. Innov.* 5.1 (2016), pp. 1–15. ISSN: 2193-9772. DOI: 10.1186/s40192-015-0044-x. URL: http://dx.doi.org/10.1186/s40192-015-0044-x.

[55] H. Garmestani, S. Lin, and B.L. Adams. "Statistical continuum theory for inelastic behavior of a two-phase medium". In: *Int. J. Plast.* 14.8 (1998), pp. 719–731. ISSN: 07496419. DOI: 10.1016/S0749-6419(98)00019-9.

[56] H. Garmestani, S. Lin, B.L. Adams, and S. Ahzi. "Statistical continuum theory for large plastic deformation of polycrystalline materials". In: *J. Mech. Phys. Solids* 49.3 (2001), pp. 589–607. ISSN: 00225096. DOI: 10.1016/S0022-5096(00)00040-5.

[57] Graeme W. Milton. *The Theory of Composites*. Cambridge: Cambridge University Press, 2002, p. 748.

[58] David L McDowell. "Simulation-based strategies for microstructure-sensitive fatigue modeling". In: *Mater. Sci. Eng. A* 468–470 (2007), pp. 4–14. ISSN: 0921-5093. DOI: http://dx.doi.org/10.1016/j.msea.2006.08.129. URL: http://www.sciencedirect.com/science/article/pii/S092150930700295X.

[59] Ted L. Anderson. *Fracture mechanics: fundamentals and applications*. CRC press, 2005.

[60] Darrell F Socie and G B Marquis. "Multiaxial Fatigue". In: *Soc. Automot. Enginneers, Inc. Warrendale* (2001).

[61] David L McDowell. "Basic issues in the mechanics of high cycle metal fatigue". In: *Int. J. Fract.* 80.2 (1996), p. 103. ISSN: 1573-2673. DOI: 10.1007/BF00012666. URL: http://dx.doi.org/10.1007/BF00012666.

[62] D.L. McDowell and F.P.E. Dunne. "Microstructure-sensitive computational modeling of fatigue crack formation". In: *Int. J. Fatigue* 32.9 (2010), pp. 1521–1542. ISSN: 0142-1123. DOI: http://dx.doi.org/10.1016/j.ijfatigue.2010.01.003. URL: http://www.sciencedirect.com/science/article/pii/S0142112310000162.

[63] Ali Fatemi and Peter Kurath. "Multiaxial fatigue life predictions under the influence of mean-stresses". In: *J. Eng. Mater. Technol.* 110.4 (1988), pp. 380–388.

[64] Ali Fatemi and Nima Shamsaei. "Multiaxial fatigue: An overview and some approximation models for life estimation". In: *Int. J. Fatigue* 33.8 (2011), pp. 948–958. ISSN: 0142-1123. DOI: http://dx.doi.org/10.1016/j.ijfatigue.2011.01.003. URL: http://www.sciencedirect.com/science/article/pii/S0142112311000053.

[65] Gustavo M Castelluccio and David L McDowell. "Assessment of small fatigue crack growth driving forces in single crystals with and without slip bands". In: *Int. J. Fract.* 176.1 (2012), pp. 49–64. ISSN: 1573-2673. DOI: 10.1007/s10704-012-9726-y. URL: http://dx.doi.org/10.1007/s10704-012-9726-y.

[66] Craig P. Przybyla and David L. McDowell. "Microstructure-sensitive extreme value probabilities for high cycle fatigue of Ni-base superalloy IN100". In: *Int. J. Plast.* 26.3 (2010), pp. 372–394. ISSN: 07496419. DOI: 10.1016/j.ijplas.2009.08.001.

[67] Craig P Przybyla and David L McDowell. "Simulated microstructure-sensitive extreme value probabilities for high cycle fatigue of duplex Ti–6Al–4V". In: *Int. J. Plast.* 27.12 (2011), pp. 1871–1895. ISSN: 0749-6419. DOI: http://dx.doi.org/10.1016/j.ijplas.2011.01.006. URL: http://www.sciencedirect.com/science/article/pii/S0749641911000155.

[68] Paul Calvin Kern. "Improvements to the computational pipeline in crystal plasticity estimates of high cycle fatigue of microstructures". MA thesis. Georgia Institute of Technology, 2016, p. 181.

[69] Benjamin D Smith, Donald S Shih, and David L McDowell. "Fatigue hot spot simulation for two Widmanstätten titanium microstructures". In: *Int. J. Fatigue* 92, Part 1 (2016), pp. 116–129. ISSN: 0142-1123. DOI: http://dx.doi.org/10.1016/j.ijfatigue.2016.05.002. URL: //www.sciencedirect.com/science/article/pii/S0142112316300883.

[70] M. Peters, A. Gysler, and G. Lütjering. "Influence of texture on fatigue properties of Ti-6Al-4V". In: *Metall. Trans. A* 15.8 (1984), pp. 1597–1605. ISSN: 1543-1940. DOI: 10.1007/BF02657799. URL: http://dx.doi.org/10.1007/BF02657799.

[71] Y N Wang and J C Huang. "Texture analysis in hexagonal materials". In: *Mater. Chem. Phys.* 81.1 (2003), pp. 11–26. ISSN: 0254-0584. DOI: http://dx.doi.org/10.1016/S0254-0584(03)00168-8. URL: http://www.sciencedirect.com/science/article/pii/S0254058403001688.

[72] G. Lütjering and J.C. Williams. *Titanium*. Engineering Materials and Processes. Springer Berlin Heidelberg, 2007. ISBN: 9783540730361. URL: https://books.google.com/books?id=41EqJFxjA4wC.

[73] Desmond Tromans. "Elastic anisotropy of HCP metal crystals and polycrystals". In: *Int. J. Res. Rev. Appl. Sci* 6.4 (2011), pp. 462–483. URL: http://www.arpapress.com/volumes/vol6issue4/ijrras%7B%5C_%7D6%7B%5C_%7D4%7B%5C_%7D14.pdf.

[74] M.W. Priddy, N.H. Paulson, S.R. Kalidindi, and D.L. McDowell. "Strategies for rapid parametric assessment of microstructure-sensitive fatigue for HCP systems". In: *Prep.* (2017).

[75] M.W. Priddy. "Exploration of forward and inverse protocols for property optimization of Ti-6Al-4V". PhD thesis. Georgia Institute of Technology, 2016.

[76] Noah H Paulson, Matthew W Priddy, David L McDowell, and Surya R Kalidindi. "Reduced-order structure-property linkages for polycrystalline microstructures based on 2-point statistics". In: *Acta Mater.* 129 (2017), pp. 428–438. DOI: http://dx.doi.org/10.1016/j.actamat.2017.03.009.

[77] Hibbett, Karlsson, and Sorensen. *ABAQUS/standard: User's Manual*. 1st ed. Hibbitt, Karlsson & Sorensen, 1998.

[78] X. Wu, G. Proust, M. Knezevic, and S. R. Kalidindi. "Elastic-plastic property closures for hexagonal close-packed polycrystalline metals using first-order bounding theories". In: *Acta Mater.* 55.8 (2007), pp. 2729–2737. ISSN: 13596454. DOI: 10.1016/j.actamat.2006.12.010. URL: http://www.sciencedirect.com/science/article/pii/S1359645407000171.

[79] Tony Fast, Marko Knezevic, and Surya R. Kalidindi. "Application of microstructure sensitive design to structural components produced from hexagonal polycrystalline metals". In: *Comput. Mater. Sci.* 43.2 (2008), pp. 374–383. ISSN: 09270256. DOI: 10.1016/j.commatsci.2007.12.002.

[80] T. Kanit, S. Forest, I. Galliet, V. Mounoury, and D. Jeulin. "Determination of the size of the representative volume element for random composites: statistical and numerical approach". In: *Int. J. Solids Struct.* 40.13 (2003), pp. 3647–3679. ISSN: 00207683. DOI: 10.1016/S0020-7683(03)00143-4.

[81] Robert V. Hogg and Allen T. Craig. "Some Special Distributions". In: *Introd. to Math. Stat.* 4th. New York: Macmillan Publishing Co., Inc., 1979. Chap. 3, pp. 103–109.

[82] Christian Heumann, Michael Schomaker, and Shalabh. "Association of Two Variables". In: *Introd. to Stat. Data Anal.* 2017. Chap. 4, pp. 67–94.

[83] D.T. Raske and JoDean Morrow. "Mechanics of materials in low cycle fatigue testing". In: *Man. Low Cycle Fatigue Test.* American Society for Testing and Materials, 1969, pp. 1–26.

[84] Hongyi Xu, Yang Li, Catherine Brinson, and Wei Chen. "A descriptor-based design methodology for developing heterogeneous microstructural materials system". In: *J. Mech. Des.* 136.5 (2014), pp. 206–216.

[85] Jitesh H. Panchal, Surya R. Kalidindi, and David L. McDowell. "Key computational modeling issues in Integrated Computational Materials Engineering". In: *Comput. Des.* 45.1 (2013), pp. 4–25. ISSN: 00104485. DOI: 10.1016/j.cad.2012.06.006.

[86] D L McDowell and D Backman. "Simulation-Assisted Design and Accelerated Insertion of Materials". In: *Comput. Methods Microstruct. Relationships*. Ed. by Somnath Ghosh and Dennis Dimiduk. Boston, MA: Springer US, 2011, pp. 617–647. ISBN: 978-1-4419-0643-4. DOI: 10.1007/978-1-4419-0643-4_17. URL: http://dx.doi.org/10.1007/978-1-4419-0643-4%7B%5C_%7D17.

[87] David L McDowell, Jitesh Panchal, Hae-Jin Choi, Carolyn Seepersad, Janet Allen, and Farrokh Mistree. *Integrated design of multiscale, multifunctional materials and products*. Butterworth-Heinemann, 2009.

[88] Veera Sundararaghavan and Nicholas Zabaras. "A statistical learning approach for the design of polycrystalline materials". In: *Stat. Anal. Data Min.* 1.5 (2009), pp. 306–321.

[89] Carolyn Connor Seepersad, Benjamin Dempsey, Janet K Allen, Farrokh Mistree, and David L McDowell. "Design of multifunctional honeycomb materials". In: *AIAA J.* 42.5 (2004), pp. 1025–1033.

[90] Farrokh Mistree, Carolyn Conner Seepersad, Benjamin M Dempsey, David L McDowell, and Janet K Allen. "Robust concept exploration methods in materials design". In: *9th AIAA/ISSMO Symp. Multidiscip. Anal. Optim. Atlanta, GA*. 2002.

[91] Ole Sigmund and S Torquato. "Design of smart composite materials using topology optimization". In: *Smart Mater. Struct.* 8.3 (1999), p. 365.

[92] G B Olson. "Systems design of hierarchically structured materials: Advanced steels". In: *J. Comput. Mater. Des.* 4.3 (1998), pp. 143–156. ISSN: 1573-4900. DOI: 10.1023/A:1008670319664. URL: http://dx.doi.org/10.1023/A:1008670319664.

[93] S Ramakrishna. "Microstructural design of composite materials for crashworthy structural applications". In: *Mater. Des.* 18.3 (1997), pp. 167–173. ISSN: 02613069. DOI: 10.1016/S0261-3069(97)00098-8.

[94] V.K Ganesh, S Ramakrishna, S.H Teoh, and N.K Naik. "Microstructural design of textile composites". In: *Mater. Des.* 18.3 (1997), pp. 175–181. ISSN: 02613069. DOI: 10.1016/S0261-3069(97)00099-X.

[95] T.M. Pollock, J.E. Allison, D.G. Backman, M.C. Boyce, M. Gersh, E.A. Holm, R. LeSar, M. Long, A.C. IV Powell, J.J. Schirra, D.D. Whitis, and C. Woodward. *Integrated computational materials engineering: a transformational discipline for improved competitiveness and national security*. Tech. rep. on Integrated Computational Materials Engineering, National Research Council (US). Committee, 2008.

[96] Z Li, B Wen, and N Zabaras. "Computing mechanical response variability of polycrystalline microstructures through dimensionality reduction techniques". In: *Comput Mater Sci* 49 (2010). DOI: 10.1016/j.commatsci.2010.05.051. URL: http://dx.doi.org/10.1016/j.commatsci.2010.05.051.

[97] Changwon Suh, Arun Rajagopalan, Xiang Li, and Krishna Rajan. "The application of Principal Component Analysis to materials science data". In: *Data Sci. J.* 1 (2002), pp. 19–26. DOI: 10.2481/dsj.1.19.

[98] F. Roters, P. Eisenlohr, L. Hantcherli, D.D. Tjahjanto, T.R. Bieler, and D. Raabe. "Overview of constitutive laws, kinematics, homogenization and multiscale methods in crystal plasticity finite-element modeling: Theory, experiments, applications". In: *Acta Mater.* 58.4 (2010), pp. 1152–1211. ISSN: 13596454. DOI: 10.1016/j.actamat.2009.10.058.

[99] Joshua B. Shaffer, Marko Knezevic, and Surya R. Kalidindi. "Building texture evolution networks for deformation processing of polycrystalline fcc metals using spectral approaches: Applications to process design for targeted performance". In: *Int. J. Plast.* 26.8 (2010), pp. 1183–1194. ISSN: 07496419. DOI: 10.1016/j.ijplas.2010.03.010.

[100] Hamad F Al-Harbi, Marko Knezevic, and Surya R Kalidindi. "Spectral approaches for the fast computation of yield surfaces and first-order plastic property closures for polycrystalline materials with cubic-triclinic textures". In: (2010).

[101] Dorel Banabic, Frédéric Barlat, Oana Cazacu, and Toshihiko Kuwabara. "Advances in anisotropy and formability". In: *Int. J. Mater. Form.* 3.3 (2010), pp. 165–189. ISSN: 1960-6214. DOI: 10.1007/s12289-010-0992-9. URL: http://dx.doi.org/10.1007/s12289-010-0992-9.

[102] Marko Knezevic, Surya R. Kalidindi, and Raja K. Mishra. "Delineation of first-order closures for plastic properties requiring explicit consideration of strain hardening and crystallographic texture evolution". In: *Int. J. Plast.* 24.2 (2008), pp. 327–342. ISSN: 07496419. DOI: 10.1016/j.ijplas.2007.05.002.

[103] Stéphane Graff, Wolfgang Brocks, and Dirk Steglich. "Yielding of magnesium: From single crystal to polycrystalline aggregates". In: *Int. J. Plast.* 23.12 (2007), pp. 1957–1978. ISSN: 0749-6419. DOI: http://dx.doi.org/10.1016/j.ijplas.2007.07.009. URL: http://www.sciencedirect.com/science/article/pii/S0749641907001076.

[104] Paul Van Houtte, Anand Krishna Kanjarla, Albert Van Bael, Marc Seefeldt, and Laurent Delannay. "Multiscale modelling of the plastic anisotropy and deformation texture of polycrystalline materials". In: *Eur. J. Mech. - A/Solids* 25.4 (2006), pp. 634–648. ISSN: 0997-7538. DOI: http://dx.doi.org/10.1016/j.euromechsol.2006.05.003. URL: http://www.sciencedirect.com/science/article/pii/S0997753806000453.

[105] S.R. Kalidindi and S.E. Schoenfeld. "On the prediction of yield surfaces by the crystal plasticity models for fcc polycrystals". In: *Mater. Sci. Eng. A* 293.1 (2000), pp. 120–129. ISSN: 09215093. DOI: 10.1016/S0921-5093(00)01048-0.

[106] Woldemar Voigt. *Lehrbuch der Kristallphisic*. 1928, p. 962.

[107] A Reuss. "Berechnung der Fließgrenze von Mischkristallen auf Grund der Plastizitätsbedingung für Einkristalle ." In: *ZAMM - J. Appl. Math. Mech. / Zeitschrift für Angew. Math. und Mech.* 9.1 (1929), pp. 49–58. ISSN: 1521-4001. DOI: 10.1002/zamm.19290090104. URL: http://dx.doi.org/10.1002/zamm.19290090104.

[108] R Hill. "The Elastic Behaviour of a Crystalline Aggregate". In: *Proc. Phys. Soc. Sect. A* 65.5 (1952), p. 349. URL: http://stacks.iop.org/0370-1298/65/i=5/a=307.

[109] G.I. Taylor. "Plastic Strains in Metals". In: *J. Inst. Met.* 62 (1938), p. 307.

[110] G Sachs. "Zur Ableitung einer Fließbedingung". In: *Mitteilungen der Dtsch. Mater. Sonderh. IX Arb. aus dem Kaiser Wilhelm-Institut für Met. und dem-Staatlichen Mater. zu Berlin-Dahlem*. Berlin, Heidelberg: Springer Berlin Heidelberg, 1929, pp. 94–97. ISBN: 978-3-642-92045-5. DOI: 10.1007/978-3-642-92045-5_12. URL: http://dx.doi.org/10.1007/978-3-642-92045-5%7B%5C_%7D12.

[111] S. Nemat-Nasser and M. Hori. *Micromechanics: Overall Properties of Heterogeneous Materials*. Amsterdam: Elsevier Science Publishers, 1993.

[112] Jianmin Qu and Mohammed Cherkaoui. *Fundamentals of micromechanics of solids*. Wiley Hoboken, 2006.

[113] S.D. Volkov and N.A. Klinskikh. "Theory of the elastic properties of polycrystals". In: *Phys. Met. Metallogr.* 19 (1965), p. 24.

[114] V.A. Lomakin. "Deformation of microscopically nonhomogeneous elastic bodies". In: *J. Appl. Math. Mech.* 29.5 (1965), pp. 1048–1054.

[115] M.J. Beran and J. Molyneux. "Use of classical variational principles to determine bounds for the effective bulk modulus in heterogeneous media". In: *Q. Appl. Math.* 24.2 (1966), pp. 107–118. ISSN: 0033569X, 15524485. URL: http://www.jstor.org/stable/43635591.

[116] M.J. Beran, T.A. Mason, B.L. Adams, and T. Olsen. "Bounding elastic constants of an orthotropic polycrystal using measurements of the microstructure". In: *J. Mech. Phys. Solids* 44.9 (1996), pp. 1543–1563. ISSN: 00225096. DOI: 10.1016/0022-5096(96)00052-X.

[117] E Kröner. "Statistical Modelling". In: *Model. Small Deform. Polycrystals*. Ed. by John Gittus and Joseph Zarka. Dordrecht: Springer Netherlands, 1986, pp. 229–291. ISBN: 978-94-009-4181-6. DOI: 10.1007/978-94-009-4181-6_8. URL: http://dx.doi.org/10.1007/978-94-009-4181-6%7B%5C_%7D8.

[118] Ekkehart Kröner. *Statistical Continuum Mechanics, Course Held at the Department of General Mechanics*. Springer Vienna, 1971, p. 157. ISBN: 978-3-7091-2862-6. DOI: 10.1007/978-3-7091-2862-6. URL: http://link.springer.com/book/10.1007/978-3-7091-2862-6.

[119] S. Torquato. *Random Heterogeneous Materials: Microstructure and Macroscopic Properties*. Interdisciplinary Applied Mathematics. Springer New York, 2002. ISBN: 9781475763553. URL: https://books.google.com/books?id=UTfoBwAAQBAJ.

[120] S. Torquato. "Random Heterogeneous Media: Microstructure and Improved Bounds on Effective Properties". In: *Appl. Mech. Rev.* 44.2 (1991), pp. 37–76.

[121] S. Torquato. "Effective electrical conductivity of two-phase disordered composite media". In: *J. Appl. Phys.* 58.10 (1985), p. 3790. ISSN: 00218979. DOI: 10.1063/1.335593. URL: http://scitation.aip.org/content/aip/journal/jap/58/10/10.1063/1.335593.

[122] J.R. Willis. "Variational and Related Methods for the Overall Properties of Composites". In: *Adv. Appl. Mech.* 21 (1981), pp. 1–78. ISSN: 00652156. DOI: 10.1016/S0065-2156(08)70330-2.

[123] John J McCoy. "Macroscopic response of continua with random microstructures". In: *Mech. today* 6 (1981), pp. 1–40.

[124] J Korringa. "Theory of elastic constants of heterogeneous media". In: *J. Math. Phys.* 14.4 (1973), pp. 509–513.

[125] Stephen R. Niezgoda, David M. Turner, David T. Fullwood, and Surya R. Kalidindi. "Optimized structure based representative volume element sets reflecting the ensemble-averaged 2-point statistics". In: *Acta Mater.* 58.13 (2010), pp. 4432–4445. ISSN: 13596454. DOI: 10.1016/j.actamat.2010.04.041.

[126] Steven .R. Niezgoda, David .T. Fullwood, and Surya .R. Kalidindi. "Delineation of the space of 2-point correlations in a composite material system". In: *Acta Mater.* 56.18 (2008), pp. 5285–5292. DOI: 10.1016/j.actamat.2008.07.005.

[127] S. Torquato. "Statistical Description of Microstructures". In: *Annu. Rev. Mater. Res.* 32 (2002), pp. 77–111.

[128] H.-J. Bunge and W T Roberts. "Orientation distribution, elastic and plastic anisotropy in stabilized steel sheet". In: *J. Appl. Crystallogr.* 2.3 (Aug. 1969), pp. 116–128. DOI: 10.1107/S0021889869006704. URL: http://dx.doi.org/10.1107/S0021889869006704.

[129] I.M. Gel'fand, R.A. Minlos, Z. Ya. Shaprio, G. Cummins, T. Boddington, H.K. Farahat, and J.E. Mansfield. "Representations of the rotation and Lorentz groups and their applications". In: *Phys. Today* 17.8 (1964), p. 48.

[130] David M Turner and Surya R Kalidindi. "Statistical construction of 3-D microstructures from 2-D exemplars collected on oblique sections". In: *Acta Mater.* 102 (2016), pp. 136–148. ISSN: 1359-6454. DOI: http://dx.doi.org/10.1016/j.actamat.2015.09.011. URL: http://www.sciencedirect.com/science/article/pii/S1359645415006771.

[131] Benjamin Smith. "Microstructure-Sensitive Plasticity and Fatigue of Three Titanium Alloy Microstructures". Masters Thesis. Georgia Institute of Technology, 2013, pp. 1–121.

[132] G. Lütjering. "Influence of processing on microstructure and mechanical properties of (α+β) titanium alloys". In: *Mater. Sci. Eng. A* 243.1 (1998), pp. 32–45. ISSN: 09215093. DOI: 10.1016/S0921-5093(97)00778-8.

[133] Jason R. Mayeur. "Three dimensional modeling of Ti-Al alloys with application to attachment fatigue". PhD thesis. Georgia Institute of Technology, 2004.

[134] Craig P. Przybyla. "Microstructure-sensitive extreme value probabilities of fatigue in advanced engineering alloys". PhD thesis. Georgia Institute of Technology, 2010, p. 87.

[135] R. R. Boyer. "An overview on the use of titanium in the aerospace industry". In: *Mater. Sci. Eng. A* 213.1 (1996), pp. 103–114. ISSN: 0921-5093. DOI: http://dx.doi.org/10.1016/0921-5093(96)10233-1. URL: http://www.sciencedirect.com/science/article/pii/0921509396102331.

[136] M. J. Philippe, Emmanuel Bouzy, and Jean-Jacques Fundenberger. "Textures and Anisotropy of Titanium Alloys". In: *Texture and Anisotropy of Polycrystals*. Vol. 273. Materials Science Forum. Trans Tech Publications, 1998, pp. 511–522. DOI: 10.4028/www.scientific.net/MSF.273-275.511.

[137] R. J. Asaro. "Crystal Plasticity". In: *J. Appl. Mech.* 50.4b (1983), pp. 921–934.

[138] R. J. Asaro and A. Needleman. "Overview no. 42 Texture development and strain hardening in rate dependent polycrystals". In: *Acta Metall.* 33.6 (1985), pp. 923–953. ISSN: 0001-6160. DOI: http://dx.doi.org/10.1016/0001-6160(85)90188-9. URL: http://www.sciencedirect.com/science/article/pii/0001616085901889.

[139] J. C. Williams, R. G. Baggerly, and N. E. Paton. "Deformation behavior of HCP Ti-Al alloy single crystals". In: *Metall. Mater. Trans. A* 33.3 (2002), pp. 837–850. ISSN: 1543-1940. DOI: 10.1007/s11661-002-0153-y. URL: http://dx.doi.org/10.1007/s11661-002-0153-y.

[140] Florent Bridier, David L. McDowell, Patrick Villechaise, and José Mendez. "Crystal plasticity modeling of slip activity in Ti–6Al–4V under high cycle fatigue loading". In: *Int. J. Plast.* 25.6 (2009), pp. 1066–1082. ISSN: 0749-6419. DOI: http://doi.org/10.1016/j.ijplas.2008.08.004. URL: http://www.sciencedirect.com/science/article/pii/S0749641908001265.

[141] David L McDowell. "A perspective on trends in multiscale plasticity". In: *Int. J. Plast.* 26.9 (2010), pp. 1280–1309. ISSN: 0749-6419. DOI: http://dx.doi.org/10.1016/j.ijplas.2010.02.008. URL: http://www.sciencedirect.com/science/article/pii/S0749641910000306.

[142] Gustavo M Castelluccio, William D Musinski, and David L McDowell. "Computational micromechanics of fatigue of microstructures in the HCF–VHCF regimes". In: *Int. J. Fatigue* 93, Part 2 (2016), pp. 387–396. ISSN: 0142-1123. DOI: http://dx.doi.org/10.1016/j.ijfatigue.2016.05.019. URL: http://www.sciencedirect.com/science/article/pii/S0142112316301219.

[143] D Eylon and C M Pierce. "Effect of microstructure on notch fatigue properties of Ti-6Al-4V". In: *Metall. Trans. A* 7.1 (1976), pp. 111–121. ISSN: 1543-1940. DOI: 10.1007/BF02644046. URL: http://dx.doi.org/10.1007/BF02644046.

[144] Nima Shamsaei, Maksym Gladskyi, Kostyantyn Panasovskyi, Sergiy Shukaev, and Ali Fatemi. "Multiaxial fatigue of titanium including step loading and load path alteration and sequence effects". In: *Int. J. Fatigue* 32.11 (2010), pp. 1862–1874. ISSN: 0142-1123. DOI: http://dx.doi.org/10.1016/j.ijfatigue.2010.05.006. URL: http://www.sciencedirect.com/science/article/pii/S0142112310001337.

[145] Zhi-Rong Wu, Xu-Teng Hu, and Ying-Dong Song. "Multiaxial fatigue life prediction for titanium alloy {TC4} under proportional and nonproportional loading". In: *Int. J. Fatigue* 59 (2014), pp. 170–175. ISSN: 0142-1123. DOI: http://dx.doi.org/10.1016/j.ijfatigue.2013.08.028. URL: http://www.sciencedirect.com/science/article/pii/S0142112313002491.

[146] H. Nakamura, M. Takanashi, M. Wu, and Y. Shimizu. "Fatigue crack initiation and growth behavior of Ti-6Al-4V under non-proportional multiaxial loading". In: *Int. J. Fatigue* 33.7 (2011), pp. 842–848. DOI: http://doi.org/10.1016/j.ijfatigue.2010.12.013.

[147] Bernd Oberwinkler, Anton Lettner, and Wilfried Eichlseder. "Multiscale fatigue crack observations on Ti–6Al–4V". In: *Int. J. Fatigue* 33.5 (2011), pp. 710–718. ISSN: 0142-1123. DOI: http://doi.org/10.1016/j.ijfatigue.2010.11.024. URL: http://www.sciencedirect.com/science/article/pii/S0142112310002884.

[148] J A Araújo and D Nowell. "The effect of rapidly varying contact stress fields on fretting fatigue". In: *Int. J. Fatigue* 24.7 (2002), pp. 763–775. ISSN: 0142-1123. DOI: http://dx.doi.org/10.1016/S0142-1123(01)00191-8. URL: http://www.sciencedirect.com/science/article/pii/S0142112301001918.

[149] T. Dick, S. Basseville, and G. Cailletaud. "Fatigue modelling in fretting contact with a crystal plasticity model". In: *Comput. Mater. Sci.* 43.1 (2008), pp. 36–42. ISSN: 0927-0256. DOI: http://dx.doi.org/10.1016/j.commatsci.2007.07.055. URL: http://www.sciencedirect.com/science/article/pii/S0927025607002169.

[150] William D Musinski and David L McDowell. "Microstructure-sensitive probabilistic modeling of {HCF} crack initiation and early crack growth in Ni-base superalloy {IN100} notched components". In: *Int. J. Fatigue* 37 (2012), pp. 41–53. ISSN: 0142-1123. DOI: http://dx.doi.org/10.1016/j.ijfatigue.2011.

09.014. URL: http://www.sciencedirect.com/science/article/pii/S0142112311002696.

[151] A. Fatemi and D.F. Socie. "A critical plane approach to multiaxial fatigue damage including out-of-phase loading". In: *Fatigue Fract. Eng. Mater. Struct.* 11.3 (1988), pp. 149–165. DOI: 10.1111/j.1460-2695.1988.tb01169.x. URL: https://www.scopus.com/inward/record.uri?eid=2-s2.0-0023854625%7B%5C&%7DpartnerID=40%7B%5C&%7Dmd5=.

[152] M. Shenoy, J. Zhang, and David L. McDowell. "Estimating fatigue sensitivity to polycrystalline Ni-base superalloy microstructures using a computational approach". In: *Fatigue Fract. Eng. Mater. Struct.* 30.10 (2007), pp. 889–904. ISSN: 1460-2695. DOI: 10.1111/j.1460-2695.2007.01159.x. URL: http://dx.doi.org/10.1111/j.1460-2695.2007.01159.x.

[153] Emil Julius Gumbel. *Statistics of extremes*. Courier Corporation, 2012.

[154] Martin Ostoja-Starzewski. "Material spatial randomness: From statistical to representative volume element". In: *Probabilistic Eng. Mech.* 21.2 (2006), pp. 112–132. ISSN: 0266-8920. DOI: http://doi.org/10.1016/j.probengmech.2005.07.007. URL: http://www.sciencedirect.com/science/article/pii/S0266892005000433.

[155] F. J. Harewood and P. E. McHugh. "Comparison of the implicit and explicit finite element methods using crystal plasticity". In: *Comput. Mater. Sci.* 39.2 (2007), pp. 481–494. ISSN: 0927-0256. DOI: http://doi.org/10.1016/j.commatsci.2006.08.002. URL: http://www.sciencedirect.com/science/article/pii/S0927025606002278.

[156] Xiaolei Yin, Wei Chen, Albert To, Cahal McVeigh, and Wing Kam Liu. "Statistical volume element method for predicting microstructure–constitutive property relations". In: *Comput. Methods Appl. Mech. Eng.* 197.43–44 (2008), pp. 3516–3529. ISSN: 0045-7825. DOI: http://doi.org/10.1016/j.cma.2008.01.008. URL: http://www.sciencedirect.com/science/article/pii/S0045782508000339.

[157] Robert D McGinty and David L McDowell. "Multiscale polycrystal plasticity". In: *Trans. - Am. Soc. Mech. Eng. J. Eng. Mater. Technol.* 121 (1999), pp. 203–209.

[158] Joseph C. Tucker, Albert R. III Cerrone, Anthony R. Ingraffea, and Anthony D. Rollett. "Crystal plasticity finite element analysis for René88DT statistical volume element generation". In: *Model. Simul. Mater. Sci. Eng.* 23.3 (2015), p. 35003. URL: http://stacks.iop.org/0965-0393/23/i=3/a=035003.

[159] Tugce Ozturk, Clayton Stein, Reeju Pokharel, Christopher Hefferan, Harris Tucker, Sushant Jha, Reji John, Ricardo A Lebensohn, Peter Kenesei, Robert M Suter, and Anthony D Rollett. "Simulation domain size requirements for elastic response of 3D polycrystalline materials". In: *Model. Simul. Mater. Sci. Eng.* 24.1 (2016), p. 15006. URL: http://stacks.iop.org/0965-0393/24/i=1/a=015006.

[160] Hidetoshi Fujii, D.J.C. Mackay, and H.K.D.H. Bhadeshia. "Bayesian Neural Network Analysis of Fatigue Crack Growth Rate in Nickel Base Superalloys". In: *Iron Steel Inst. Japan* 36.11 (1996), pp. 1373–1382.

[161] B.P. Gauthaml, R. Kumarl, S. Bothraz, G. Mohapatral, N. Kulkarnil, and K.A. Padmanabhan. "More efficient ICME through materials informatics and process modeling". In: *Proc. 1st World Congr. Integr. Comput. Mater. Eng.* John Wiley & Sons. 2011, p. 35.

[162] Ankit Agrawal, Parijat D Deshpande, Ahmet Cecen, Gautham P Basavarsu, Alok N Choudhary, and Surya R Kalidindi. "Exploration of data science techniques to predict fatigue strength of steel from composition and processing parameters". In: *Integr. Mater. Manuf. Innov.* 3.1 (2014), pp. 1–19. ISSN: 2193-9772. DOI: 10.1186/2193-9772-3-8. URL: http://dx.doi.org/10.1186/2193-9772-3-8.

[163] Somnath Ghosh and Pritam Chakraborty. "Microstructure Sensitive Fatigue Crack Nucleation in Titanium Alloys Using Accelerated Crystal Plasticity FE Simulations". In: *Mater. with Intern. Struct. Multiscale Multif. Model. Simul.* Ed. by Patrizia Trovalusci. Cham: Springer International Publishing, 2016, pp. 43–62. ISBN: 978-3-319-21494-8. DOI: 10.1007/978-3-319-21494-8_4. URL: http://dx.doi.org/10.1007/978-3-319-21494-8%7B%5C_%7D4.

[164] P.J. Moriarty, W.E. Holley, and S.P. Butterfield. *Extrapolation of Extreme and Fatigue Loads Using Probabilistic Methods*. Tech. rep. Golden, Colorado: National Renewable Energy Laboratory, 2004, pp. 1–32.

[165] David W Scott. *Multivariate density estimation: theory, practice, and visualization*. John Wiley & Sons, 2015.

[166] Bernard W Silverman. *Density estimation for statistics and data analysis*. Vol. 26. CRC press, 1986.

[167] Noah H. Paulson, Matthew W. Priddy, David L. McDowell, and Surya R. Kalidindi. "Data-driven reduced-order models for rank-ordering the high cycle fatigue performance of polycrystalline microstructures". In: *Prep.* (2017).

[168] Subra Suresh. *Fatigue of materials*. Cambridge university press, 1998.

[169] Ruoqian Liu, Yuksel C Yabansu, Zijiang Yang, Alok N Choudhary, Surya R Kalidindi, and Ankit Agrawal. "Context Aware Machine Learning Approaches for Modeling Elastic Localization in Three-Dimensional Composite Microstructures". In: *Integr. Mater. Manuf. Innov.* (2017), pp. 1–12. ISSN: 2193-9772. DOI: 10.1007/s40192-017-0094-3. URL: http://dx.doi.org/10.1007/s40192-017-0094-3.

VITA

Noah H. Paulson was born on December 2, 1990 to Matthew and Jane Paulson. Noah was raised in Lexington, Massachusetts and attended the public schools there. He subsequently attended Tufts University and graduated summa cum laude with a B.S. in Mechanical Engineering in 2013. Noah was awarded the George W. Woodruff Fellowship and began his graduate studies at the Georgia Institute of Technology in late 2013. He joined Dr. Surya R. Kalidindi's research group soon after.